Composite Functional Materials
2026, 2(3): 20260304 https://doi.org/10.63823/20260304

REVIEW ARTICLE

Resolving cross-scale contradictions in fast-charging zinc anode interfaces for practical applications

Jingwen Liu[a], Han Jiang[a,b], Qianyi Chen[a,b], Xiang Guo[a], Hongxu Li[a], Viet Q. Bui[c], Xinghui Liu[a,b,*]

a. National Key Laboratory of Aerospace Chemical Power, Hubei Institute of Aerospace Chemotechnology, Xiangyang 441003, China
b. Center for Low-dimensional Quantum Materials, School of Materials Science and Chemical Engineering, Hubei University of Technology, Wuhan, 430068, Hubei, China.
c. University of Technology and Education - The University of Danang, 48 Cao Thang, Danang, 550000, Vietnam.

ABSTRACT: Fast-charging aqueous zinc-ion batteries (AZIBs) have advanced rapidly owing to their intrinsic safety, low cost and the longer Sand's time of divalent Zn^{2+}, which can delay ion-depletion-limited failure compared with monovalent Li^{+}. Nevertheless, the divalent nature also imposes sluggish desolvation and interfacial charge-transfer kinetics, making fast zinc deposition highly susceptible to polarization, dendrite growth, parasitic reactions, and rapid capacity decay. Existing reviews mainly classify materials and strategies, whereas the field lacks a scale-resolved framework explaining where fast-charging failure originates, how it propagates and when it becomes irreversible. Here we propose a polarization-driven “three contradictions” framework for AZIBs, in which microscopic ion-electron transport mismatch generates polarization, mesoscale kinetics-uniformity conflict amplifies nonuniform deposition, and macroscopic electrochemical stability window (ESW)-limited rate-capacity trade-off converts accumulated overpotential into capacity loss and full-cell failure. By mapping desolvation design, foil/powder electrode engineering and wide-window electrolyte strategies onto these three stages, we further propose practical evaluation protocols based on DOD_{Zn}, cumulative plating capacity (CPC), E/C ratio, N/P ratio and full-cell validation, providing a roadmap from high-rate laboratory demonstrations toward application of AZIBs under XFC conditions.

KEYWORDS: Aqueous zinc-ion batteries, Extreme fast charging, Kinetics and stability, Polarization, Zn anode.

1. Introduction

The commercialization of next-generation energy storage hinges on the ability to deliver extreme fast charging (XFC) without sacrificing safety, lifetime, or energy density.[1-3] However, fast charging is not simply achieved by increasing current density.[4, 5] Under XFC conditions, electrochemical systems are driven far from quasi-equilibrium, amplifying ion-transport limitations, interfacial polarization, morphological instability, and parasitic reactions that are often masked under mild operating conditions.

Received: July 29, 2026. **Revised:** August 29, 2026. **Accepted:** October 6, 2026. **Available online:** October 13, 2026
***Corresponding author: E-mail address:** liuxinghui119@gmail.com (X. Liu, https://orcid.org/0000-0001-7744-1400)
© 2026 Wave Academic Press Limited.
This is an open access article under the CC BY-NCND license (http://creativecommons.org/licenses/by-nc-nd/4.0/)

Understanding how these limitations emerge and propagate across different length scales is therefore essential for designing practical fast-charging batteries. In lithium-ion batteries (LIBs), XFC is commonly defined at the full-cell level as recovering ~80% of capacity or SOC within ≤15 min. [6, 7] Although no universally accepted XFC criterion has been established for AZIBs, recent Ah-level AZIB pouch cells have adopted this time-based benchmark, suggesting its applicability to aqueous Zn systems.[8]

Currently, LIBs dominate the energy storage market, with graphite-based materials serving as the prevailing anode. However, under XFC conditions, sluggish solid-state intercalation and diffusion of Li^+ in graphite can drive anode polarization, [9] causing metallic Li deposition, commonly termed lithium plating, and associated capacity loss and safety risks.[10] Lithium-metal anodes bypass this intercalation barrier *via* a direct plating/stripping mechanism, but their high thermodynamic reactivity in organic electrolytes exacerbates dendrite formation and safety risks.[11-14] Conversely, zinc anodes also operate *via* the plating/stripping mechanism but possess moderate reactivity, enabling safe operation in aqueous electrolytes.[15-18] Together with the high theoretical gravimetric capacity of Zn metal (820 mAh g^{-1}), a high volumetric capacity (5854-5855 mAh cm^{-3}), suitable redox potential of -0.763 V vs. SHE, low cost, and intrinsic aqueous safety, aqueous zinc-ion batteries (AZIBs) have emerged as attractive candidates for scalable energy storage.[19, 20] More importantly for XFC, Zn^{2+} carries an intrinsic mass-transfer advantage that distinguishes it from monovalent charge carriers. Under ideal diffusion-limited conditions, Sand's time predicts that the time required for complete ion depletion scales with the square of the ionic charge number, suggesting that divalent Zn^{2+} can theoretically delay concentration depletion under comparable current-density and concentration conditions.

Based on these advantages, AZIBs have attracted rapidly increasing global interest, as evidenced by the exponential growth of AZIB publications over the past decade. [21-23] Existing review and perspective articles have advanced the field from several complementary directions: First, mechanism-focused reviews have discussed electric-double-layer (EDL) regulation, [24, 25] Zn^{2+} solvation/desolvation chemistry[26-28], and solid-liquid interfacial charge transport in aqueous zinc batteries.[29] Second, application-oriented reviews have emphasized high areal capacity or high-mass-loading electrodes, [30] limited zinc excess, lean electrolyte conditions, low negative-to-positive capacity (N/P) and electrolyte-to-capacity ratio (E/C) ratios[31], soft-pack or pouch-cell configurations[32], and grid-relevant stationary storage scenarios[33]. Third, theory- and data-assisted studies have used first-principles calculations, atomistic simulations, machine-learning-assisted screening, and multiscale modelling to understand degradation mechanisms and accelerate materials or electrolyte design.[34-36] Alongside these review efforts, fast-charging AZIB studies have also progressed rapidly, moving from simple high-current cycling demonstrations toward mechanism correction and multifunctional designs that combine solvation regulation, interfacial stabilization, deposition guidance, parasitic-reaction suppression, and usable ESW expansion. [22, 26, 37, 38, 39]

Despite these advances, two related problems remain unresolved. First, existing AZIB reviews have not yet treated fast-charging AZIBs as a distinct field with a scientific understanding of their evolution. Second, the fast-charging literature itself is difficult to summarize by a single descriptor because the reported strategies are highly scattered and intrinsically multifunctional: an electrolyte additive, artificial interphase, and electrode architecture may simultaneously weaken Zn^{2+} solvation, stabilize the interface, homogenize Zn deposition, suppress water activity, and expand the ESW. Material-based classifications are useful for describing what has been designed, but they provide limited insight into the stage-dependent progression of fast-charging failure. What remains missing is a scale-resolved principle that clarifies where failure originates, how it is amplified, and when it becomes irreversible.

Here, we establish a cross-scale "three contradictions" framework to understand fast-charging zinc anode interfaces. In this framework, we identify that polarization originates from microscopic ion-electron transport mismatch, is amplified through mesoscale deposition non-uniformity, and ultimately collides with the macroscopic aqueous ESW limit, leading to parasitic reactions and capacity loss. Guided by this logic, this Review first reconstructs the scientific trajectory of fast-charging AZIBs, then summarizes representative strategies across the microscale, mesoscale, and macroscale levels. Finally, we propose scale-resolved evaluation protocols that bridge XFC-relevant Zn-anode testing to practical full-cell XFC performance, together with future design principles for XFC AZIBs. By linking diverse material strategies to their corresponding scales, this Review aims to provide a framework for resolving the coupled limitations of fast-charging zinc anodes.

2. Scientific basis and evolution of fast-charging AZIBs

Unlike LIBs, where extreme fast charging is mainly limited by sluggish Li^+ transport, interphase instability, lithium plating, and safety concerns in organic electrolytes, [40, 41] AZIBs are primarily constrained by sluggish Zn^{2+} desolvation, interfacial polarization, nonuniform zinc deposition, and parasitic reactions within the narrow ESW. These differences are rooted in the intrinsic properties of the working ions, including electronic configuration, valence state, ionic radius, solvation structure, and mass-transfer boundary (**Figure 1a**)[26, 42, 43]. Although Li^+ and Zn^{2+} possess comparable ionic radii (0.76 Å and 0.74 Å, respectively), [44] the divalent nature of Zn^{2+} gives it a much higher charge density, leading to interfacial electrochemistry fundamentally distinct from that of monovalent Li^+. This ion-level distinction makes Zn^{2+} a double-edged charge carrier for fast charging.

On the one hand, the closed-shell $[Ar]3d^{10}$ configuration and high charge density of Zn^{2+} thermodynamically favor a rigid six-coordinated octahedral hydration structure, in sharp contrast to the more labile solvation structure of Li^+.[45, 46] Before reduction, hydrated Zn^{2+} must undergo a multi-step desolvation process to strip its strongly bound water sheath, imposing a substantial kinetic barrier at the zinc/electrolyte interface (**Figure 1b**).[47, 48] Under XFC conditions, sluggish desolvation causes the interfacial supply of active Zn^{2+} to lag behind rapid electron delivery. This ion-electron transport mismatch generates severe concentration polarization and nonuniform distribution of Zn^{2+} concentration, electric field and charge-transfer rate. [26, 47-49] Once such microscopic polarization becomes spatially heterogeneous, zinc deposition preferentially occurs at regions with lower nucleation barriers or stronger local electric fields, leading to uneven nuclei, protrusion growth, and porous or dendritic deposits. [37, 50-57] These morphological heterogeneities further concentrate current and ion flux, amplifying local overpotential until the accumulated polarization approaches the aqueous ESW margin and triggers parasitic reactions, including the hydrogen evolution reaction (HER), [38] local pH increase, zinc corrosion, and zinc hydroxide sulfate (ZHS) accumulation. [58-62]

On the other hand, Zn^{2+} also offers an intrinsic mass-transfer advantage for high-current operation. Because zinc deposition involves a two-electron transfer process, the onset of complete ion depletion is delayed according to Sand's time theory (**Figure 1c**).[63] Described by the equation: $\tau = \frac{\pi D(zFC_0)^2}{4J^2}$ (where D is the diffusion coefficient, z is the charge number, F is Faraday's constant, C_0 is the bulk concentration, and J is the current density).[64] Since Sand's time scales with the square of the ionic charge number, divalent Zn^{2+} theoretically exhibits a longer depletion time than monovalent Li^+ under comparable current density and bulk concentration. This means that if the desolvation barrier and associated parasitic reactions can be mitigated, AZIBs should exhibit intrinsic tolerance to high-current plating/stripping.

Driven by this paradox, the past decade has witnessed rapid advances in fast-charging AZIBs. Early studies primarily focused on higher current densities and longer cycling life after the demonstration of mild-rechargeable AZIBs.[65] Subsequent work revealed that high current does not always aggravate dendritic failure; instead, under certain conditions, it can accelerate nucleation and promote dense deposition.[66-68] This mechanism correction was further supported by theoretical descriptions such as Sand's thickness, which provided guidelines for planar zinc deposition under practical fast-charging conditions. [69] More recently, the field has shifted from single-performance optimization toward balanced evaluation under practical constraints, including zinc utilization ratio, cumulative plating capacity (CPC), failure inflection behavior, electrolyte inventory, and cell-level scalability. [70-72] This evolution indicates that fast-charging AZIB research is moving from empirical performance improvement toward mechanism-guided and application-oriented design (**Figure 1d**).

3. Core challenges of the fast-charging anode interface

Fast-charging zinc anodes fail through a cross-scale evolution of polarization rather than through isolated interfacial reactions.[37] Polarization is first generated at the molecular/interface level by sluggish Zn^{2+} desolvation and ion-electron transport mismatch, then amplified at the electrode level by heterogeneous ion/electron flux and nucleation behavior, and finally converted into cell-level failure when the accumulated overpotential consumes the usable aqueous ESW margin (**Figure 2**). Accordingly, this section discusses the three coupled contradictions that govern fast-charging zinc anode interfaces: microscale transport mismatch, mesoscale kinetics-uniformity conflict, and macroscale rate-capacity limitation.

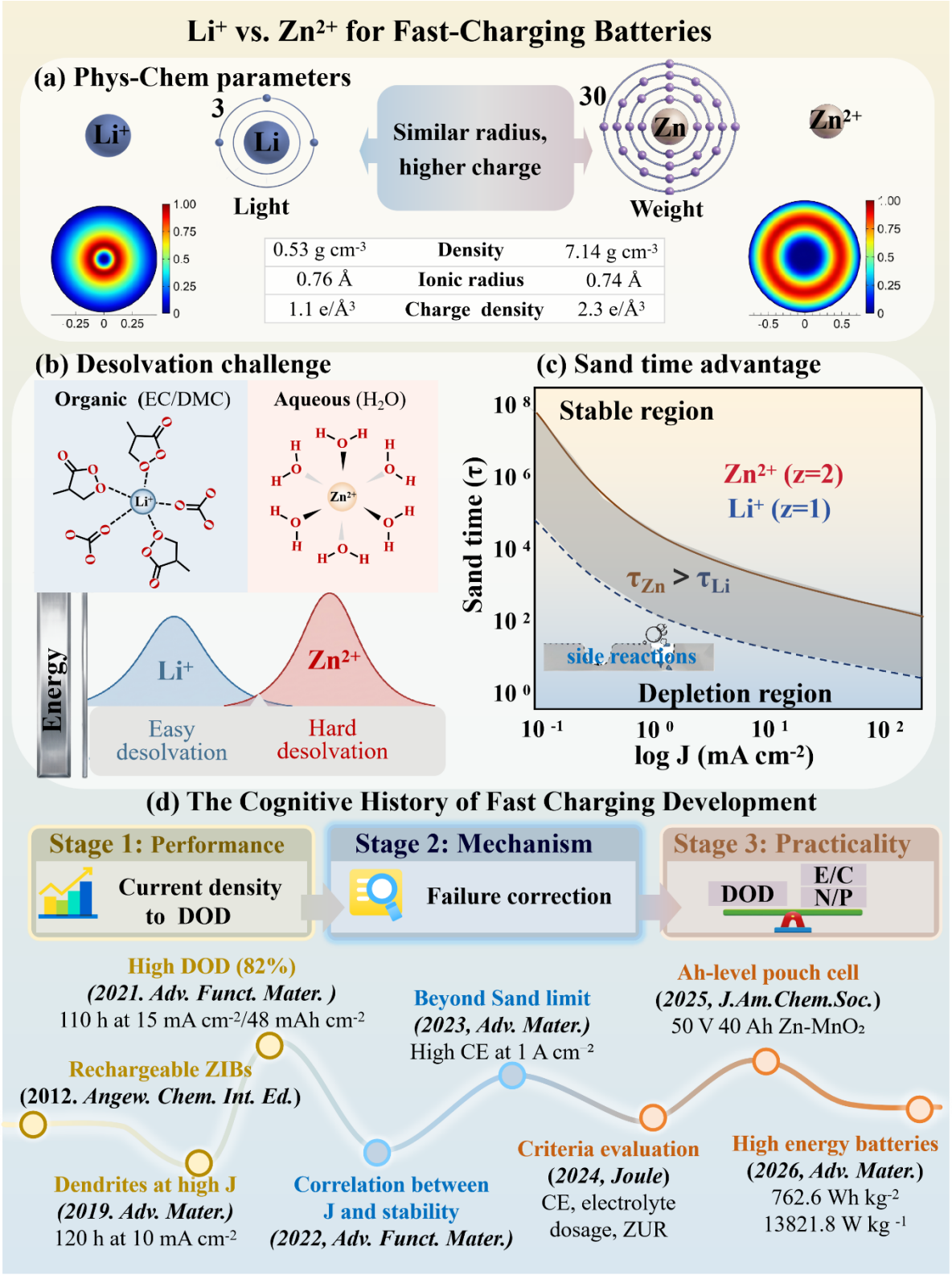


Figure 1. (a) The physicochemical parameters of Li and Zn; (b) the solvation structure and desolvation energy of Li^+ and Zn^{2+}; (c) Sand's time theory; (d) the trajectory of scientific understanding of fast-charging research.

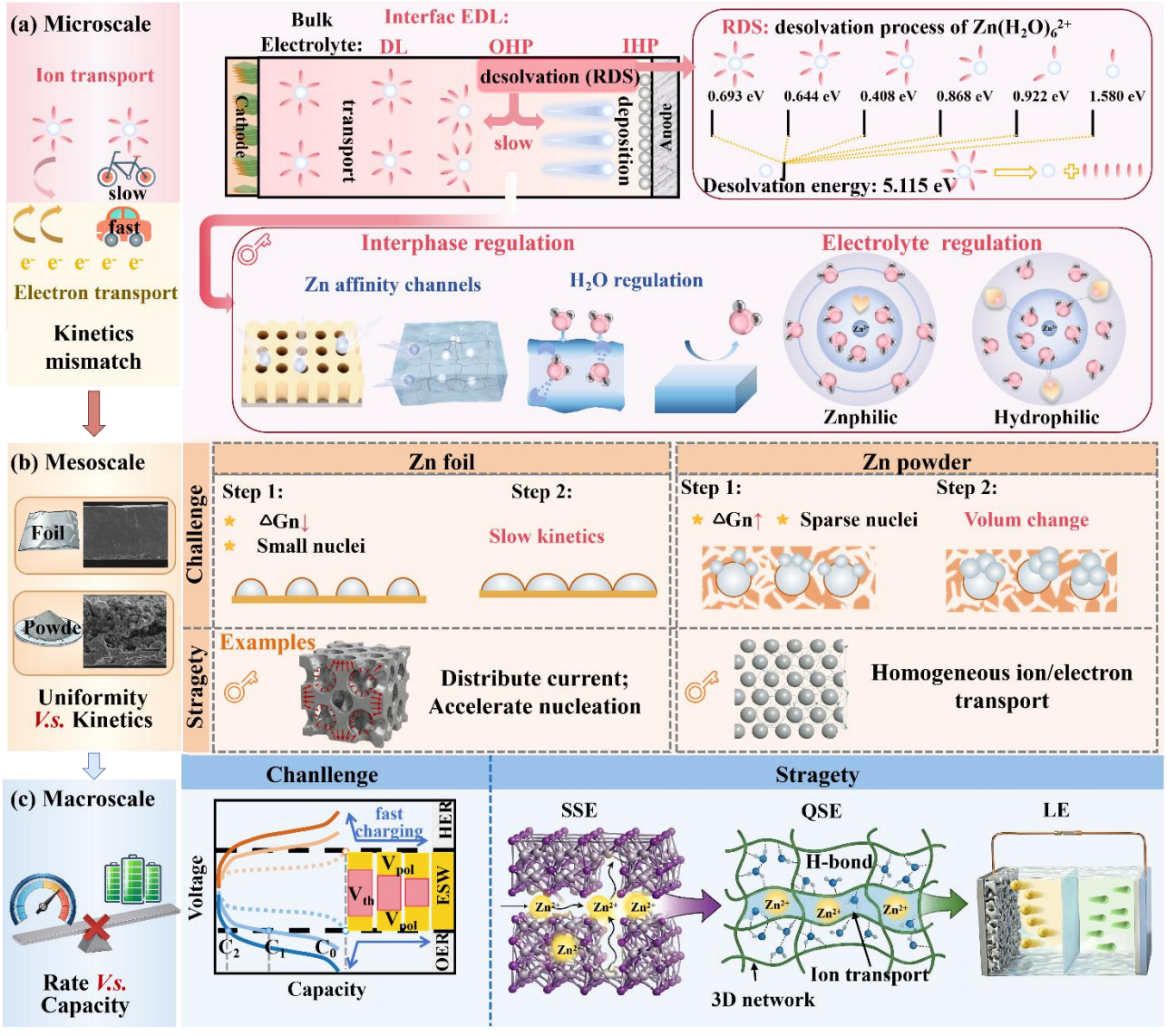


Figure 2. The progressive multi-scale contradictions of fast-charging aqueous zinc anodes and their corresponding mitigation strategies: (a) microscale, (b) mesoscale, and (c) macroscale.

3.1 Microscale polarization generation: ion-electron transport mismatch

At the microscale, the primary origin of fast-charging polarization is the mismatch between rapid electron delivery and sluggish Zn^{2+} transfer. Under XFC, electrons can be supplied to the metallic anode almost instantaneously, whereas solvated Zn^{2+} first migrate through the EDL before being reduced. This interfacial ion-transfer process is fundamentally constrained by desolvation, which has been identified as a key rate-determining step (RDS) for zinc plating.[26] Before plating can occur, the solvated Zn^{2+} migrates from the diffusion layer (DL) to the outer Helmholtz plane (OHP), where the rigid hydration sheath must be sequentially removed before electron transfer and Zn deposition (**Figure 2a**).[47, 49] Because the strongly bound $[Zn(H_2O)_6]^{2+}$ structure imposes a high energetic penalty, the interfacial supply of electroactive Zn^{2+} cannot keep pace with electron transfer under XFC conditions. This mismatch directly generates concentration polarization. Once interfacial Zn^{2+} consumption exceeds replenishment, the local ion concentration decreases and the anode requires a larger driving force to sustain the imposed current. The resulting overpotential not only slows charge-transfer

kinetics but also pushes the local electrode potential toward parasitic pathways. Therefore, the first contradiction of fast-charging zinc anodes is the kinetic incompatibility between fast electron transfer and delayed Zn^{2+} desolvation/migration.

Resolving this transport bottleneck requires interventions that directly dismantle the desolvation barrier (**Figure 2a**), fundamentally aiming to decouple Zn^{2+} from H_2O.[73] Constructing an artificial solid electrolyte interface (SEI) is the premier approach, driven primarily by Zn^{2+} affinity and supported by auxiliary H_2O regulation.[74] To facilitate rapid transit, primary Zn^{2+} affinity is regulated *via* inorganic ionic channels or organic coordination networks.[75, 29] Complementing this, H_2O regulation mitigates parasitic corrosion by either trapping water molecules within hydrogen-bonded networks or physically excluding free water through hydrophobic coatings.[76-78] Beyond interfacial modification strategies, fundamentally lowering the desolvation barrier requires reconfiguring the bulk solvation structure. This involves two pathways: substituting the primary solvation sheath with zinc-philic components to entirely displace inner H_2O, or introducing hydrophilic additives into the secondary sheath.[79] The latter disrupts the bulk hydrogen-bonded network, fundamentally weakening the core H_2O-Zn^{2+} interaction.[80, 81] Based on this progressive logic, Section 4 establishes a systematic taxonomy of these strategies, divided into SEI structural design (Section 4.1) and liquid electrolyte compositional engineering (Section 4.2).

3.2 Mesoscale polarization amplification: kinetics-uniformity conflict

After polarization is generated at the molecular/interface level, its practical impact is determined by how it is distributed across the electrode. At the mesoscale, local current density, electric-field distribution, nucleation barrier, and electrode morphology determine whether microscopic polarization is homogenized or amplified. This is most clearly reflected in the contrast between planar zinc foils and porous zinc powder anodes (**Figure 2b**).

Planar zinc foils provide a mechanically continuous and geometrically simple electrode surface, which is beneficial for dense and uniform deposition. However, their limited electrochemically active area and relatively high nucleation barrier require a large overpotential to initiate zinc plating.[50, 51] Conversely, porous zinc powder leverages a vast specific surface area to dilute local current density and depress the nucleation barrier. This drives rapid nucleation and minimizes polarization, unlocking the swift kinetics essential for fast charging.[52] Nevertheless, this rapid kinetic profile fundamentally compromises structural integrity. The initial nucleation is loose and uncoordinated; upon sustained growth, it triggers massive volume expansion, mechanical pulverization, and amplified parasitic reactions like HER.[53-55] Ultimately, this highlights the fundamental mesoscale contradiction: planar foils offer structural uniformity but suffer kinetic limitations, while porous powders provide kinetic superiority but inevitably face uniformity limitations, even structural degradation.

The second contradiction is therefore a mesoscale kinetics-uniformity conflict. Increasing active area and lowering nucleation barriers can improve high-rate kinetics, but these benefits may be offset if the electrode architecture amplifies spatial heterogeneity (**Figure 2b**). For zinc foil anodes, fast-charging strategies primarily focus on homogenizing local electric fields and lowering the polarization overpotential to accelerate kinetics.[56] In contrast, modifications for zinc powder anodes are dedicated to mechanically and chemically stabilizing the highly reactive, expanding interface under extreme rates.[57] Following this dichotomy, Section 5 will separately review the state-of-the-art modification strategies for zinc foils (Section 5.1) and zinc powders (Section 5.2).

3.3 Macroscale polarization-induced failure: ESW-limited rate-capacity trade-off

At the macroscale, the ultimate consequence of fast-charging polarization is determined by the finite ESW of the aqueous electrolyte (**Figure 2c**).[60, 61] Under low-rate, quasi-equilibrium conditions, interfacial kinetic resistance is minimal, rendering the polarization overpotential (V_{pol}) negligible compared with the theoretical voltage (V_{th}). Consequently, the anode working potential ($V_{th} + V_{pol}$) remains within the ESW, enabling the cell to approach its theoretical maximum reversible capacity (C_0). However, transitioning to XFC conditions exposes a contradiction between kinetic demand and thermodynamic stability. To overcome the barriers to desolvation and nucleation, the system requires a high driving force, which increases V_{pol} and shifts the working potential toward the HER boundary. Consequently, the usable polarization margin narrows, parasitic water decomposition begins earlier,[62] and the reversible

capacity decreases from C_0 through C_1 to C_2.

Viewed through the fundamental energy equation ($E=C\times V$), this contradiction defines the ultimate macroscale bottleneck. Under high-rate conditions, energy output is limited not only by capacity retention (C) but also by the usable operating voltage (V) within the aqueous ESW. A larger V_{pol} cannot simply be compensated by increasing the applied voltage, because the added driving force may instead trigger HER and consume active charge. Thus, kinetic polarization imposes a double penalty: it depresses the effective output voltage while accelerating irreversible capacity loss. This rate-capacity-voltage coupling defines the practical energy-density limit of fast-charging AZIBs.

Therefore, expanding the usable aqueous stability margin is critical for sustaining fast charging. To address this limitation, macroscale electrolyte engineering diverges into three evolutionary pathways (**Figure 2c**). Solid-state electrolytes (SSEs) maximize the ESW by eliminating water, but their sluggish diffusion induces massive polarization. Quasi-solid-state gels offer a structural compromise, deploying polymer networks to immobilize water, which still inadvertently throttles ion migration.[82] Breaking this trade-off, novel liquid systems (e.g., decoupled electrolytes) have emerged as the frontier.[83] They retain the rapid aqueous kinetics while dynamically adapting the apparent ESW, driving active components to anode or cathode interfaces during charging.[84] Following this logic, Section 6 categorizes these macroscale strategies across solid-state (6.1), gel-state (6.2), and advanced liquid electrolyte systems (6.3).

4. Interphase and solvation regulation for rapid ion transport

Within the polarization-cascade framework, desolvation regulation targets the initial generation of interfacial polarization under XFC. The key is to simultaneously sustain rapid Zn^{2+} supply and facilitate interfacial dehydration without introducing additional transport resistance. Current strategies therefore fall into two categories: interphase regulation, which controls Zn^{2+} transport and H_2O distribution directly at the electrode/electrolyte interface, and electrolyte regulation, which tunes the solvation state of Zn^{2+} before it reaches the interface. Representative strategies and their reported performances are summarized in **Table 1**.

4.1 Interphase regulation: SEI structure and composition regulation

Artificial SEIs regulate the hydrated Zn^{2+} anode environment by balancing two interdependent functions: accelerating Zn^{2+} supply to prevent interfacial electron depletion; regulating H_2O to facilitate dehydration and suppress parasitic reactions. Importantly, these two functions should not be considered independently, because rapid Zn^{2+} transport without effective water regulation can intensify HER, whereas excessive water exclusion or binding may compromise ion accessibility.

4.1.1 Zn^{2+} channels for accelerated ion supply

One approach is to construct ion-conducting channels that continuously replenish Zn^{2+} consumed during high-rate deposition. Rigid inorganic channels effectively maintain mechanical strength. For instance, a zincophilic nanofluid channel (ZNC) and $ZnWO_4$ (ZWO) nanoarrays interphase guides Zn^{2+} transport through confined channels (**Figure 3a**), not only significantly shortening the thickness of the diffusion mass transfer zone, but also effectively alleviating the interfacial concentration polarization caused by uneven ion distribution (**Figure 3b**).[85] Benefiting from the synergistic reshaping of mass-transfer kinetics and the interfacial concentration gradient, the Zn symmetric cell can cycle over 500 h under 10 mA cm^{-2}/5 mAh cm^{-2} (**Figure 3c**). Removing crystalline grain-boundary constraints further improves transport: amorphous $ZnWO_4$ exhibits a calculated Zn^{2+} diffusion energy barrier of 0.19 eV, compared with 0.36 eV for its crystalline state, and supports stable cycling at 20 mA cm^{-2} and 10 mAh cm^{-2} for over 600 h.[86]

Beyond rigid inorganic channels, soft polymer channels (organic interphases) provide structural flexibility and abundant coordination sites for ion transfer. Polymer macromolecules are rich in polar functional groups (e.g., cyano, pyridine, hydroxyl, and ether groups), and their strong adsorption onto Zn^{2+} directly participates in and promotes the desolvation of Zn^{2+}. A bacterial-cellulose nanofluidic layer, for instance, was introduced at the anode/electrolyte interface (**Figures 3d and 3e**). [87] The Lewis basic groups, such as ether bonds and hydroxyl groups, enriched on its macromolecular chains can spontaneously concentrate Zn^{2+} and shield the surface charges of the channels to form an electroneutral, single-ion transport pathway (**Figure 3f**). In situ electrochemical digital holography directly revealed a stable interfacial Zn^{2+} concentration field at 10 mA cm^{-2},

Table 1. Interphase and solvation strategies for rapid Zn ion transport.

Strategy		Symmetric cell							Full cell			
		Kinetic descriptor		J (mA cm^{-2})	Q_{Area} (mAh cm^{-2})	DOD (%)	Time (h)	XFC regime	Type	Current (A g^{-1})	Cycle number	Capacity retention (%)
		Ea (kJ/mol)	tZn^{2+}									
SEI structure and composition regulation	Zn@ZWO[85]	9.02	0.72	10	5	NR	650	II	V_6O_{13}/Zn	10	5000	100
				10	1.7		2000					
	BC@Zn[87]	41.96	0.64	40	40	75.97	1573	IV	Zn/I_2	1	9000	75.60
				100	100	90.91	490					
	F-Sb SAs@Zn[89]	13.42	0.89	20	5	8.5	1200	III	Zn/I_2	10	100000	94.3
	PA-Hn@Zn[90]	33.62	NR	10	5	NR	600	III	PA-Hn@Zn/KVOH	5	3000	100
				10	10		275					
	ZPHC@Zn[91]	25.4	0.79	5	2	NR	500	III	V_2O_5/ZPHC@Zn	5	1000	75.1
				10	10		300					
	ZVO@Zn[92]	NR	NR	2	1	NR	1000	I	ZVO@Zn/MnO_2	0.5	300	92.7
Liquid electrolyte solvation structure	SCL additives[93]	27.0	NR	30	30	73.3	171	IV	Zn/$NH_4V_4O_{10}$	5	4000	84.9
				30	40	97.7	98					
	MGMs [94]	34.76	0.82	5	5	NR	3000	III	Zn/PANI	5	5000	68.5
				20	5		500					
	BSB [95]	37.9	0.86	5	5	NR	3227	III	Zn/V_2O_5	2	1800	80
				30	1		3600					
	VAIMLys [96]	NR	0.89	1	1	NR	4000	II	Zn/V_2O_5	2	1500	82.2
				10	1		1000					
	STTE [97]	NR	NR	10	10	NR	200	III	Zn/NaVO	0.2	85	NR
				10	20		450					
	STEs [98]	NR	0.60	10	10	85.4	625	III	Zn/NVO	4	4000	87.7
	Pro, $C_5H_9NO_2$[99]	NR	NR	0.5	0.5	NR	2500	I	PANI/Zn	1	1300	93.6
				0.5	0.5		1600					
	DHP [100]	36.33	0.59	5	2	NR	4500	II	Zn/$NH_4V_4O_{10}$	5	1000	93.9
				5	5		540					
	ACN [101]	32.5	NR	1	1	NR	1200	I	Zn/V_6O_{13}	10	10000	99.2

Note:

(1) Zinc tungstate (ZWO, $ZnWO_4$); bacterial cellulose (BC); single atoms (SAs); F-axially coordinated Sb single atoms (F-Sb SAs); phytic acid (PA); hydrogen-bond-anchored phytic acid–Zn/hydrogel protective layer (PA-Hn); zinc phytate/halloysite nanotubes/carboxymethyl cellulose composite interfacial layer (ZPHC); zinc vanadium oxide (ZVO); sucralose (SCL); multifunctional-group molecules (MGMs); bisolvation-sheath-bichelation (BSB); 1-vinyl-3-aminopropyl imidazolium lysinate (VAIMLys); solvent-tailored triflate electrolyte (STTE); steric-hindrance electrolytes (STEs); proline (Pro); dimethyl hydroxymethylphosphonate (DHP); acetonitrile (ACN).

(2) XFC regime is classified using current-density/areal-capacity framework; for strategies reported under multiple symmetric-cell conditions, the highest reached regime is used:

Regime I, fundamental evaluation (j<5 mA cm^{-2} and Q_{areal} ≤1 mAh cm^{-2});

Regime II, moderate fast charging (j≤10 mA cm^{-2} and Q_{areal}≤5 mAh cm^{-2});

Regime III, single-factor XFC-relevant stress (j >10 mA cm^{-2} or Q_{areal}>5 mAh cm^{-2} or DOD_{Zn}≥10%);

Regime IV, coupled high-current/high-areal-capacity XFC-relevant condition (j >20 mA cm^{-2} and Q_{areal}>5 mAh cm^{-2}).

while additional in-situ Raman spectroscopy showed reconstruction of the interfacial H-bond network, linking rapid Zn^{2+} replenishment with facilitated desolvation. Accordingly, the desolvation activation energy decreased from 58.19 to 41.96 kJ mol^{-1}, enabling stable cycling even at 40 mA cm^{-2}/40 mAh cm^{-2} and 100 mA cm^{-2}/100 mAh cm^{-2} (**Figure 3g**). Notably, Zhou *et al*. innovatively extended in situ Raman spectroscopy from conventional molecular-species identification to real-time visualization of interfacial ion-concentration fluctuations.[88] By tracking the SO_4^{2-} band (~980 cm^{-1}) near the moving electrode/electrolyte interface, they directly mapped the temporal evolution of Zn^{2+} distribution during deposition.

These results indicate that a low calculated diffusion barrier alone is insufficient to establish XFC capability. Under sustained high-current deposition, the more

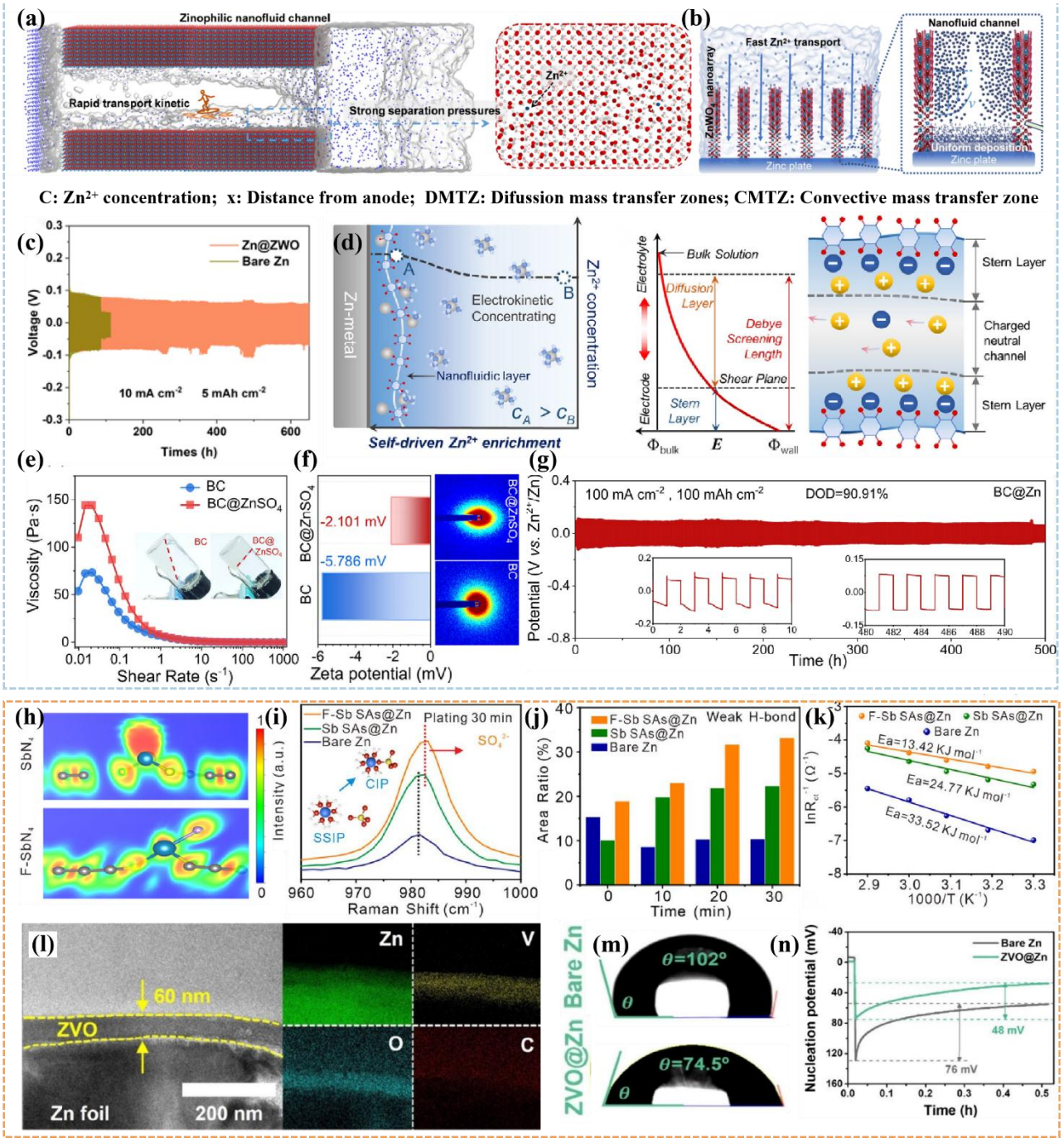


Figure 3. (a) Schematic diagram of the nanofluid channel model and dual regulation effects. (b) Mechanism diagram of fast Zn^{2+} transport in nanofluid channels. (c) Cycling performance of symmetric batteries at 10 mA cm^{-2}.[85] Copyright 2024, Elsevier. (d) Ionic conductivities of BC and BC@$ZnWO_4$ at different $ZnSO_4$ concentrations, and a schematic diagram of the concentration gradient. (e) Viscosity of BC and BC@$ZnWO_4$ at different shear rates. (f) Zeta potential and SAXS test results. (g) Cycle performance test of BC@Zn/BC@Zn symmetric cells at 100 mA cm^{-2}, 100 mAh cm^{-2}.[87] Copyright 2025, Wiley-VCH GmbH. (h) Electron localization function. (i) Raman spectra of the $\nu(SO_4^{2-})$ band for different anodes. (j) In situ Raman spectra of weak hydrogen-bond proportions evolution during deposition. (k) Ea for different anodes.[89] Copyright 2025, Wiley-VCH GmbH. (l) A cross-sectional TEM image and corresponding EDS mappings of the ZVO@Zn anode. (m) The contact angle measurements and (n) the nucleation overpotentials of the Zn and ZVO@Zn anodes.[92] Copyright 2024, American Chemical Society.

relevant criterion is whether the interphase can maintain a stable Zn^{2+} concentration field as Zn^{2+} is continuously consumed. Thus, ion-channel design should be evaluated together with dynamic concentration polarization rather than solely by equilibrium diffusion energetics.

4.1.2 H_2O regulation for suppressed side reactions

A second route is to directly regulate interfacial H_2O. Notably, hydrophobic interphases exclude water from the Zn surface, whereas hydrophilic interfaces immobilize or reorganize H_2O through specific interactions. Although these mechanisms appear opposite, both seek to reduce the population of electrochemically active water participating in the Zn^{2+} hydration environment.

For example, hydrophobic fluorine (F)-axial-coordinated single-atom catalysts (F-Sb SAs) simultaneously regulate interfacial water and accelerate Zn^{2+} desolvation through electron delocalization and p-p orbital hybridization (**Figure 3h**).[89] Raman spectroscopy shows a shift of the $\nu(SO_4^{2-})$ band toward higher wavenumbers on F-Sb SAs@Zn, corresponding to an increased proportion of contact ion pairs and indicating enhanced dehydration of the Zn^{2+} solvation sheath (**Figure 3i**). More importantly, in situ Raman spectroscopy during Zn deposition reveals that F-Sb SAs@Zn consistently maintained a higher fraction of weakly hydrogen-bonded water than bare Zn (**Figure 3j**), providing direct dynamic evidence for facilitated water removal from hydrated Zn^{2+}. Consistently, the desolvation activation energy decreased from 33.52 kJ mol^{-1} to 13.42 kJ mol^{-1} (**Figure 3k**), supporting stable cycling for 1200 h at 20 mA cm^{-2} and 5 mAh cm^{-2}.

Conversely, hydrophilic interphases can suppress water activity by immobilizing water within strong interfacial H-bond networks. A phytic-acid-Zn/polyanionic hydrogel constructs a three-dimensional dehydrated interface, exhibits excellent cycling stability at a high current density of 10 mA cm^{-2}, overcoming the bottleneck of rapid short-circuit failure in bare Zn at high currents. [90] Building on this, the concepts of "spatial confinement and ion sieving" were introduced, including the construction of a dual interfacial layer comprising zinc phytate and halloysite nanotubes (HNTs).[91] Within this structure, phytic acid molecules are responsible for hydrophilic desolvation, while halloysite provides a nanoscale "ion sieve" *via* its surface charges and inner cavity structure.

Currently, the functional design of SEIs is advancing toward multifunctional synergy, integrating the regulation of water molecules with the guidance of zinc ion deposition. For instance, Yoo *et al*. constructed an ultrathin, multifunctional zinc vanadium oxide (ZVO) surface coating (**Figure 3l**), proposing a strategy that unifies "hydrophilic and zincophilic synergy".[92] The polar oxygen sites in this coating are responsible for tearing the hydration shell and actively capturing water molecules (hydrophilicity; **Figure 3m**; further lowering the desolvation activation energy Ea); simultaneously, the metal oxide lattice with high zinc affinity acts as atomic-level nucleation sites, significantly reducing the nucleation overpotential (zincophilicity; **Figure 3n**). This synergistic effect enables the anode to operate even under current shocks of 10 mAh cm^{-2} or higher.

A critical issue is therefore not whether an interface is simply “hydrophobic” or “hydrophilic”, but whether it selectively lowers the activity of interfacial water while preserving rapid Zn^{2+} transport. Excessive exclusion, confinement, or binding of solvent molecules may otherwise replace a desolvation limitation with an interfacial mass-transfer limitation. XFC-oriented SEIs should consequently be assessed by the coupled evolution of water activity, Zn^{2+} flux, and interfacial resistance under realistic areal capacities.

4.2 Electrolyte regulation: liquid electrolyte solvation structure

Unlike artificial SEIs, electrolyte regulation modifies the solvation environment before Zn^{2+} reaches the anode. The central design trade-off is between reducing water activity and avoiding overly stable Zn^{2+}-additive coordination that must subsequently be broken during deposition. Accordingly, electrolyte strategies can be classified into inner and outer solvation sheaths of hydrated zinc ions.

4.2.1 Inner-sphere solvation structure for direct coordination with Zn^{2+}

In AZIBs, the primary solvation shell of hydrated zinc ions, $[Zn(H_2O)_6]^{2+}$, is the fundamental origin of HER and passivation corrosion at the anode interface. A critical step toward enhancing fast-charging stability involves introducing additives with stronger coordination capabilities for Zn^{2+}, thereby directly substituting inner-sphere water molecules and altering the primary solvation structure. For instance, sucralose (SCL) forms an SCL-containing primary solvation shell $[Zn(SCL)_x(H_2O)_{6-x}]^{2+}$ and significantly reconfigures the global hydrogen-bond network.[93] Consequently, under XFC conditions of 30 mA cm^{-2} and deep discharge (depth of discharge, DOD = 73.3%), the Zn//Zn symmetric cell achieves stable cycling for 171 h, while the Zn//Cu cell delivers a high

CE of 99.61%. Moreover, folded multifunctional molecules can penetrate the inner shell *via* multisite coordination,effectively displacing 2-3 active water molecules and forming a multisite-coordinated $[Zn(MGM)_x(H_2O)_y]^{2+}$ solvation cluster (**Figure 4a**).[94] Arrhenius fitting reveals a remarkable reduction in the desolvation activation energy to 34.76 kJ mol^{-1} (**Figure 4b**). Consequently, the anode exhibits stable plating/stripping profiles even under 20 mA cm^{-2} (5 mAh cm^{-2}) (**Figure 4c**).

More complex coordination architectures further illustrate that solvation engineering can affect both ion transport and interfacial chemistry. Sodium succinate (DS) can bridge two Zn^{2+} centers to form a bisolvation-sheath-bichelation configuration (i.e., a Zn^{2+}-DS^{2-}-Zn^{2+} structure), thereby completely breaking the constraints of traditional mononuclear coordination (**Figure 4d**).[95] Rather than inducing tension, this dinuclear chelation promotes charge delocalization, effectively reducing electrostatic repulsion between adjacent Zn^{2+} ions and accelerating Zn^{2+} migration (**Figure 4e and f**). Upon migrating to the anode interface, the BSB cluster undergoes competitive anion desolvation, as visualized by AIMD simulations (**Figure 4g**), drastically lowering the desolvation energy barrier. The zinc anode demonstrates excellent fast-charging rate capabilities up to 30 mA cm^{-2}. Meanwhile, poly (ionic liquid)s (PILs) and solvent-tailored triflate electrolytes (STTE) couple solvation reconstruction with interphase formation. PILs utilize dense polar groups to replace the primary hydration layer, forming a polymer-wrapped coordination network.[96] As these clusters migrate to the anode, the coordinating groups directly participate in interfacial electrochemical coupling and decomposition, generating a robust SEI protective layer, supporting long-term cycling (1000 h) under 10 mA cm^{-2}. [96] Moreover, ether solvents in STTE alter the global hydrogen-bond network and introduce steric hindrance, forcibly pulling $CF_3SO_3^-$ anions into the inner shell to form contact ion pair (CIP) or aggregate (AGG) structures.[97] The anion-rich sheath preferentially decomposes at the interface to generate protective SEIs, enabling the STTE to maintain stable cycling for over 450 h under 10 mA cm^{-2} and 20 mAh cm^{-2}, with a DOD up to 68%.

However, stronger coordination is not necessarily equivalent to faster charging. Although replacing H_2O can lower water activity and suppress HER, excessively stable additive-Zn^{2+} or anion-Zn^{2+} interactions may create a new energetic penalty during desolvation. Inner-sphere design therefore requires an optimal, rather than maximal, coordination strength and should be evaluated in terms of both solvation stability and actual charge-transfer kinetics.

4.2.2 Outer-sphere solvation structure for surrounding solvation

Unlike the direct substitution of coordinated water molecules in the inner shell, the regulation of the outer-sphere (secondary) solvation structure aims to modify steric interactions and hydrogen-bond networks surrounding hydrated Zn^{2+}. This approach can weaken Zn^{2+}-H_2O interactions while avoiding the kinetic penalty associated with strong inner-sphere coordination.

Large molecules such as sucrose accumulate outside the primary solvation shell and use steric effects to perturb the hydration environment. [98] Specifically, this outer-sphere enrichment leverages significant steric hindrance to expand the Zn^{2+} solvation sheath volume, pulling and substantially weakening the inner Zn^{2+}-H_2O interactions and constructing a water-shielding electric double layer (EDL) at the anode, enabling stable cycling of 625 h at 10 mA cm^{-2} and 10 mAh cm^{-2}.

Proline reconstructs the surrounding H-bond network while maintaining an organic-free primary solvation shell (**Figure 4h**).[99] Theoretical calculations indicate that the strong binding energy between Pro and water molecules (-1.21 eV) is much higher than the intrinsic hydrogen-bond interactions between water molecules (-0.31 eV) (**Figure 4i**), enabling the additive to disrupt the frozen network among bulk water molecules completely. Meanwhile, EXAFS wavelet transforms spectra visually confirm the maintenance of an organic-free primary solvation structure in the system. Similarly, dimethyl hydroxymethylphosphonate interacts with Zn^{2+} *via* low-affinity coordination, facilitating localized dehydration, while its peripheral hydroxyl groups firmly lock the active water molecules in the outer sphere.[100] This mechanism effectively mitigates strong solvation constraints, significantly reducing the desolvation Ea from 46.23 kJ mol^{-1} to 36.33 kJ mol^{-1}, enabling the Zn//Zn symmetric cell to operate stably for over 4500 h under 5 mA cm^{-2}.

Although theoretical calculations, structural characterizations, apparent desolvation activation energies, and cell-level electrochemical tests provide valuable mechanistic and kinetic information, they offer limited direct insight into the transient evolution of interfacial solvation under operating conditions. In acetonitrile (ACN)-containing electrolytes, ACN can construct a "catcher" network by forming strong O-H···N hydrogen bonds with water molecules.[101] In situ Raman further shows that the C≡N band remains unchanged during Zn plating/stripping, without the

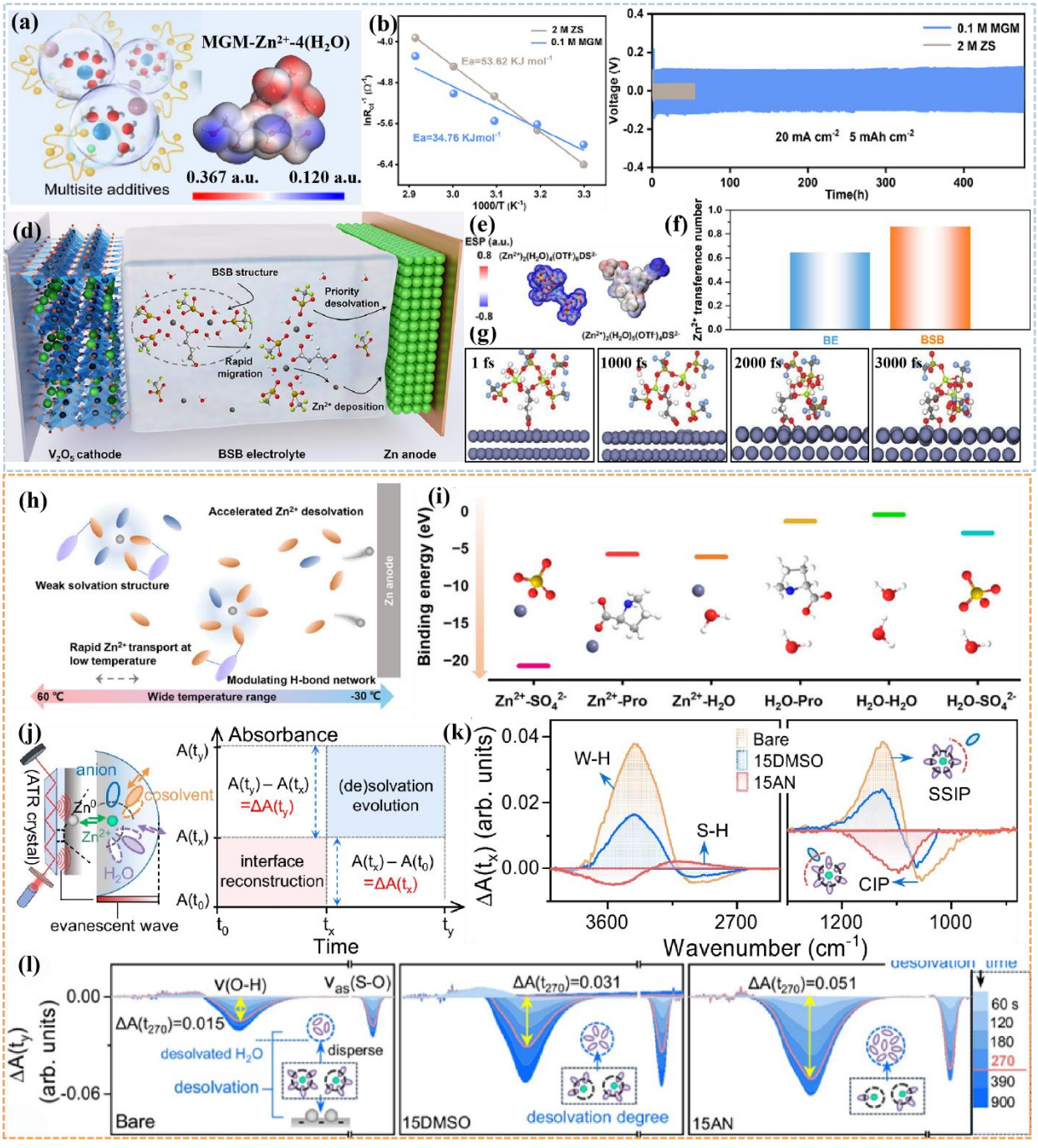


Figure 4. (a) Multisite additives (MGM) and ESP mapping of the solvated structures of pristine Zn^{2+}-6(H_2O) and MGM-Zn^{2+}-4(H_2O). (b) Arrhenius curves and comparison of the activation energies. (c) Cycling performance of Zn//Zn symmetric batteries based on ZS and MGM electrolytes under 20 mA cm^{-2}.[94] Copyright 2025, Wiley-VCH GmbH. (d) Scheme of the Zn^{2+} solvation and desolvation process in the BSB electrolyte. (e) Electrostatic potential mapping. (f) Comparison of the Zn^{2+} transference numbers in the BE electrolyte and the BSB electrolyte. (g) The desolvation process of $(Zn^{2+})_2(H_2O)_5(OTf^-)_4DS^{2-}$ simulated by AIMD.[95] Copyright 2025, Wiley-VCH GmbH. (h) The working mechanism of P-4 electrolyte. (i) Binding energies between different components in Pro/$ZnSO_4$ electrolyte.[99] Copyright 2025, Wiley-VCH GmbH. (*j*) Schematic of electrochemical in situ FTIR. The process can be decoupled into two stages: abrupt change of interface reconstruction (expressed as ΔA(tx) = A(tx) − A(t0)) and gradual change of (de)solvation evolution (expressed as ΔA(ty) = A(ty) − A(tx)). (k) ΔA(tx) comparison of three electrolytes during deposition. (l) The ΔA(ty) evolution of ν(O-H) and νas(S-O) during desolvation.[102] Copyright 2025, Wiley-VCH GmbH.

emergence of new coordination features, supporting that ACN mainly facilitates interfacial desolvation rather than dynamically reconstructing the primary Zn^{2+} solvation shell in bulk electrolyte. Building on this, Yu *et al*. employed time-resolved in situ FTIR during Zn plating at an absolute current of 10 mA for 900 s to directly monitor the (de)solvation process during Zn plating/stripping (**Figure 4j**).[102] Upon current application, an abrupt reconstruction of the interfacial H-bond and ion-pairing environment was first observed (**Figure 4k**), followed by gradual evolution of the O-H and S-O signals during desolvation (**Figure 4l**). These results demonstrate the capability of advanced in situ spectroscopy to capture transient interfacial solvation dynamics and highlight the need to extend such measurements to XFC-relevant high-current-density conditions. Future studies should further integrate high-current in situ Raman/FTIR with operando synchrotron X-ray absorption techniques to correlate transient solvent/anion redistribution with changes in the local Zn^{2+} coordination environment under realistic XFC conditions.

Overall, inner-sphere regulation directly reconstructs the primary Zn^{2+} solvation shell and more strongly suppresses water activity, but overly strong coordination may increase the desolvation penalty. Outer-sphere regulation better preserves fast Zn^{2+} transport, although its regulation of water activity is more indirect.

5. Balancing kinetics and uniformity *via* electrode design

Although microscale desolvation regulation reduces interfacial polarization, stable fast charging also requires mesoscale electrode designs that homogenize ion/electron flux and maintain large-area deposition uniformity. In this section, Zn-foil and Zn-powder electrodes are distinguished according to their electrode forms and dominant modification approach for XFC. Zn foils are planar metallic substrates, for which the key issue is to activate the surface and regulate nucleation, crystallographic orientation, and local deposition kinetics. In contrast, Zn powders form high-surface-area particulate networks, where particle contact, electronic/ionic percolation, electrode porosity, corrosion exposure, and volume/structural stability become more critical. Therefore, Section 5.1 focuses on improving the kinetic uniformity of Zn foils, whereas Section 5.2 focuses on stabilizing Zn-powder architectures under high-flux operation, with representative strategies and performance metrics summarized in **Table 2**.

5.1 Activating zinc foils

To mitigate the inherent electrochemical sluggishness and dendrite growth on planar zinc foils, diverse strategies are systematically categorized based on their roles in reshaping nucleation thermodynamics (zincophilic sites), guiding crystallographic growth (preferred planes), and redistributing local current densities through geometric reconstruction (3D designs).

5.1.1 Zincophilic sites

Under high-current fast-charging conditions, the intrinsically high nucleation overpotential of zinc foil anodes typically leads to sluggish interfacial deposition kinetics. This thermodynamic inertia easily triggers uncontrolled nucleation, forming massive initial nuclei locally that subsequently evolve into destructive dendrites. Therefore, introducing "zincophilic sites" with strong Zn^{2+} interactions at the anode/electrolyte interface—thereby reshaping the thermodynamic and kinetic environment to lower the nucleation barrier—is a primary strategy for enabling stable high-rate operation of zinc foils.

Constructing zincophilic sites utilizing the strong thermodynamic affinity of heterometallic interfaces is a direct and effective approach. Among various zincophilic elements, copper (Cu) has been extensively studied due to its low nucleation barrier. Zheng *et al*. directly employed a commercial brass ($Cu_{0.7}Zn_{0.3}$) solid solution alloy as the anode.[103] Theoretical calculations and kinetic characterizations revealed that this reduced nucleation overpotential of zinc ions originates from the accelerated interfacial charge transfer. To further optimize the distribution of Cu sites, Liu *et al*. proposed a modification strategy utilizing Cu^{2+}-preloaded layered kaolin.[104] During cycling, the in situ reduced Cu^{2+} forms spatially gradient Cu_xZn_y alloy nucleation sites, further achieving improved performance. With the development of computational chemistry, Zhao *et al*. systematically screened optimal zincophilic carriers from the perspectives of thermodynamic inertia and kinetic zincophilia.[105] The resulting Bi@Zn hetero-metallic interface exhibited outstanding kinetic performance. Theoretical and experimental results confirmed that Bi sites maximally reduce the nucleation barrier and accelerate interfacial charge transfer. Benefiting from this kinetic enhancement, the corresponding symmetric cell delivered an ultra-low overpotential of ~55 mV and an exceptional lifespan of over 4700 cycles at a high current density of 10 mA cm^{-2}.

Table 2. Zn electrode strategies for balancing kinetics and uniformity.

Anode type		Tafel		Symmetric cell						Full cell			
				Kinetic descriptor									
		Corrosion potentials	Corrosion J (mA cm^{-2})	Ea (kJ/mol)	Overpotentials reduction rate (%)	J (mA cm^{-2})	Q_{Area} (mAh cm^{-2})	Time (h)	XFC regime	Type	Current density	Cycle number	Capacity retention (%)
Activating zinc foils	Zn/Brass[103]	−9.95 mV	0.26	NR	22.8%	1	1	1400	III	Zn/Br_2	20 A g^{-1}	50	98.53
						10	10	420					
	Zn@CuCK[104]	−0.982 V	0.659	36.16	58.8%	5	2	2300	II	Zn@CuCK/NVO	5 A g^{-1}	12000	83.5
						10	5	1100					
	Bi@Zn[105]	−0.978V	0.21	45.17	NR	10	5	2000	II	Bi@Zn/MnO_2	0.1 A g^{-1}	150	85.3
	Nuclei-rich electrode[51]	−0.976V	0.23	48.6	43.9%	1	1	4000	III	Zn/ MnO_2	10C	3000	99
						15	10	1200					
	T-Zn[106]	−0.84 V	0.42	35.7	72.8%	5	1	2500	II	T-Zn/I_2	1.5 A g^{-1}	5000	83.4
						10	1	400					
	NMIF@Zn[108]	−1.133 V	0.32	16.7	22.5%	3	3	2000	III	NMIF@Zn/MnO_2	1 A g^{-1}	1000	82.3
						20	10	1000					
	3D-Zn@ZnSe[107]	−0.965 V	0.092	36.66	78.7%	0.5	0.5	2000	II	3D-Zn@ZnSe/V_2O_5	5 A g^{-1}	8500	90.63
						10	3	200					
Consolidating zinc powder anode	GIZ[114]	−1.064 V	6.82	NR	50%	1	1	3000	I	Zn/NVO	2 A g^{-1}	1000	61.2
	3D Zn@ZAP[129]	−0.954 V	0.31	NR	NR	5	5	4700	III	3D Zn@ZAP/MnO_2	1.7 A g^{-1}	500	68.4
						10	10	1750					
	Zn powder/PG[127]	−0.951 V	0.38	17.1	36.5%	5	1	400	I	Zn powder/PG/MnO_2	1 A g^{-1}	100	72
						5	0.5	360					
	ZP-NC[119]	−1.015 V	1.82	34.44	NR	1	1	900	II	ZP-NC/NVO	4 A g^{-1}	1100	75.7
						5	5	170					
	PC41@ZnP[121]	−0.893 V	0.78	NR	46.2%	1	1	1600	I	PC41@ZnP/MnO_2	10 C	2000	77.3
						5	1	900					
	MXene@Zn[112]	−0.918 V	0.45	NR	28.1%	1	1	200	I	MXene@Zn/FeHCF	1 A g^{-1}	1000	77
	Zn-PD[116]	−1.005 V	0.98×10^{-3}	NR	50.0%	1	1	200	I	Zn-PD/NVO	0.5A g^{-1}	200	72.3
	LSZ[115]	−0.858 V	0.013	NR	35.9%	1	0.5	2000	I	LSZ/V_2O_5	1A g^{-1}	2000	79.1
	SLA[125]	−0.902 V	0.32	NR	NR	5	5	450	III	SLA/V_2O_5	10 A g^{-1}	5000	75
						10	10	100					
	P-A2@NH_2[124]	−0.953 V	0.04	10.13	36.5%	2.5	0.5	8300	IV	P-A2@NH_2/AlVO-H_2O	2A g^{-1}	500	91.9
						25	25	2000					
	ZMA@3D Zn[130]	−0.910 V	0.29	NR	50.7%	10	10	890	III	ZMA@3D-Zn/MnO_2	5 A g^{-1}	500	84.8
						20	20	1153					
	Passivated Zn-P[117]	−0.925 V	0.22	NR	NR	3	3	70	II	Zn/MnO_2	1 A g^{-1}	250	71.8
	C@Zn-P[111]	−0.901 V	0.19	NR	36.6%	1	0.5	600	I	C@ZnP/MVO	1 A g^{-1}	1000	81.4
	DDA-MXene@Zn-p[113]	−0.957 V	0.279	NR	46.2%	1	1	450	I	DDA-MXene@Zn-p/MnO_2	1 A g^{-1}	1000	82.2
	Zn@C-5[126]	−0.903 V	0.26	NR	85.6%	1	1	880	II	Zn@C5/MnO_2	0.5 A g^{-1}	800	>75
						5	5	180					
	ZP/DDP[120]	−0.889 V	0.24	NR	NR	2	2	700	II	ZP/DDP/I_2/DDP	1.7 A g^{-1}	1200	100
						5	5	200					
	APS[128]	−0.882V	0.77	NR	NR	5	1	5000	I	APS/MnO_2	20 mA cm^{-2}	7500	100
	Zn-P-MIEC[123]	−0.868 V	0.00789	14.22	NR	10	1	100	II	Zn-P-MIEC/MnO_2	0.5A g^{-1}	1500	90
	ZnP-FC[122]	−0.98 V	1.28	NR	NR	5	1	1650	II	ZnP-FC/KVOH	5 A g^{-1}	6000	85
						5	5	570					

Note:

(1) Zinc/brass electrode (Zn/Brass); Cu^{2+}-carboxymethyl chitosan-kaolin layer-modified Zn (Zn@CuCK); bismuth-zinc hetero-metallic interface (Bi@Zn); micro-terraced Zn (T-Zn); nuclei-rich Zn electrode (nuclei-rich electrode); NaMgF3/Na3InF6 nanocube interphase-modified Zn (NMIF@Zn); polyporous three-dimensional Zn framework with a zincophilic ZnSe overlayer (3D-Zn@ZnSe); GaInZn alloy-coated Zn (GIZ); three-dimensional printed Zn scaffold coated with Zn-alginate/polyacrylamide hydrogel (3D Zn@ZAP); zinc powder/pristine graphene hybrid electrode (Zn powder/PG); nano-copper-modified Zn powder (ZP-NC);

polytetrafluoroethylene/carboxymethyl cellulose 4:1 binder-modified Zn powder (PC41@ZnP); Ti3C2Tx MXene-wrapped Zn powder (MXene@Zn); poly(ethylene glycol) diacrylate-modified Zn powder (Zn-PD); liquid metal-skinned Zn powder (LSZ); semi-liquid Zn powder anode (SLA); soft-elastic amino-functionalized polymer-modified Zn powder (P-A2@NH2); zinc methacrylate-modified three-dimensional printed Zn powder anode (ZMA@3D Zn); passivated Zn powder (passivated Zn-P); amorphous carbon-coated Zn powder (C@Zn-P); dimethyldiallylammonium chloride-assisted Ti3C2Tx MXene-modified Zn powder (DDA-MXene@Zn-p); glucose-derived amorphous carbon-coated Zn powder with a Zn:C ratio of 5:1 (Zn@C-5); diisocyanate-poly(tetrahydrofuran) dihydrazide binder-modified Zn powder (ZP/DDP); artificial protrusion strategy (APS); mixed ionic-electronic conducting scaffold-supported Zn powder (Zn-P-MIEC); biomimetic quasi-skin-capillary Zn powder anode with ionic-electronic conducting full-chain networks (ZnP-FC).

(2) XFC regime is classified using current-density/areal-capacity framework; for strategies reported under multiple symmetric-cell conditions, the highest reached regime is used:

Regime I, fundamental evaluation (j<5 mA cm^{-2} and Q_{areal} ≤1 mAh cm^{-2});

Regime II, moderate fast charging (j≤10 mA cm^{-2} and Q_{areal}≤5 mAh cm^{-2});

Regime III, single-factor XFC-relevant stress (j>10 mA cm^{-2} or Q_{areal}>5 mAh cm^{-2} or DODZn≥10%);

Regime IV, coupled high-current/high-areal-capacity XFC-relevant condition (j>20 mA cm^{-2} and Q_{areal}>5 mAh cm^{-2}).

Highly electronegative polar groups rich in lone-pair electrons (e.g., -OH) can also strongly coordinate with Zn^{2+}, serving as effective nucleation-inducing centers. Inorganic minerals and natural biomass macromolecules are ideal structural carriers for these polar sites. Zou *et al*. constructed a "nuclei-rich" inducing interface using -OH-rich hydroxyapatite (**Figure 5a**).[51] The strong adsorption of Zn^{2+} by -OH groups significantly facilitated the desolvation process, reducing the interfacial activation energy from 66.0 to 48.6 kJ mol^{-1}. Kinetic characterizations demonstrated that the exchange current density of the modified interface increased from 10.19 to 17.04 mA cm^{-2}, driving the zinc deposition mechanism from conventional instantaneous nucleation to a high-rate progressive nucleation mode (**Figure 5b**). Empowered by this kinetic enhancement, the symmetric cell achieved over 1, 200 hours of dendrite-free cycling under 15 mA cm^{-2} and 10 mAh cm^{-2} (**Figure 5c**).

5.1.2 Preferred crystal planes

Due to the hexagonal close-packed (hcp) crystal structure of Zn, its various crystallographic planes (e.g., (002), (100), (101)) exhibit pronounced anisotropy in atomic packing density, surface energy, and charge distribution. This crystallographic anisotropy directly causes an uneven electric-field distribution and kinetic discrepancies during Zn^{2+} deposition at the anode/electrolyte interface, making the anode highly susceptible to dendrite growth and side reactions. Therefore, regulating the preferred crystal orientation *via* interface engineering—guiding zinc ions to deposit in an orderly manner along specific thermodynamically or kinetically favorable planes—is a critical pathway to resolving the intrinsic instability of zinc anodes at high rates.

Among the various crystal planes, the (002) plane features the highest atomic packing density and the lowest surface energy in zinc crystals. Guiding zinc deposition along the (002) plane not only provides a flat 2D lateral growth platform but also significantly suppresses water-induced side reactions owing to its thermodynamic stability. However, the close-packed structure of the (002) plane inevitably results in relatively sluggish reaction kinetics. In contrast, certain non-(002) planes exhibit faster charge-transfer and deposition kinetics. Provided they are effectively induced and regulated by specific interfacial fields, these non-(002) planes can also overcome the risk of disordered growth, achieving highly uniform and dense deposition. This strategy not only offers excellent interfacial stability but also endows the electrode with rapid response capabilities that far exceed those of the (002) plane, breaking the exclusivity of conventional (002) textures.

In practice, manipulating a single crystal plane often involves a trade-off between thermodynamics and kinetics: the (002) plane is exceptionally stable but kinetically sluggish, whereas high-energy planes (e.g., (100)) offer ultra-fast kinetics but are prone to severe interfacial side reactions. To address this compromise, constructing a multi-plane synergistic "micro-terraced surface" is an advanced solution. Zhang *et al*. treated Zn foils in an aqueous TiF_4 solution to induce redox-driven, crystallographically anisotropic surface dissolution. Ti^{4+} acts as a mild oxidant and is reduced to Ti^{3+}, while surface Zn is oxidized to soluble Zn^{2+}.[106] Preferential dissolution at under-coordinated sites then drives surface reconstruction into a micro-terraced morphology composed of (002) basal terraces

Table 3. Polarization reduction of representative Zn-electrode strategies.

Anode type		*J* (mA cm^{-2})	Before modification (mV)	After modification (mV)	Polarization reduction (%)
Activating zinc foils	Zn/Brass[103]	10	57	44	22.8%
	Zn@CuCK[104]	0.4	68	28	58.8%
	Zn@CuCK[104]	5	NR	38	NR
	Nuclei-rich electrode[51]	5	96.1	53.9	43.9%
	Bi@Zn[105]	5	72.4	25.4	64.9%
	Nuclei-rich electrode[51]	1	70.5	15.2	78.4%
	3D-Zn@ZnSe[107]	0.5	85.4	18.2	78.7%
Consolidating zinc powder anode	T-Zn[106]	NR	15.1	4.1	72.8%
	3D Zn@ZAP[129]	NR	NR	NR	NR
	NMIF@Zn[108]	1	51.6	40.0	22.5%
	ZP-NC[119]	NR	NR	NR	NR
	3D-Zn@ZnSe[107]	1	50.9	35.7	29.9%
	MXene@Zn[112]	1	38.1	27.4	28.1%
	GIZ[114]	NR	80	40	50.0%
	3D Zn@ZAP[129]	0.2	64	41	35.9%
	SLA[125]	NR	NR	NR	NR
	Zn powder/PG[127]	NR	52	33	36.5%
	ZMA@3D Zn[130]	10	102.9	50.7	50.7%
	ZP-NC[119]	NR	NR	NR	NR
	C@Zn-P[111]	10	124	79	36.3%
	PC41@ZnP[121]	1	65.3	35.1	46.2%
	Zn@C-5[126]	1	130.82	18.91	85.6%
	MXene@Zn[112]	NR	NR	NR	NR
	Zn-PD[116]	NR	NR	NR	NR
	LSZ[115]	NR	NR	NR	NR
	SLA[125]	NR	NR	NR	NR

Note: Table 3 supplements **Table 2** by detailing specific polarization conditions and values of before/after modifications, whereas Table 2 highlights the reduction percentages for clearer comparison. Data for Polarization reduction (%) of Table 2 is calculated based on Table 3.

and (100) side planes (**Figure 5d**). The distinct Zn^{2+} adsorption energetics of the (002), (100), and their interfacial sites direct Zn migration toward the terrace boundaries, converting disordered surface diffusion into directional 2D diffusion (**Figure 5e and 5f**). The coupled terrace diffusion and edge anchoring improve high-rate kinetics while maintaining interfacial stability, enabling low plating/stripping polarization even at 20 mA cm^{-2}.

5.1.3 3D anode design

Under high-current fast-charging operations, 3D structured anode design is another effective strategy to improve zinc deposition kinetics. The core mechanism involves constructing a highly porous, conductive framework to drastically increase the electrochemically active surface area (Areal), thereby significantly reducing the local interfacial current density (J_{local} = J/A_{real}). Bie *et al*. utilized a one-step electrochemical scanning technique to in situ reconstruct a polyporous 3D-Zn framework on a planar zinc foil, simultaneously coating it with a zincophilic ZnSe overlayer.[107] This intrinsically reconstructed 3D zinc host not only precisely repaired inherent surface defects but also effectively lowered the local current density and buffered the volumetric stress during plating/stripping.

With a deeper understanding of the microscopic behavior of anodes under fast-charging conditions, researchers have increasingly recognized that the introduction of zincophilic sites, the preferential induction of specific crystal planes, and 3D structural designs are deeply intertwined. For example, Yang *et al*. developed a novel composite-phase $NaMgF_3/Na_3InF_6$ nanocube interphase (NMIF@Zn) that undergoes dynamic *in situ* reconstruction into a stratified architecture during electroplating (**Figure 5g**).[108] Through the synergistic regulation of this stratified interface, the preferential reduction of In^{3+} forms a zincophilic metallic in the inner layer, while the outer layer retains the negatively charged fluoride nanocubes. This reconstructed interphase not only strengthens the EDL structure (**Figure 5h**) but also establishes unhindered ion channels rich in zincophilic sites, significantly lowering the ion migration barrier and nucleation overpotential to enable conformal, dendrite-free deposition. As a result, the

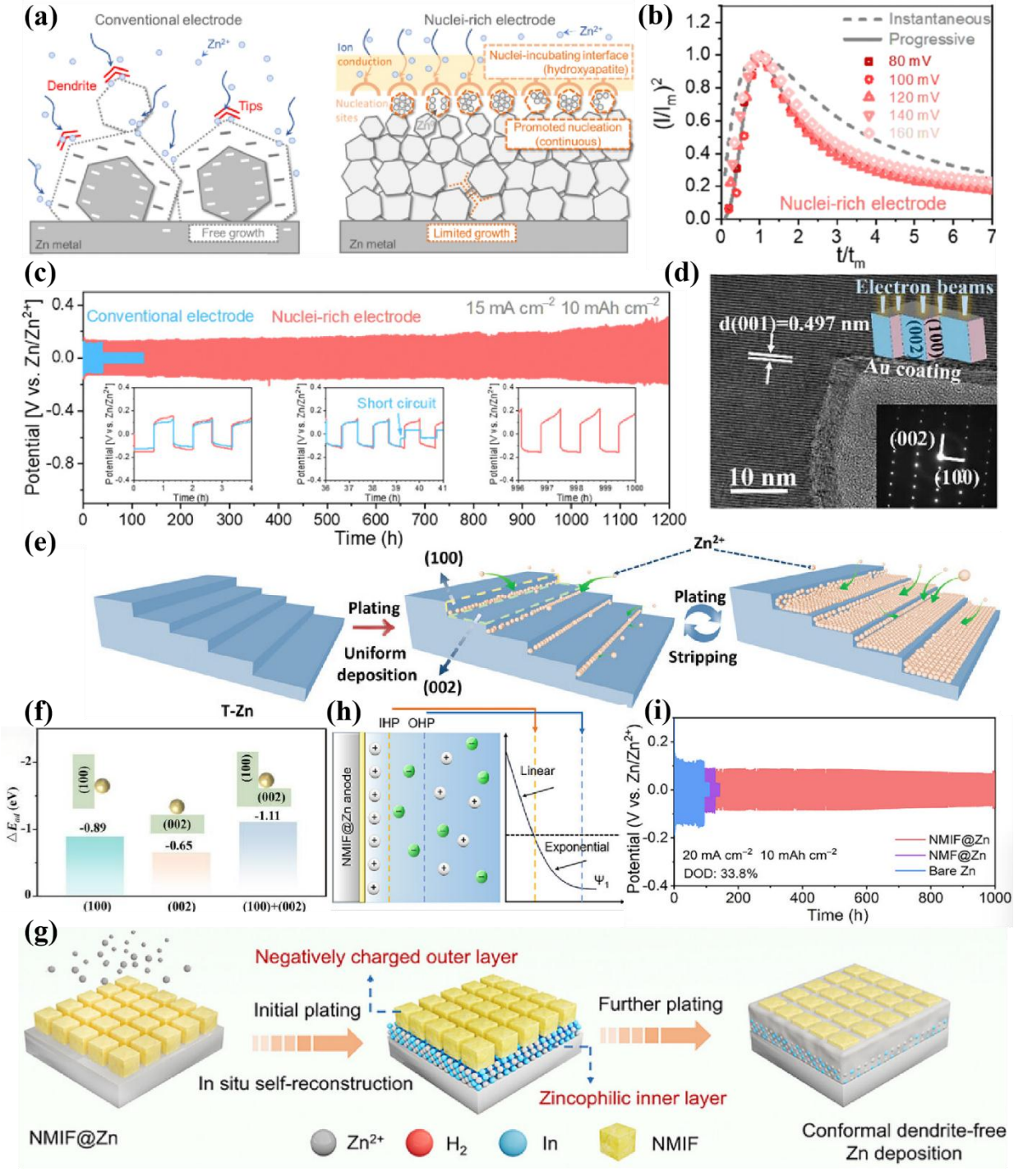


Figure 5. (a) Schematic of Zn plating on conventional and nuclei-rich Zn electrodes. (b) $(I/Im)^2$-(t/tm) curves from the current response in chronoamperometry plating of Zn at nuclei-incubating interfaces. (c) Long-term cycling profiles of Zn symmetric cells with a current density of 15 mA cm^{-2}.[51] Copyright 2023, The Royal Society of Chemistry. (d) HRTEM image of T-Zn. (e) Schematics of the Zn plating on P-Zn and T-Zn. (f) Adsorption energy of Zn^{2+} on the (100), (002), and (100)/(002) crystal planes of metallic Zn.[106] Copyright 2026, Wiley-VCH GmbH. (g) Schematic diagram of the in situ self-reconstruction process on the NMIF@Zn anode. (h) Schematic of the EDL structure of NMIF@Zn with a reinforced Zn^{2+} concentration. (i) Potential profiles of symmetric cells using different electrodes at 20 mA cm^{-2}.[108] Copyright 2026, Wiley-VCH GmbH.

NMIF@Zn anode demonstrated excellent plating/stripping reversibility under the stringent conditions of 20 mA cm^{-2} and 10 mAh cm^{-2} (**Figure 5i)**.

Overall, zincophilic-site engineering lowers the nucleation barrier, crystallographic regulation guides ordered Zn growth, and 3D architectures reduce the local current density. However, each strategy addresses only part of the kinetics-uniformity trade-off, while excessive surface activation or structural complexity may introduce additional side reactions and instability. Their integration is therefore more promising for XFC than maximizing any single factor alone.

5.2 Consolidating zinc powder anode

Compared with planar Zn foils, Zn powders provide a much larger electrochemically active area, which lowers local current density and facilitates rapid nucleation. However, the same high surface area also increases Zn/electrolyte contact, intensifying corrosion, HER, and volume-induced structural instability under XFC. Current stabilization strategies are systematically categorized into three dimensions: zinc powder modification, functionalization of auxiliary components, and structural design of electrode architectures.

5.2.1 Zinc powder modification

The particle size distribution and morphology of Zn powders are intrinsic structural parameters that influence particle packing, electrode porosity, local electric-field distribution, and Zn^{2+} transport. Zhao *et al*. constructed a Zn powder electrode with through-thickness gradients in particle size and porosity, as confirmed by cross-sectional and layer-resolved SEM observations (**Figure 6a**).[109] Finite-element simulations reveal that this gradient architecture redistributes Zn^{2+} concentration and deposition sites across the electrode depth (**Figure 6b**), thereby promoting bottom-up Zn deposition rather than surface-localized growth (**Figure 6c**). In addition to particle size, morphology also affects interparticle compatibility and structural stability; Cao *et al*. showed that flake-type Zn powders exhibit enhanced compatibility with similarly shaped graphite, resulting in a more uniform local electric field and Zn deposition.[110] These results indicate that Zn powder size and morphology should be jointly optimized with electrode porosity and interparticle connectivity rather than treated as independent parameters.

Surface modification of Zn powders primarily serves two functions: regulating Zn deposition kinetics and suppressing water-induced parasitic reactions. Conductive carbon coatings establish continuous electronic pathways while homogenizing Zn deposition. Tang *et al*. synthesized amorphous carbon-coated Zn powders (C@Zn-P) by spraying and annealing; the carbon layer forms negatively charged COO^- and COH^- groups *via* water deprotonation, facilitating Zn^{2+} diffusion through electrostatic binding (81.4% capacity retention after 1000 cycles).[111] Li *et al*. wrapped Zn powders with $Ti_3C_2T_x$ MXene through electrostatic self-assembly, leveraging the low lattice mismatch (~10%) to establish continuous electronic channels while redistributing Zn^{2+} flux for uniform nucleation (> 1000 cycles with ~100% CE).[112] However, MXene's intrinsic hydrophilicity and weak adhesion to Zn limit long-term durability. Tang *et al*. addressed this by introducing dimethyl diallyl ammonium chloride (DMDAAC) as a dual-functional enhancer that strengthens MXene-Zn adhesion electrostatically while imparting superhydrophobicity (99.2% CE after 300 cycles).[113]

Zincophilic metallic coatings guide deposition and suppress corrosion through heterogeneous interfacial interactions. GaInZn alloy coatings lower the surface energy from 29.0 to 26.9 mN m^{-1} and reduce the nucleation overpotential from 15.1 to 4.1 mV, enabling preferential nucleation and corrosion suppression.[114] Interestingly, liquid metal-skinned Zn (LSZ) powders are a nanothick eutectic gallium-indium skin that conformally coats Zn powders and acts as an electrically conductive glue, eliminating the need for binders and carbon additives while guiding horizontal Zn growth along the (002) plane and restricting direct water contact (2000 h in symmetric cells; 99.998% capacity retention per cycle at 10 A g^{-1}).[115]

Polymer and inorganic interphases provide complementary routes to stabilize the highly exposed surface of Zn powders. For example, poly (ethylene glycol) diacrylate (PEGDA) hydrogel layers immobilize free water through multidentate hydrogen bonding, reducing the hydrogen evolution current density from 1.07 to 0.058 mA cm^{-2} at −0.1 V and the nucleation overpotential from 80 to 40 mV.[116] In contrast, inorganic interphases stabilize Zn powders mainly through physical or chemical passivation. Sun *et al*. demonstrated that a rapid chemical solution passivation generates a thin, dense oxide layer on Zn powder surfaces; the passivated anode cycles stably for 100 h at 3 mA cm^{-2} and 3 mAh cm^{-2} with a depth of discharge of 41.3%.[117] Ning *et al*. formed a biomimetic "dragon-scale" phosphate-rich interface through sodium tripolyphosphate-mediated electrolyte regulation, where STPP coordinates with Zn^{2+} to enable in situ formation of a chemically grafted protective

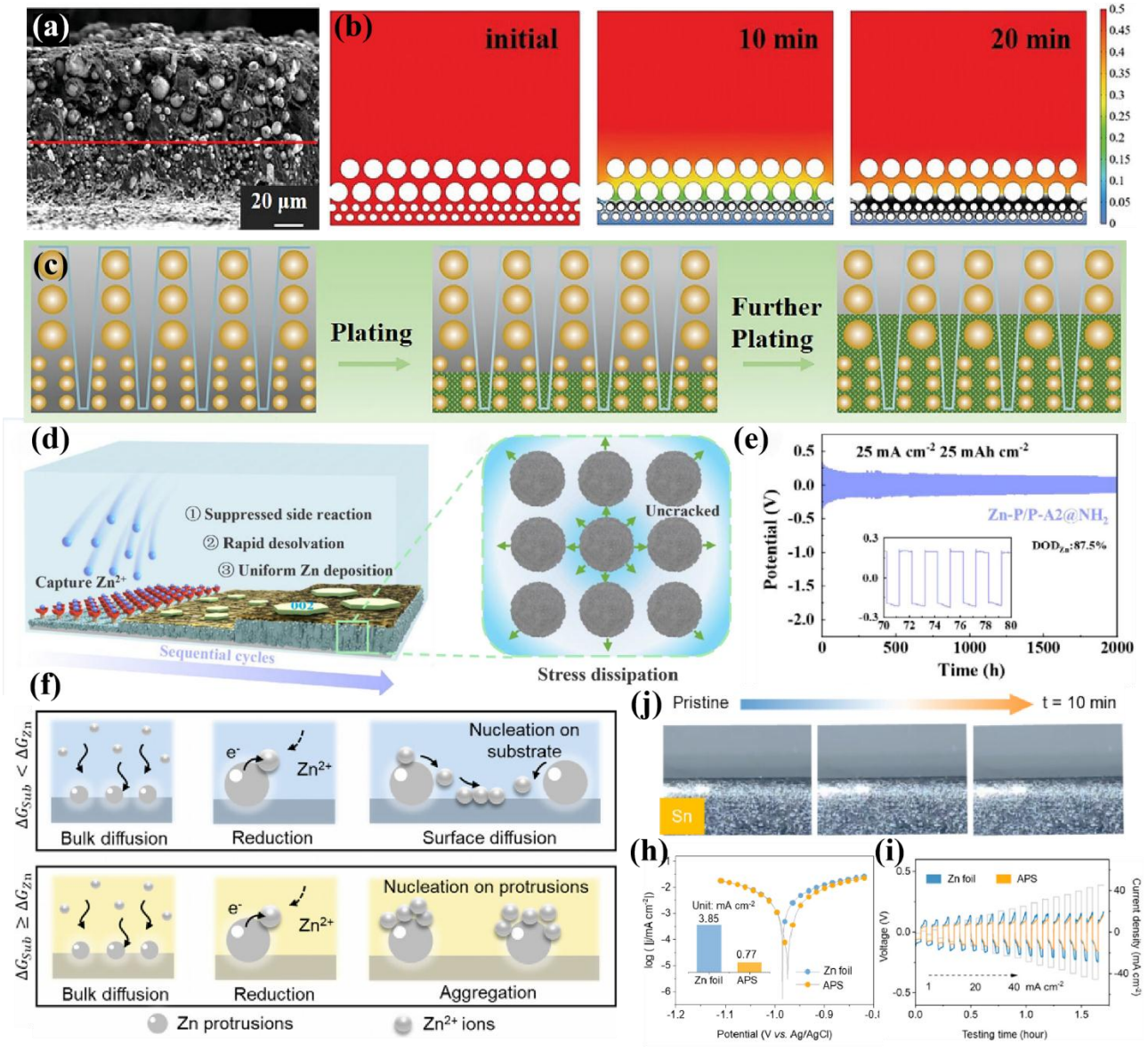


Figure 6. (a) SEM images of the ZP-Grad electrode. (b) The finite element simulations of different electrodes during the Zn deposition process. (c) Schematic diagram of desirable bottom-up and dendrite-free Zn deposition behavior in ZP-Grad electrode.[109] Copyright 2025, Wiley-VCH GmbH. (d) Stabilized morphology and regulated Zn deposition in the soft-elastic polymer-modified Zn-P anodes during cycling and stable structure of stress-relieving Zn-P/P-A2@NH_2 anode. (e) Cycling performance of Zn-P/P-A2@NH_2 electrodes under 25 mA cm^{-2} and 25 mAh cm^{-2}.[124] Copyright 2025, Wiley-VCH GmbH. (f) Zn deposition mechanisms on flat and protrusive Zn surfaces. (g) Optical microscopy observation of hydrogen evolution on the Sn substrate. (h) Tafel plots demonstrate corrosion of Zn anodes in a 2 M aqueous $ZnSO_4$ electrolyte. (i) Rate capability tests of Zn symmetrical cells based on the Zn foil and APS anodes.[128] Copyright 2025, American Chemical Society.

layer (> 900 h at 8.8 mA cm^{-2}; 60.8 mAh g^{-1} after 4000 cycles at 10 A g^{-1}).[118]

As discussed in Section 4.1, effective interphase regulation requires balancing rapid Zn^{2+} transport with interfacial water suppression. For Zn powder anodes, this principle should be further extended to the particulate electrode level by considering compatibility with auxiliary components, interparticle connectivity, and mechanical stability.

5.2.2 Engineering auxiliary components

Auxiliary components play a critical role in

maintaining interparticle transport and structural integrity in powder-based electrodes. Conductive additives can function as active deposition regulators rather than passive electron-conducting fillers. Jin *et al*. incorporated nano-copper powder as a functional conductive medium to replace conventional carbon black; the zincophilic Cu not only enhances electronic conductivity but also provides uniform nucleation sites for homogeneous Zn deposition (170 h at 5 mA cm^{-2} and 5 mAh cm^{-2}; 81 Wh kg^{-1} at N/P = 4.3).[119]

Polymer binders provide an additional means to couple Zn^{2+} regulation with mechanical stabilization. Wang *et al*. developed a diisocyanate-polytetrahydrofuran-dihydrazide (DDP) binder inspired by protein structures; strong Zn^{2+} coordination capability and dense hydrogen-bond arrays enable a free-standing, current-collector-free electrode while repelling coordinated water molecules to inhibit side reactions (stable cycling at 5 mAh cm^{-2}).[120] Lei *et al*. engineered a zincophilic-hydrophobic balanced binder combining polytetrafluoroethylene and carboxymethyl cellulose; PTFE creates a localized water-poor environment to suppress water-triggered side reactions while CMC provides zincophilic pathways for uniform Zn^{2+} transport (220 h at 50% utilization, 6.6 mAh cm^{-2}).[121] Extending beyond conventional binder formulations, Zheng *et al*. constructed a biomimetic quasi-skin-capillary structure using aramid nanofibers, in which the surface layer homogenizes Zn^{2+} flux and limits water contact, while the internal nanofiber network anchors Zn particles and provides selective ion-transport pathways, enabling stable operation even at 50 mA cm^{-2} with 195 mV overpotential.[122]

More integrated designs further combine ionic/electronic transport, stress buffering, and interfacial regulation within a single auxiliary network. Zhang *et al*. constructed mixed ionic-electronic conducting scaffolds using carbon nanotubes and ethylene-vinyl acetate copolymer *via* tape casting, in which the CNT-EVA composite serves as both the conductive additive and the binder, establishing a dual-conduction network that homogenizes Zn^{2+} ingress (100 h at 10 mA cm^{-2}).[123] Qin *et al*. introduced soft-elastic amino-functionalized polymer binders that form dynamically swelling 3D networks upon electrolyte infiltration, simultaneously mitigating internal stress through reversible volume expansion, reconstructing the Zn^{2+} solvation sheath to reduce free water content (**Figure 6d**), and preferentially adsorbing on Zn (002) planes to induce dense horizontal deposition. Benefiting from this design, the symmetrical cell operated > 2000 h at 25 mA cm^{-2} and 25 mAh cm^{-2}; 87.5% DOD (**Figure 6e**).[124] Liu *et al*. further developed a semi-liquid electrode using poly(ethylene glycol) as a dual-conductive medium for both ions and electrons combined with Super P. The colloidal dispersion exhibits shear-thinning rheological behavior that effectively releases plating stress and allows stripping/plating to occur throughout the entire electrode volume (2250 mAh cm^{-2} CPC at 5 mA cm^{-2}; 1000 mAh cm^{-2} at 10 mA cm^{-2}).[125]

These studies highlight that auxiliary components in Zn powder anodes should not be optimized solely for adhesion or electronic conductivity. Instead, they can simultaneously preserve ion-electron transfer, volume evolution, and maintain stable contact among Zn particles during repeated high-rate plating/stripping.

5.2.3 Designing electrode architectures

While particle modification and auxiliary-component engineering address local interfacial and interparticle limitations, the overall performance of Zn powder anodes is ultimately governed by the electrode-scale architecture. Conventional slurry-cast Zn powder electrodes depend on discrete contacts between powders, which can lead to poor electronic connectivity and uneven current distribution during repeated plating/stripping. Electrode-level structural design therefore aims to improve particle connectivity and establish continuous ion-electron transport pathways. Wang *et al*. utilized powder metallurgy to fuse discrete particles into a three-dimensional continuous carbon network. Specifically, glucose-derived carbon layers on Zn powder surfaces were interconnected through spark plasma sintering to form a built-in conductive scaffold that redistributes electric fields and provides zincophilic nucleation sites throughout the electrode bulk (> 880 h; 32 mV voltage hysteresis).[126] Du *et al*. hybridized commercial Zn powders with pristine graphene, where the self-assembled 3D graphene network simultaneously enhances interparticle adhesion and acts as an electric field redistributor (89 mV voltage hysteresis versus 349 mV for Zn foil; > 360 h at 5 mA cm^{-2}).[127]

The electrode-current collector interface also critically determines the rate capability of powder-based anodes. Xiao *et al*. proposed an artificial protrusion strategy (APS) using zincophilic tin as the current collector, mechanically embedding Zn powders to create protrusions that exploit Sn's low Zn nucleation overpotential and favorable hardness to guide horizontal Zn^{2+} diffusion rather than vertical dendritic propagation (**Figure 6f**).[128] Optical microscopy confirms that this smooth deposition effectively suppresses hydrogen evolution, with negligible bubble

formation (**Figure 6g**). Tafel analysis confirms the APS anode significantly reduces corrosion current density (0.77 vs. 3.85 mA cm^{-2} for bare Zn; **Figure 6h**). Consequently, this design enables exceptional kinetics, sustaining a limiting current density of 40 mA cm^{-2} (**Figure 6i**).

Three-dimensional printing enables precise spatial control over Zn distribution and electrolyte accessibility, creating geometrically optimized architectures specifically suited for fast-charging applications. Yang *et al*. constructed 3D-printed Zn scaffolds coated with a conformal ion-conductive hydrogel layer (3D Zn@ZAP); the 3D framework provides structural integrity and enlarged electrochemical surface area while the hydrogel coating promotes rapid Zn^{2+} transport along polymer chains (> 120 h at 30 mA cm^{-2} and 30 mAh cm^{-2}).[129] Cao *et al*. functionalized 3D-printed Zn powders with a zinc methacrylate layer containing nucleophilic carbonyl groups that assist desolvation and homogenize ionic flux, achieving 1153 h at 20 mA cm^{-2} and 20 mAh cm^{-2} and remaining stable for 222 h at 30 mA cm^{-2}.[130]

Overall, powder-based architectures, especially 3D-printed Zn anodes, are advantageous for extreme-rate and high-areal-capacity operation because their enlarged active area reduces the local current density, but this benefit is accompanied by higher interfacial reactivity, structural instability, and fabrication complexity. However, their complex fabrication may limit large-scale manufacturing. In contrast, Zn foils sacrifice part of this kinetic advantage for better structural continuity, processability, and mechanical robustness. Future designs should therefore integrate the high-rate kinetics of porous/powder architectures with the practical stability of foil-based electrodes.

6. Synergizing wide ESW and low polarization

At the macroscale, fast-charging failure occurs when accumulated polarization exhausts the electrolyte stability margin due to sluggish ion transport. Thus, XFC-oriented electrolyte design should balance ESW expansion with low transport resistance. Section 6 compares solid-state electrolytes (SSE), quasi-solid-state electrolytes (QSE), and advanced liquid electrolytes, with representative strategies and performance metrics summarized in **Table 4.**

6.1 Solid-state electrolytes

SSEs eliminate free water, thereby extending the ESW and suppressing HER-induced corrosion. However, the non-compact contact within the solid phase/the other solid phase interface and sluggish ion transport in the SSE often lead to high interfacial resistance, requiring tailored structural designs across polymer, inorganic, MOF, and composite materials.

6.1.1 Polymer-based solid electrolytes.

Solid polymer electrolytes (SPEs) rely on segmental chain motion for ion transport, yet the high charge density of Zn^{2+} promotes strong cross-linking with polar functional groups, yielding low ionic conductivity and transference numbers. To decouple Zn^{2+} from anionic traps, Sun *et al*. developed a bilayer poly(ethylene oxide) (PEO) electrolyte loaded with CALF-20 (a porous metal-organic framework) that preferentially binds CF_3SO_3 anions through electrostatic interactions.[131] This anion trapping weakens Zn^{2+}-anion pairing and raises the Zn^{2+} transference number from 0.46 to 0.82, while the composite achieves an ionic conductivity of 10^{-2} S cm^{-1} at room temperature. Paired with a MnO_2 cathode, the full cell delivers 140 mAh g^{-1} with 93% capacity retention over 1000 cycles.

Recently, Hou *et al*. embedded piezoelectric and ferroelectric $CaBi_2Nb_2O_9$ nanosheets within a poly (vinylidene fluoride) (PVDF) matrix.[132] The ferroelectric polarization suppresses ion aggregation at the electrical double layer, reducing the interfacial potential from 22 to 9 mV, while the piezoelectric effect generates a built-in electric field that mitigates dendrite driving forces during Zn deposition. This electrolyte exhibits an ESW of 3.04 V, an ionic conductivity of 1.04 mS cm^{-1}, and a Zn^{2+} Zn^{2+} transference number (tZn^{2+}) of 0.55; Zn//PTO full cells sustain 2500 cycles at 5C with 80% capacity retention. Despite recent progress, organic SSE stability remains unsatisfactory, primarily due to insufficient mechanical strength for suppressing zinc dendrites.

6.1.2 Inorganic-based solid electrolytes

Inorganic solid electrolytes offer high mechanical rigidity and thermal stability, but high activation barriers to Zn^{2+} migration in crystalline lattices impede Zn^{2+} migration. Zhou *et al*. prepared a kaolin-derived solid electrolyte (KL-Zn) *via* zinc-ion exchange of natural mineral kaolin, creating enlarged interlayer spacing that facilitates a desolvation-free Zn^{2+} transport mechanism with an activation energy of only 23.1 kJ mol^{-1}.[133] KL-Zn achieves an ionic conductivity of 5.08 mS cm^{-1}, a tZn^{2+} of 0.79, and an ESW of 2.73 V, with Tafel analysis revealing a low corrosion current

Table 4. Electrolyte strategies for balancing ESW and polarization.

	Electrolyte type	Symmetric cells					Full cell			
		ESW	*J* (mA cm^{-2})	Q_{Area} (mAh cm^{-2})	Time (h)	XFC regime	Type	Current density	Cycle number	Capacity retention (%)
Solid-state electrolyte (SSE)	ZGBC SSE[136]	0-2.66 V	1	1	1000	I	MnO_2	1 C	500	72.7
	HMIC SSE [137]	0-2.88 V	2	2	4500	II	Zn|/ZGBC / NVO	0.1 A g^{-1}	5000	96.1
	CAM-Ag HOF SSE [135]	0-2.6 V	0.5	0.5	1600	I	Zn/PBA	3 C	1000	100
			1	1	1000	I				
	BSSE bilayer SSE [131]		1	1	1400	I	Zn/MnO_2	0.5 A g^{-1}	1000	93
	CBN@PVDF SSE [132]	2.45V	1	1	1500	I	Zn/PTO	5 C	2500	80
	Plastic-crystal SSE [138]	2.8 V	1	0.5	500	I	Zn-MnO_2	200 mA g^{-1}	500	
	Eutectic SSE [139]	2.85 V	8	8	1700	III	Zn-MnHCF	300 mA g^{-1}	1200	90.4
			1	1	2000					
	Mineral-derived SSE [133]	2.73 V	0.2	0.1	2200	I	Zn/$NH_4V_4O_{10}$	1 A g^{-1}	500	93
	Metal halide SSE [134]	3.74 V	0.1	0.1	1100	I	Zn/Ti	0.2 mA cm^{-2}	200	90
Quasi-solid-state electrolyte (QSE)	CN-PAM composite hydrogel [151]	2.48 V	1	1	3000	II	Zn/NVO	10 Ag^{-1}	1000	92.6
			10	2.5	550					
	Hierarchical-heterogeneous biogel [146]	NR	1	1	1000	I	Zn/AC	1 A g^{-1}	10000	97.1
	Bio-inspired multifunctional hydrogel [142]	NR	1	1	2400	I	Zn/MnO_2	10 A g^{-1}	3000	62.7
	Bone-inspired sustainable hydrogel [150]	NR	1	1	3500	II	Zn/NVO	5 Ag^{-1}	2000	82.4
			5	5	2000					
	Polyphosphonitrile derivative-based gel [140]	3.0 V	1	1	10500	I	Zn/VOH	1.5 Ag^{-1}	2000	94.0
	HPG-35 wt % gel [168]	2.7 V	1	1	5500	I	Zn/ZVO	0.7 Ag^{-1}	2300	92
	Biomacromolecular hydrogel [147]	2.31 V	20	5	450	III	Zn/ZVO	0.5Ag-^{1}	400	92.4
	PAM/T[143]	NR	1	1	1200	I	Zn/KVOH	5 Ag^{-1}	2000	87.2
	CarraChi Gel [148]	2.26 V	10	35	4000	III	Zn/ZVO	200 mAg^{-1}	200	84
	Biocompatible gel [145]	1.90 V	1	1	5500	I	Zn/$LiMn_2O_4$	1C	1000	82
	Crowded zwitterionic hydrogel [141]	2.1-2.6 V	1	1	1200	I	Zn/PANI	3 Ag^{-1}	1000	85
	CPAM-based hydrogels [149]	2.92 V	1	0.5	7000	I	Zn/$Zn_{0.25}V_2O_5$	40 Ag^{-1}	2000	80
	Gradient hydrogel [144]	2.6V	1	1	2500	I	Zn/V_2O_5	2 Ag^{-1}	500	91
Novel liquid electrolyte	Deep eutectic co-solvent (DES)[153]	2.4 V	10	10	1000	III	Zn/VS2	0.5 Ag-1	500	85.4
	Zn(OTF)$_2$-Diethylene glycol (DEG)[169]	2.7 V	2	1	900	I	Zn/PANI	8 Ag^{-1}	1700	85
	Ternary eutectic [154]	2.7 V	4	2	140	II	Zn/PANI	5 A g^{-1}	5000	88.5
			0.5	0.1	3000					
	Microemulsion [39]	3.52 V	1	0.5	4800	I	Zn/NaV_3O_8	1 A g^{-1}	1000	78.5
	Lysine pentapeptide [157]	NR	2	2	10000	II	Zn/Polypyrrole/MnO_2	2 A g^{-1}	4000	78.1
	Silk fibroin additive [170]	NR	2	2	200	II	Zn/V_2O_5 ·nH_2O	1 A g^{-1}	1000	95
	Stevia (ST)[165]	NR	5	5	2300	II	Zn/VO_2	2 A g^{-1}	1000	100
	Cellulose succinate ester (CSAE)[166]	2.3 V	1	1	3666	I	Zn/MnO_2	5 A g^{-1}	4000	79.75
	$Emim^+$-TFA^-/OTf^--Zn^{2+}-H_2O [161]	NR	1	1	2500	I	Zn/VO_2@VO	10 Ag^{-1}	3000	75
	Separated [162]	NR	0.2	0.2	2500	I	Zn/V_2O_5	2 A g^{-1}	3000	52
	Self-adaptive [163]	NR	1	1	1350	I	Zn/V_2O_5	2C	553	80
	$ZnSO_4$ and Zn $(ClO_4)_2$[171]	NR	0.5	0.5	3600	I	Zn/NaV_3O_8	2 C	900	93
	MTE [164]	2.53V	2	2	1100	II	Zn/NVO	0.2C	300	71
	Amphiphile confined water [152]	2.73V	10	10	2100	III	Zn/KFeMnHCF	5 A g^{-1}	15000	78.4
	ZSA [155]	NR	2	0.5	1400	I	Zn/PDAN	1 A g^{-1}	7500	71.6

Note:

(1) Zinc ion solid-state electrolyte (ZGBC SSE); hydrated metal-organic ionic cocrystal solid-state electrolyte (HMIC SSE); cyanuric acid-melamine-silver hydrogen-bonded organic framework solid-state electrolyte (CAM-Ag HOF SSE); bilayer solid-state electrolyte (BSSE bilayer SSE); CaBi2Nb2O9/poly(vinylidene difluoride) solid polymer electrolyte (CBN@PVDF SSE); plastic-crystal solid-state electrolyte (plastic-crystal SSE); eutectic solid-state electrolyte (eutectic SSE); mineral-derived solid-state electrolyte (mineral-derived SSE); zinc-based metal halide solid-state electrolyte (metal halide SSE); graphitized carbon nitride/polyacrylamide composite hydrogel (CN-PAM composite hydrogel); gelatin/alginate hierarchical-heterogeneous biogel electrolyte (hierarchical-heterogeneous biogel); bio-inspired multifunctional hydrogel network (bio-inspired multifunctional hydrogel); bone-inspired Zn-doped hydroxyapatite/gelatin hydrogel electrolyte (bone-inspired sustainable hydrogel); polyphosphonitrile derivative-based gel electrolyte (polyphosphonitrile derivative-based gel); poly(ethylene glycol) methyl ether methacrylate/N-hydroxyethyl acrylamide hydrogel with 35 wt% water (HPG-35 wt% gel); electrogelated recyclable biomacromolecular hydrogel electrolyte (biomacromolecular hydrogel); polyacrylamide/trehalose hydrogel (PAM/T); kappa-carrageenan/chitosan gel (CarraChi Gel); hyaluronic acid-based biocompatible hydrogel electrolyte (biocompatible gel); crowded zwitterionic hydrogel electrolyte (crowded zwitterionic hydrogel); single-walled carbon nanotube-embedded polyacrylamide hydrogel (CPAM-based hydrogels); gradient hydrogel electrolyte (gradient hydrogel); acetamide-caprolactam deep eutectic co-solvent (DES); zinc trifluoromethanesulfonate ($Zn(OTf)_2$)-diethylene glycol electrolyte ($Zn(OTF)_2$-diethylene glycol (DEG)); dual-metal-salt-derived ternary eutectic electrolyte (ternary eutectic); microemulsion electrolyte (microemulsion); tailored lysine pentapeptide (LP); silk fibroin additive (SF); stevia (ST); cellulose succinate ester (CSAE); 1-ethyl-3-methylimidazolium trifluoroacetate/zinc trifluoromethanesulfonate-water electrolyte (Emim+-TFA-/OTf--Zn^{2+}-H_2O); self-phase-separated electrolyte (SPSE); self-adaptive electrolyte (self-adaptive); decoupled dual-salt electrolyte based on zinc sulfate and zinc perchlorate (ZnSO4 and $Zn(ClO_4)_2$); multi-tentacle electrolyte (MTE); amphiphile-confined water electrolyte (ACW); 5-sulfosalicylic acid group-coordinated zinc salt (ZSA).

(2) XFC regime is classified using current-density/areal-capacity framework; for strategies reported under multiple symmetric-cell conditions, the highest reached regime is used:

Regime I, fundamental evaluation ($j<5$ mA cm^{-2} and $Q_{areal} \leq 1$ mAh cm^{-2});

Regime II, moderate fast charging ($j \leq 10$ mA cm^{-2} and $Q_{areal} \leq 5$ mAh cm^{-2});

Regime III, single-factor XFC-relevant stress ($j>10$ mA cm^{-2} or $Q_{areal}>5$ mAh cm^{-2} or DODZn≥10%);

Regime IV, coupled high-current/high-areal-capacity XFC-relevant condition ($j>20$ mA cm^{-2} and $Q_{areal}>5$ mAh cm^{-2}).

density of 0.03 mA cm^{-2}. On a different front, Hu *et al*. proposed a composition engineering strategy for hybrid metal halide electrolytes, synthesizing $C_4N_2H_{12}ZnBr_4$ ($PipZnBr_4$) where organic piperazine cations replace inorganic A-site cations to construct Zn^{2+} migration channels between $[ZnBr_4]^{2-}$ units and organic cations.[134] $PipZnBr_4$ delivers an ionic conductivity of 2.9×10^{-4} S cm^{-1} at 25 ℃, a tZn^{2+} of 0.61, and an ESW of 3.74 V; the assembled Zn//I_2 full cell delivers 234.5 mAh g^{-1} after 200 cycles.

6.1.3 MOF-based solid electrolytes

Metal-organic frameworks (MOFs) and hydrogen-bonded organic frameworks (HOFs) offer tunable pore structures and abundant surface sites, yet conventional crystalline frameworks often lack continuous conduction pathways. Li et al. transformed cyanuric acid-melamine into a hydrogen-bonded organic framework solid electrolyte (CAM-Ag) by incorporating Ag-N coordinate bonds.[135] This crystal transformation shortens the hopping distance between Zn^{2+} sites from long-range to adjacent-site hopping, reducing the migration energy barrier from 0.33 to 0.26 eV. CAM-Ag exhibits an ionic conductivity of 1.14×10^{-4} S cm^{-1}, a tZn^{2+} of 0.72, an ESW of 2.66 V, and a corrosion current density of 0.028 mA cm^{-2}; the Zn//MnO_2 full cell delivers 315 mAh g^{-1} with 72.7% capacity retention over 500 cycles. Departing from conventional divalent Zn^{2+} carriers, Xu *et al*. designed an amorphous MOF (ZGB-MOF) enriched with O-Ga-Cl polyanion clusters.[136] The polyanion environment of Ga^{3+} promotes the formation of monovalent $ZnCl^+$ carrier groups, slashing the ion transport energy barrier to 0.12 eV and yielding an ionic conductivity of 5.2×10^{-3} S cm^{-1} with the tZn^{2+} of 0.873. The electrolyte displays an ESW of 2.88 V, and the Zn//ZnHCF full cell shows robust rate capability up to 4 A g^{-1}.

6.1.4 Other composite-based solid electrolytes

Composite strategies that integrate multiple transport mechanisms offer a promising route to break the conductivity-stability trade-off. Hong *et al*. developed a hydrated metal-organic ionic cocrystal (HMIC, Zn-4IMI1-3) featuring a solvent-assisted hopping mechanism along grain boundaries (**Figure 7a**).[137]

Crystal engineering strengthens host-guest interactions with anions and hydrogen bonding with surface water molecules, achieving a Zn^{2+} conductivity of 8.6 mS cm^{-1} and the tZn^{2+} of 0.81 with an ESW of 2.6 V (**Figure 7b**). The strong water binding lowers the desolvation activation energy to 29.1 kJ mol^{-1}, enabling Zn//PBA batteries to charge at 180 C (20 s) for over 1000 cycles (**Figure 7c**) with 100% capacity retention from -30 to 30 ℃.

Zhao *et al*. developed a plastic-crystal electrolyte (ZPE) using the amphiphilic surfactant AOT. In this system, AOT molecules self-assemble into layered nanochannels, where their ionic headgroups maintain directional alignment while moving freely within the structure.[138] Within these nanochannels, heteroleptic coordination by water molecules frees Zn^{2+} from anionic traps, yielding a conductivity of 2.2 × 10^{-3} S cm^{-1}, a tZn^{2+} of 0.73, an oxidation stability exceeding 2.8 V, and a Zn-Cu CE of 99.6%.

Ling *et al*. developed a non-flammable polymer solid-state eutectic electrolyte (PSNE) *via* in situ polymerization of a ternary eutectic within an ETPTA framework.[139] Strong Zn^{2+}-NMA coordination induces a high desolvation barrier, thermodynamically elevating the discharge voltage, while the cross-linked ETPTA matrix anchors solvent molecules to facilitate rapid ion conduction. Consequently, the PSNE achieves a high ionic conductivity (3.94 ×10^{-3} S cm^{-1}), at Zn^{2+} of 0.60, and a 2.85 V stability window. Remarkably, it enables stable symmetric cell cycling for 1700 h at 8.0 mA cm^{-2} under a stringent 80% Zn utilization, yielding practical pouch cells with an energy density of 50 Wh kg^{-1}.

For XFC, the advantage of SSE lies in strong water suppression and a wide ESW, whereas sluggish Zn^{2+} transport may generate additional polarization. Therefore, the key is not to maximize ESW alone, but to balance stability margin with transport resistance.

6.2 Quasi-solid electrolytes

Quasi-solid hydrogel electrolytes retain aqueous-level ionic conductivity while confining water within polymer networks to suppress HER and extend the ESW. However, the hydrophilic gel backbone inherently impedes Zn^{2+} transport, and the trade-off between ionic conductivity and mechanical robustness remains a fundamental challenge for fast-charging operation.[140] Strategies to address these issues are systematically categorized by material platform: biopolymer-based, synthetic polymer-based, and nanomaterial-reinforced composite hydrogels.

6.2.1 Synthetic polymer-based hydrogels

Synthetic polymer networks enable precise control over pore architecture, crosslinking density, and functional groups to balance ion transport with mechanical stability under high current densities. Wang *et al*. synthesized a crowded zwitterionic hydrogel electrolyte *via* free-radical polymerization of sulfobetaine methacrylate (SBMA).[141] The inner-salt structure of the polySBMA matrix promotes Zn^{2+} dissociation and transport along polymer chains. Maltose simultaneously bridges polymer chains *via* hydrogen bonding while crowding salt species, thereby inducing anion-polymer interactions and further reducing contact ion pairs and solvation water. The resulting electrolyte achieves an ionic conductivity comparable to its liquid equivalent, an ESW of 2.6 V, and stable Zn utilization up to 57% DOD at high rates (5 A g^{-1}) down to -60 ℃.

Synthetic polymer frameworks also allow the incorporation of functional additives for targeted property modulation. Trehalose, a naturally abundant disaccharide, forms robust hydrogen bonds with PAM chains, filling network imperfections and enhancing mechanical strength and water retention. Yang *et al*. reported a PAM/trehalose gel achieving 100 kPa strength and 5338% stretchability with strong interfacial adhesion; the flexible Zn//MnO_2 pouch cell cycles for 2400 h with 98.8% CE.[142]

Wang *et al*. extended this platform by exploiting trehalose cryoprotective properties to enable wide-temperature operation from -15 to 50 ℃, achieving 87.2% capacity retention after 2000 cycles at 5 A g^{-1}.[143] Pushing the environmental boundary further, Han *et al*. designed a polyphosphonitrile derivative gel incorporating low-melting-point methanol co-solvents and in situ gelation using a fireproof phosphonitrile monomer; the resulting electrolyte achieves a 99.75% Coulombic efficiency over 6500 cycles and an ultra-wide operating window from -70 to 80 ℃.[140]

Beyond homogeneous networks, structural gradients can be engineered to decouple the conductivity-mechanics trade-off. Zhou *et al*. leveraged the Hofmeister effect to design a concentration-gradient hydrogel electrolyte (CGHE) comprising polyvinyl alcohol and hydroxyethyl cellulose with spatially varying acetate concentrations.[144] The high-acetate layer facing the Zn anode suppresses water activity and HER, while the low-acetate bulk maintains ionic transport. This gradient architecture achieves a high Zn^{2+} transference number of 0.88 and a mechanical strength of 1.7 MPa, guiding uniform Zn (002) deposition while suppressing HER through localized reduction in water activity (2500 h; 99.1% CE).

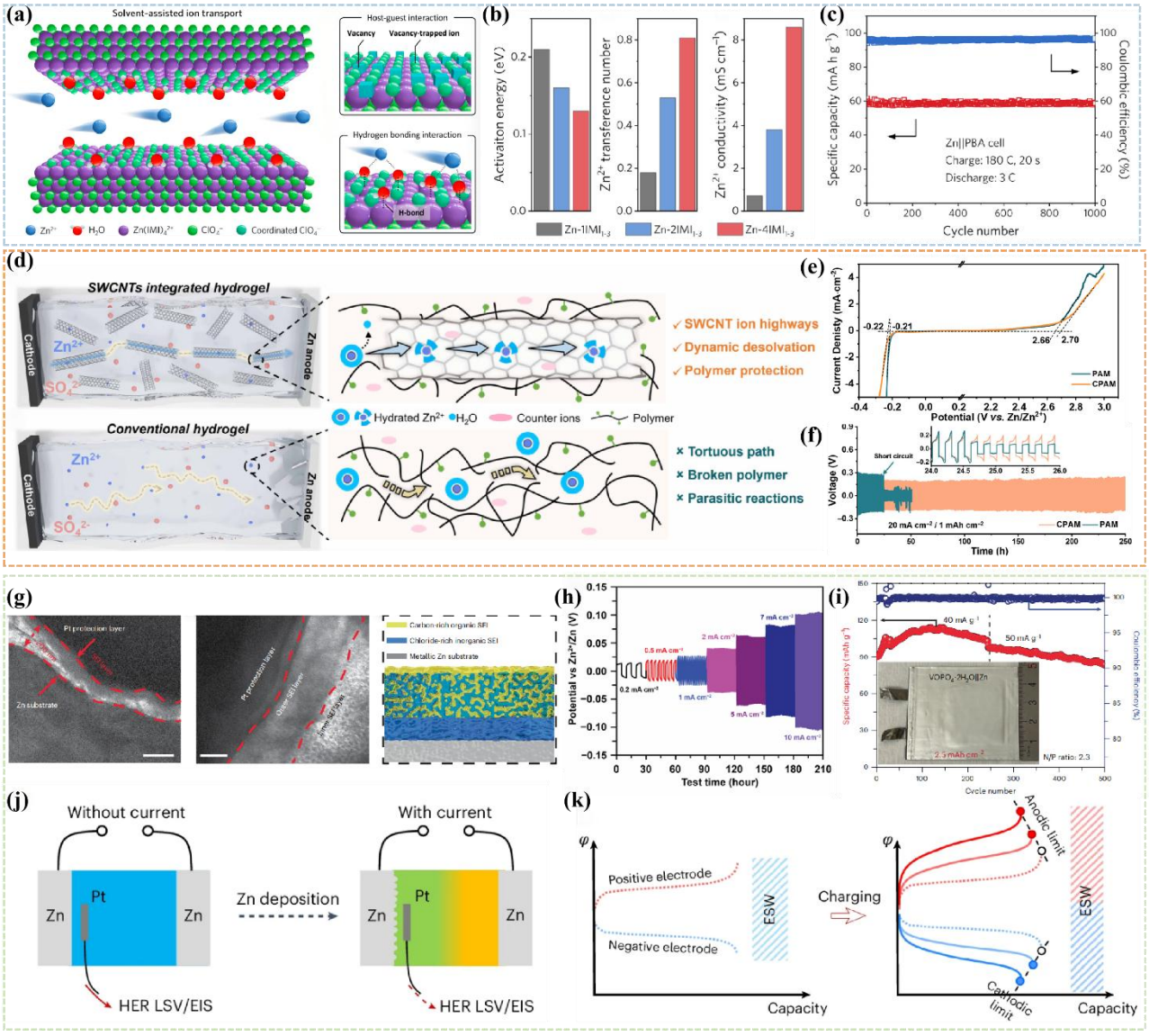


Figure 7. (a) Schematic diagram of the solvent-assisted ionic transport mechanism in HMIC-based electrolytes. (b) Comparison of Ea, tZn^{2+}, and Zn^{2+} conductivities of Zn-1IMI1-3, Zn-2IMI1-3, and Zn-4IMI1-3. (c) Long-term cycling performance of Zn/PBA cell with Zn-4IMI1-3 at 20 s charge time.[137] Copyright 2025, National Academy of Sciences. (d) Schematic illustration of fast ion transport through SWCNT channels in cPAM and tortuous ion transport in conventional PAM. (e) ESW of PAM and CPAM. (f) Long-term cycling performance of symmetric Zn/Gel/Zn cells under 20 mA cm^{-2}.[149] Copyright 2025, The Authors. Published by AAAS. (g) The cross-sectional TEM image, high-resolution TEM image and presentation of the dual-layer SEI. (h) Rate performance of symmetric batteries. (i) Pouch cell cycling with $VOPO_4$ $2H_2O$ mass loading of 22.5 mg cm^{-2}.[156] Copyright 2023, Springer Nature. (j) Electrochemical set-up used to assess the effect of charge-induced phase separation on HER suppression. (k) Working principle of the self-adaptive electrolyte during fast charging.[163] Copyright 2025, Springer Nature.

6.2.2 Biopolymer-based hydrogels

In contrast to petroleum-derived synthetic polymers, whose monomers and crosslinkers often contain toxic chemicals, raising biosecurity concerns, natural polysaccharides and proteins offer inherently sustainable, biodegradable alternatives with abundant hydrophilic functional groups that anchor free water and suppress corrosion. Li *et al.* developed a hyaluronic acid hydrogel electrolyte leveraging its ample -OH and -COOH groups; the -COOH groups coordinate with Zn^{2+} to modulate the solvation sheath

and regulate nucleation thermodynamics, while the -OH groups form hydrogen bonds with free water molecules to reduce interfacial water activity and inhibit HER.[145] The electrolyte achieves a CE of 99.71% and sustains Zn plating/stripping for 250 h at 80% DOD, while the Zn//$LiMn_2O_4$ pouch cell retains 82% capacity after 1000 cycles at 3C.

Wang *et al*. alternatively constructed a hierarchical-heterogeneous biogel electrolyte (GTA) from gelatin, tannic acid, and alginate [146], where in situ crystallized gelatin triple helices within alginate domains provide temperature-triggered adhesion and high toughness. Moreover, the GTA exhibits a high Zn^{2+} transference number and temperature-independent ionic conductivity, enabling rate cycling with a smaller overpotential from 1 to 20 mA cm^{-2}.

On the practical front, Huang *et al*. employed electrogelation to fabricate thin-film biomacromolecular hydrogel electrolytes (as thin as 50 μm) with simultaneously high mechanical strength (2.0-4.4 MPa) and ionic conductivity (10.1-19.5 mS cm^{-1}).[147] The electrolyte achieves 99.83% CE over 2800 cycles and supports practical Zn-metal batteries with an aerial capacity of 5.4 mAh cm^{-2} at N/P = 1.1, highlighting the potential of sustainable biopolymer platforms for energy-dense applications. For large-format applications, Wang *et al*. formulated a carrageenan/chitosan gel electrolyte in which sulfate groups on κ-carrageenan chains crosslink with amino groups on chitosan to form a robust hydrogen-bonded network that immobilizes water molecules. This design enables an open-pouch cell configuration that releases hydrogen gas and permits electrolyte replenishment, delivering 0.9 Ah with 84% capacity retention after 200 cycles and validating the practical scalability of biopolymer gel systems.[148]

6.2.3 Nanomaterial-reinforced composite hydrogels

Integrating functional nanomaterials into polymer matrices introduces additional ion-transport pathways and selective interfaces that transcend the limitations of pristine polymer networks, offering the most direct route to high-rate capability. Lin *et al*. embedded aligned single-walled carbon nanotubes (SWCNTs) within PAM hydrogels through photo-initiated in situ polymerization to create nanofluidic ion highways; the hydrophobic SWCNT channels induce partial desolvation of $[Zn(H_2O)_6]^{2+}$ during passage (**Figure 7d**), expanding the ESW from 2.87 to 2.92 V (**Figure 7e**) while reducing the Zn^{2+} migration activation energy by 43% and doubling the ionic conductivity to 30.3 mS cm^{-1}.[149] The SWCNT/PAM gel maintains structural integrity at 50 mA cm^{-2} and enables Zn//Zn cells to operate stably for 250 h at 20 mA cm^{-2} (**Figure 7f**). Similarly, Peng *et al*. incorporated Zn-doped hydroxyapatite (Zn-HA) nanofibers into a gelatin matrix to establish dual Zn^{2+} transport channels.[150] The phosphate groups within the HA crystal lattice create low-energy-barrier Zn^{2+} transport pathways *via* site-to-site hopping, while surface hydroxyl groups anchor free water to suppress side reactions. The Zn-HA superionic conductor delivers an ultrahigh ionic conductivity of 32.5 mS cm^{-1} with a Zn^{2+} transference number of 0.80, achieving a CPC of 5 Ah cm^{-2} at 5 mA cm^{-2}/5 mAh cm^{-2} with 82.4% full-cell capacity retention after 2000 cycles. Liu *et al*. introduced alkali-etched graphitic carbon nitride (g-C_3N_4) nanosheets as multifunctional crosslinkers and structural templates within PAM networks; the OH-rich g-C_3N_4 induces polymerization through multi-point hydrogen bonding, constructing a homogeneously porous composite hydrogel with an ionic conductivity of 22.21 mS cm^{-1} and a Zn^{2+} transference number of 0.80.[151] The CN-PAM gel achieves stable cycling for 550 h at 10 mA cm^{-2}/2.5 mAh cm^{-2}, and the Zn//NVO full cell maintains 92.6% capacity retention after 1000 cycles at 10 A g^{-1}.

Notably, although QSEs significantly improve cycling stability compared to SSEs, their tolerance to high currents remains insufficient, as excessive crosslinking has a strong coordination effect with Zn^{2+} and increases transport resistance. Their XFC performance therefore depends on balancing stability with rapid ion conduction.

6.3 Novel liquid electrolytes

While solid and quasi-solid electrolytes suppress water activity through physical confinement, novel liquid systems retain rapid aqueous ion transport through increasingly multifunctional electrolyte designs. Recent advances span nanoscale water confinement, deep-eutectic and microemulsion systems, peptide-based electrolytes, and dynamically phase-separated or self-adaptive concepts. Zheng *et al*. constructed an amphiphile-confined water electrolyte in which n-alkanols with hydrophilic hydroxyl heads and hydrophobic tails reorganize the aqueous phase into nanometric water channels approximately 1.8 nm in size.[152] This decouples cation transport from the inert amphiphile matrix, yielding a Zn^{2+} transference number of 0.79 and enabling a Zn//KFeMnHCF full cell to retain 78.4% capacity over 15000 cycles while delivering 68.4 mAh g^{-1} even at -60 ℃.

A promising route to broaden the ESW while preserving liquid-state kinetics is to introduce

molecular co-solvents that restructure the bulk hydrogen-bond network and displace water from the Zn^{2+} coordination sphere. Wang *et al*. formulated a deep eutectic electrolyte from acetamide (donor) and caprolactam (acceptor). [153] The donor-acceptor pair reorients bulk hydrogen bonds away from water, lowering the HER onset potential by over 200 mV. The electrolyte achieves a CE of 98.37% and sustains symmetric cell cycling for 1000 h at 10 mA cm^{-2} and 10 mAh cm^{-2}. Li *et al*. extended this co-solvent concept by introducing lithium bis(trifluoromethanesulfonyl) imide as a supporting salt into a $Zn(OTf)_2$-N-methylacetamide matrix.[154] The supporting salt with weak lattice energy not only induces the reconstruction of intermolecular interactions to form ion pairs and ion aggregates but also tailors the Zn^{2+} solvation structure and SEI. Departing from neutral co-solvents, Wang *et al*. developed an organometallic chelated electrolyte by reacting zinc oxide with 5-sulfosalicylic acid (SA). The resulting $Zn(SA)(H_2O)_4$ complex uses SA as an organic coordinating co-solvent that displaces water from the inner solvation shell.[155] The highest occupied molecular orbital and lowest unoccupied molecular orbital (LUMO-HOMO) gap of Zn-SA is lower than that of Zn-water. At the same time, LUMO (which accepts electrons for reduction) is localized on the SA^{2-} ligand, lowering the coordinated water activity and widening the cathodic stability limit. Ji *et al*. further combined the co-solvent strategy with a high-concentration overall design, resulting in a concentrated chloride hybrid electrolyte with dimethyl carbonate.[156] The concentrated Cl^- coordinates Zn^{2+} to displace water from the solvation shell, while DMC lowers bulk Hammett acidity. Notably, DMC does not merely act as an inert solvent; it decomposes in situ to participate in SEI formation, yielding a dual-layered structure with an organic-rich outer layer and an inorganic $ZnS/ZnCO_3$ inner layer (**Figure 7g**). This co-solvent-mediated high-concentration architecture can endure the current density of 10 mA cm^{-2} (**Figure 7h**) and enables a practical pouch cell to deliver 100 Wh kg^{-1} over 500 deep cycles (**Figure 7i**).

Manipulating the configurational entropy of the electrolyte provides an alternative strategy for spatially confining water activity. Xia *et al*. introduced an oil-in-water microemulsion system that spontaneously forms an oil-rich layer at the electrode interface, expanding the ESW to 3.52 V.[39] Liu *et al*. constructed a thermodynamically stable colloid dispersion electrolyte from tailored lysine pentapeptides.[157] The peptide attracts water molecules to achieve Zn^{2+} desolvation while guiding (002)-plane deposition, enabling ultralong symmetric cell cycling exceeding 10, 000 h.

Targeted interfacial engineering provides localized stabilization that directly suppresses HER and lowers polarization under high-rate operation. Wang *et al*. demonstrated a localized hydrogen-bond docking strategy using polyhydroxy hexitol.[158] Each hexitol molecule bears six pairs of hydrogen-bond donors and acceptors that preferentially adsorb onto the Zn surface in a parallel configuration, reconstructing interfacial hydrogen-bond networks. This targeted interfacial modification increases the proportion of weak hydrogen bonds among water molecules from 12.36% to 15.51%, suppressing proton transport *via* the Grotthuss mechanism, while the lower-lying LUMO of hexitol diverts electron density away from coordinated water. Consequently, the electrolyte achieves a Coulombic efficiency of 99.8% and extends symmetric cell lifespan beyond 5000 h. Transitioning from hydrogen-bond regulation to concentration-field engineering, localized high-concentration electrolytes achieve interfacial anion enrichment without the viscosity penalty of bulk high-concentration systems. Yang *et al*. introduced ammonium phosphotungstate (APT) as a trace diluent-like additive; the oversized $[PW_{13}O_{40}]^{3-}$ polyoxoanion remains outside the Zn^{2+} primary solvation shell but electrostatically repels OTf^- into the solvation sheath, increasing contact ion pairs and creating a local anion-rich environment that promotes Zn^{2+} desolvation and induces a uniform anion-derived SEI.[159] Similarly, Huang *et al*. constructed a self-assembled localized high-concentration environment using zwitterionic co-solute C10, where amphiphilic molecules spontaneously form ~3.8 nm quasi-spherical aggregates that enrich Zn^{2+}/OTf^- at the interface *via* zwitterionic effects while establishing bilayer ion-conducting channels within the electric double layer.[160] Hence, the C10 system delivers 1200 h at 5 mA cm^{-2} with 42.7% depth of discharge. Yang *et al.* leveraged gradient chaotropic regulation by designing an ionic-liquid-based aqueous electrolyte in which chaotropic anions spontaneously enrich at the Zn anode interface to form a hydrophobic yet salt-philic gradient layer.[161] This interfacial gradient simultaneously enables dendrite-free zinc deposition and antifreeze operation, with full cells maintaining nearly 100% capacity retention over 3500 cycles at -40 ℃.

The electrolyte that dynamically adapts its composition in response to charging conditions is also an effective strategy. Conventional attempts at such decoupling rely on membranes or metastable layering, which suffer from trans-phase diffusion during stirring or rollover, compromising long-term stability. Zhao *et al.* addressed this by developing a self-phase separated

electrolyte (SPSE) grounded in thermodynamic screening of Hildebrand solubility parameters and dielectric constants.[162] N, N-dimethyltrifluoroacetamide (FDMA) was identified as the hydrophobic nonaqueous solvent; its moderate dielectric constant and large Hildebrand parameter disparity relative to water drive spontaneous demixing into an aqueous phase (A phase, $ZnSO_4$-based) and a nonaqueous phase (N phase, FDMA-rich). Crucially, the phase boundary remains thermodynamically stable against stirring and aging, unlike prior metastable decoupling systems. Molecular dynamics simulations and SANS confirm the spontaneous emergence of a sharp interface. Consequently, the corrosion current density drops to 0.08 mA cm^{-2}. Zhao *et al*. developed a self-adaptive electrolyte formulated at the cloud point of a ternary salt-solvent system.[163] During charging, solvent separation dynamically redistributes oxidation-resistant components toward the cathode and reduction-resistant components toward the anode (**Figure 7j**), broadening the ESW in real time as overpotential rises (**Figure 7k**). Decoupled electrolyte architectures extend this logic further by independently tailoring the anolyte and catholyte to maximize their respective stability windows, though practical integration remains at an early stage.

Finally, bio-inspired and biomass-derived electrolytes offer sustainable pathways to interfacial stabilization. Wang *et al*. designed a multi-tentacle electrolyte in which multi-tentacle salts and organics form extensive hydrogen bonds to confine water movement without increasing viscosity.[164] This enables stable Zn cycling at -40 ℃ with 99.99% capacity retention per cycle over 1000 cycles at a high areal capacity of 3.4 mAh cm^{-2}. Wang et al. further exploited a biomimetic anchor-capture effect using stevia, a natural multidentate additive that simultaneously anchors onto the Zn surface to reconstruct interfacial hydrogen bonding and captures Zn^{2+} to suppress 2D diffusion.[165] Li *et al*. introduced a sustainable biomass electrolyte prepared *via* mechanochemistry from microcrystalline cellulose and succinic anhydride. Carboxyl and hydroxyl groups synergistically shield the Zn anode, enabling the Zn//MnO_2 full cell to retain 79.75% capacity after 4000 cycles at 5 A g^{-1}.[166]

Among the three electrolyte platforms, SSEs largely sacrifice the intrinsic advantages of aqueous electrolytes by removing or strongly restricting water, while their high transport resistance further limits XFC capability. QSEs provide a compromise between water confinement and ion transport, but the resistance of gel networks remains difficult to reconcile with extreme-rate operation, and highly conductive designs often require more complex material architectures. In comparison, liquid electrolytes remain the most practical platform for XFC because they preserve rapid aqueous ion transport while allowing the ESW and interfacial stability to be tuned through solvation and interfacial regulation. Therefore, the key is not to maximize the nominal ESW, but to retain a sufficiently wide usable stability margin without sacrificing fast ion transport.

7. Related equations

(1) Depth of discharge (DOD)

The full-cell DOD is calculated based on the rated capacity:

$$DOD = \frac{\text{actual discharge capacity}}{\text{theoretical capacity}} \times 100\%$$

However, distinct from the full-cell DOD, the formula for the zinc foil anode is defined as follows:

$$DOD = \frac{y}{0.585x} \times 100\%$$

where x is the zinc foil thickness (in μm), y is the zinc areal capacity utilized in the electrochemical testing (mAh cm^{-2}). This formula is based on the theoretical volumetric capacity of zinc (approximately 5855 mAh cm^{-3}), calculating the DOD as the ratio of the actual discharge capacity to the theoretical capacity.

(2) Cumulative plating capacity (CPC)

The cumulative plate capacity before failure (CPC = sum C_{cycle}) should be universally adopted as a core metric for assessing commercial viability.

(3) Electrolyte-to-Capacity Ratio (E/C Ratio)

$$E/C = \frac{V_{electrolyte}}{C_{cell}}$$

Where $V_{electrolyte}$ is the volume of the injected electrolyte (μL), and C_{cell} is the total nominal capacity of the cell (mAh).

(4) System-Level Energy Density (E_{cell})

To ensure that fast-charging capabilities do not come at the severe expense of overall energy density, E_{cell} (Wh kg^{-1}) must be calculated based on the total mass of all active and passive components within the cell packaging, rather than solely relying on the mass of the cathode active material:

$$E_{cell} = \frac{\int_0^t V(t) I dt}{M_{total}}$$

The total cell mass (Mtotal) is strictly defined as:

$$M_{\text{total}} = M_{\text{Cathode}} + M_{\text{Zn_anode}} + M_{\text{electrolyte}} + M_{\text{separator}} + M_{\text{packing}}$$

This comprehensive calculation explicitly accounts for the necessary inclusion of excess zinc (N/P constraints) and the realistic electrolyte inventory.

(5) Negative-to-positive capacity ratio (N/P ratio)

The N/P ratio quantifies the excess of the zinc anode. It is calculated as:

$$N/P = \frac{m_{zn} \times C_{th,\,zn}}{m_{cathode} \times C_{pr,\,cathode}}$$

Where: m_{Zn} and $m_{cathode}$ are the areal mass loadings of the zinc anode and cathode active material (mg cm^{-2}), respectively.

$C_{th,\,Zn}$ is the theoretical specific capacity of zinc (820 mAh g^{-1}).

$C_{pr,\,cathode}$ is the practical specific capacity delivered by the cathode (mAh g^{-1}).

8. Outlook

The development of fast-charging AZIBs is entering a stage where isolated material modifications are no longer sufficient. Future progress requires scale-resolved design rules that directly target the polarization cascade identified in this Review: suppressing polarization generation at the molecular/interface level, limiting polarization amplification at the electrode level, and delaying polarization-induced failure at the full-cell level. Based on this framework, the following directions are particularly important for transforming laboratory-scale fast-charging zinc anodes into practical batteries.

8.1 From empirical modification to scale-resolved design rules

At the microscale, the priority is to suppress the initial generation of polarization by clarifying and regulating the RDS of Zn^{2+} desolvation. Zinc-ion desolvation is a multi-step process. However, most current studies rely heavily on static theoretical calculations of binding energy or desolvation energy, which cannot fully capture transient interfacial states under high-current conditions relevant to XFC. Drawing inspiration from electrocatalysis on H_2O splitting (e.g., HER and OER), [167] future efforts must identify and manipulate the absolute RDS. This requires moving beyond reaction theoretical calculations by applying advanced in situ characterizations to capture transient reactive intermediates during rapid charge transfer (**Figure 8a**).

At the mesoscale, the key task is to prevent microscopic polarization from being amplified into nonuniform deposition. Zn foils and Zn powders should be viewed as complementary electrode architectures with distinct failure modes. Dense Zn foils provide mechanical continuity and lower corrosion exposure but suffer from high local nucleation polarization, whereas Zn powders reduce local current density through larger active surface area but introduce interparticle heterogeneity, structural expansion, and contact instability. Future electrode design should integrate foil stability with the flux-buffering capability of porous or powder-like architectures, such as hierarchical current collectors, 3D frameworks, and so on (**Figure 8a**).

At the macroscale, the central challenge is to delay polarization-induced failure by preserving a usable aqueous stability margin. Future electrolyte and cell-level design should therefore shift from maximizing the nominal ESW to preserving a usable stability margin under fast-charging polarization. Rather than evaluating electrolyte stability in isolation, future studies should quantify how the stability window evolves during repeated XFC cycling with limited Zn, lean electrolyte, and high cathode loading. The practical target is to maintain a sufficient polarization margin before water decomposition or interfacial failure is triggered under full-cell operation (**Figure 8a**).

Beyond individual scale optimization, artificial intelligence (AI)-assisted cross-scale modeling could accelerate the discovery of practical fast-charging systems. Current theoretical methods are often fragmented: DFT calculations to compute desolvation barriers or COMSOL simulations to model dendrite propagation. However, practical cell failure emerges from the coupling among these scales. Machine learning and predictive models should therefore be used to connect molecular descriptors, interfacial kinetic parameters, electrode architecture, and cell-level degradation. Such models could identify hidden correlations between desolvation energy, nucleation overpotential, local current density, electrolyte resistance, and CPC, enabling predictive design rather than trial-and-error optimization (**Figure 8b**).

8.2 Scale-resolved evaluation protocols bridging Zn-anode testing and practical XFC AZIBs

High-rate Zn-anode performance is often evaluated

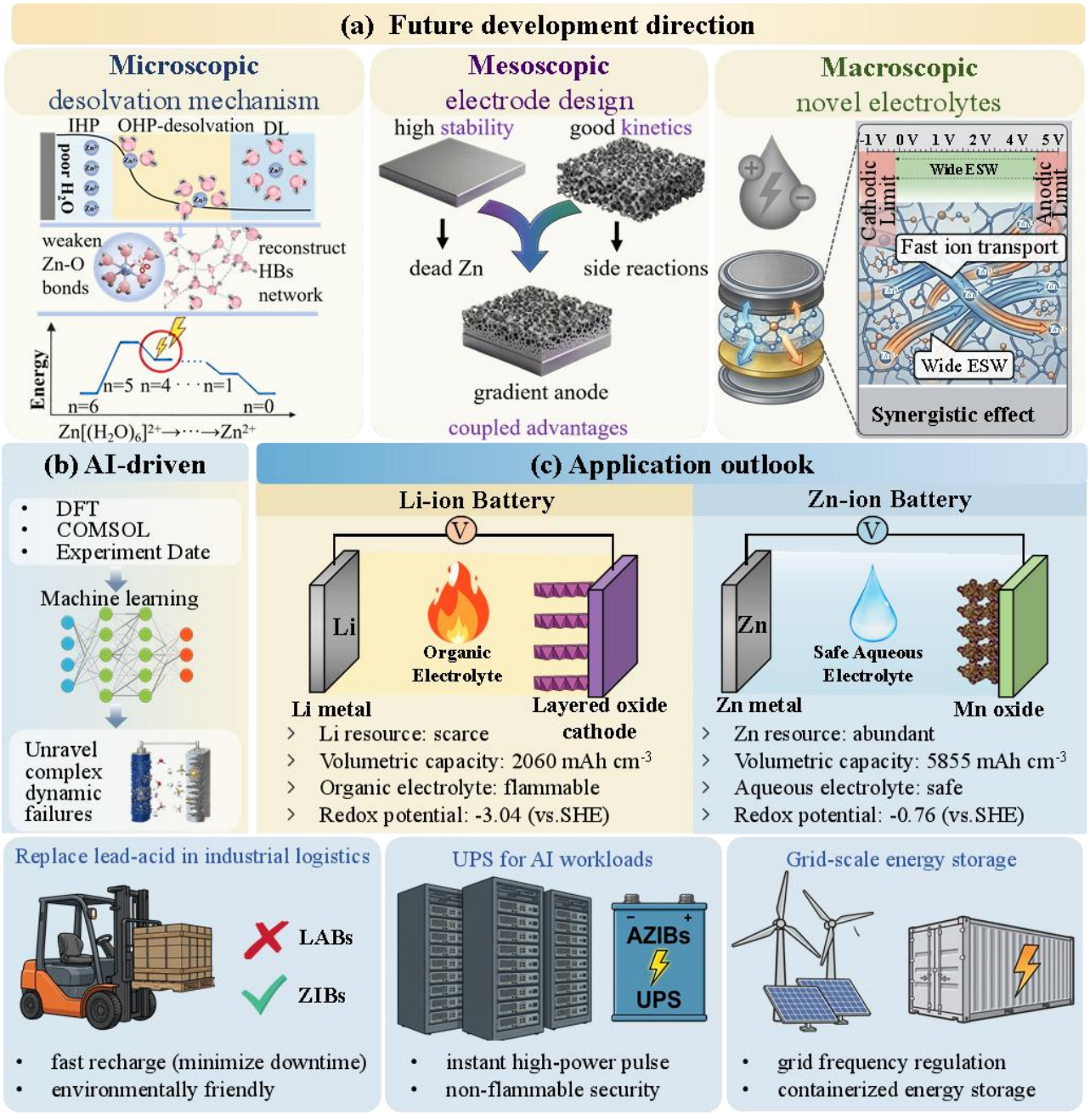


Figure 8. (a) Future development direction across microscopic, mesoscale, and macroscopic scales. (b) AI-driven framework. (c) Application outlook targeting specific scenarios where XFC AZIBs may be applied.

under permissive conditions, such as thick Zn foils, excess electrolyte, and low cathode loading, which may mask polarization-induced degradation and overestimate practical relevance. Therefore, XFC evaluation should bridge anode-level behavior under XFC-relevant conditions with practical full-cell performance.

At the microscale, evaluation should determine whether a strategy suppresses the generation of polarization by accelerating Zn^{2+} transport, desolvation, and interfacial charge transfer while limiting parasitic reactions. Relevant descriptors include desolvation activation energy, Zn^{2+} transference number (t_{Zn2+}), nucleation overpotential, HER tendency, corrosion

current, and interfacial resistance evolution. Based on **Tables 1-5**, ensuring initial kinetic stability under XFC conditions requires a low desolvation activation energy (E_a < 40 kJ mol^{-1}) and a high Zn^{2+} transference number (t_{Zn2+} > 0.6). At the mesoscale, evaluation should determine whether polarization amplification is controlled by local current-density distribution, local pH, deposition morphology and interface EDL. Key descriptors include current density, areal capacity, actual plating/stripping time, deposition morphology, dead-Zn formation, and CPC. Based on **Tables 1~4**, mesoscopic evaluation must reach at least Regime III (J > 10 mA cm^{-2} or Q_{areal} > 5 mAh cm^{-2}). Under these conditions, a XFC Zn anode should deliver a CPC exceeding 1 Ah cm^{-2} to conclusively demonstrate sustained dendrite suppression and interface stability under massive ionic flux.

At the macroscale, evaluation should determine whether these microscopic and mesoscopic advantages can be maintained in practical full cells. Required descriptors include cathode loading, Zn thickness or Zn excess (DOD_{Zn}), N/P ratio, cell-level energy density and pouch-cell validation. To bridge the gap to practical viability (**Tables 1~4**), XFC full cells must operate under strict material constraints: a deep DOD_{Zn} (> 30%), a low N/P ratio (< 3). The detailed mathematical formulations are summarized in **Section 7**.

To avoid conflating high-current Zn-anode testing with true full-cell XFC capability, we propose a two-level evaluation protocol comprising XFC-relevant anode and full-cell XFC performance metrics for pouch cells.

(1) For Zn-anode-level evaluation: Testing must transcend small-area coin cells by utilizing scaled-up electrodes (> 10~20 cm^2) with restricted Zn foil thicknesses (≤ 30-50 μm). Evaluation should rely on aggressive areal testing parameters (j > 10 mA cm^{-2} and Q_{areal} > 5 mAh cm^{-2}), the anode should safely sustain a deep DODZn (> 30%) and push the CPC beyond 20 Ah.

(2) For full-cell level evaluation: Building on the anode baseline, Ah-scale pouch cells must operate under rigorous constraints: high cathode loading, N/P < 3, and E/C < 10 μL mAh^{-1}. Device-level targets must fundamentally stem from the intrinsic thermodynamic limits of specific cathode chemistries. Taking the Zn//MnO_2 system as an example, its practical full-cell energy density is 50~80 Wh kg^{-1}. Mathematically ($P = E/t$), injecting 80% of the targeted energy density within 15 min demands a continuous power output equivalent to P_{target} ≥3.2 × E_{target}. Therefore, for a Zn//MnO_2 pouch cell (80 Wh kg^{-1}), its power density of at least 256 W kg^{-1} can satisfy the XFC requirement.

(3) Beyond standardizing internal evaluation, establishing independent third-party certification platforms is critical for validating the true commercial viability of AZIBs. Exceptional performance metrics, including the ultra-high-rate cycling stability of pouch cells, should be rigorously tested in a blind manner using identical temperatures, hardware fixtures, and cell assembly protocols. This verification process will minimize selective data reporting and propel the transition of fast-charging zinc batteries from fundamental laboratory research to trusted industrial applications.

8.3 Potential application

The ultimate evaluation of any energy storage technology lies in its practical utility. Rather than pursuing universally flawless systems, commercialization efforts must target specific application scenarios. Lithium-ion batteries dominate in energy density but pose severe thermal runaway risks under XFC. Redox flow batteries are intrinsically safe but suffer from low energy density and high structural complexity, necessitating circulating pumps and bulky reservoirs. Furthermore, lead-acid batteries are limited by their toxicity and poor high-rate performance. In contrast, AZIBs strike an exceptional balance between economic viability and safety. This balance is underpinned by their high theoretical volumetric capacity (5855 mAh cm^{-3}), resource abundance, and the use of intrinsically safe aqueous electrolytes. With appropriate strategies, XFC AZIBs may become competitive candidates for safe, low-cost, and high-power energy-storage scenarios (**Figure 8c**):

(1) Industrial logistics and heavy machinery: For high-frequency operations, including forklifts and automated guided vehicles in ports, the fast-charging capability of AZIBs significantly minimizes operational downtime. This characteristic establishes them as a sustainable, high-power alternative to traditional lead-acid batteries.

(2) Data centers and uninterruptible power supply (UPS) for AI computing: The rapid expansion of artificial intelligence computing generates instantaneous power spikes (step-loads) that severely stress data center grids. Functioning as high-rate UPS systems, AZIBs can instantaneously deliver massive power pulses to bridge these gaps and prevent critical

data loss. More importantly, their intrinsic aqueous safety effectively eliminates the fire hazards associated with deploying high-power lithium-ion battery banks in dense computing environments.

(3) Grid-scale storage and frequency regulation: Stabilizing grid frequency requires energy storage systems capable of rapidly absorbing or discharging massive power surges within seconds. The ultrafast kinetic response of AZIBs aligns with these high-frequency power-switching demands. Combined with their low levelized cost and high safety, AZIBs can serve as highly responsive grid buffers, alleviating the complex thermal management burdens inherent to large-scale lithium-based utility storage.

In summary, by integrating AI-assisted computational design with rigorous, standardized evaluation metrics and independent certification, XFC aqueous zinc batteries are poised to unlock their full kinetic potential. By maintaining safety under extreme currents, AZIBs may play an important role in the next-generation energy storage landscape.

9. Conclusion

Overall, this Review establishes a cross-scale framework for understanding fast-charging AZIBs by linking the generation, amplification and failure consequences of polarization under XFC conditions. At the microscale, sluggish Zn^{2+} desolvation and charge-transfer kinetics create an ion-electron transport mismatch; at the mesoscale, nonuniform ion flux and uneven deposition magnify polarization; at the macroscale, the limited ESW converts accumulated overpotential into parasitic reactions and capacity loss. By organizing desolvation regulation, electrode-architecture design and electrolyte engineering within this scale framework, we clarify the central contradictions that constrain rapid and reversible AZIBs. Future advances should move beyond isolated performance optimization toward mechanism-guided, application-relevant design, enabling AZIBs to better leverage their intrinsic safety and cost advantages under XFC conditions.

Table 5. Distribution of XFC-regime validation across different strategy categories.

Scale	Original table	Strategy category	No. of strategies	IV, n (%)	III, n (%)	II, n (%)	I, n (%)	Note
Microscopic	Table 1	SEI structure and composition regulation	6	1 (16.7%)	3 (50.0%)	1 (16.7%)	1 (16.7%)	**SEI regulation shows slightly stronger high-severity validation than solvation regulation.**
		Liquid electrolyte solvation structure	9	1 (11.1%)	4 (44.4%)	2 (22.2%)	2 (22.2%)	
Mesoscopic	Table 2	Activating zinc foils	7	0 (0.0%)	3 (42.9%)	4 (57.1%)	0 (0.0%)	**Powder anodes are more relevant to practical high-loading XFC cells; foil activation is more uniformly validated at moderate/high rates.**
		Consolidating zinc powder anodes	19	1 (5.3%)	3 (15.8%)	6 (31.6%)	9 (47.4%)	
Macroscopic	Table 3	Solid-state electrolyte (SSE)	8	0 (0.0%)	1 (12.5%)	1 (12.5%)	6 (75.0%)	**Electrolyte strategies mainly serve as stability/safety enablers; Regime IV validation is still absent.**
		Quasi-solid-state electrolyte (Q-SSE)	13	0 (0.0%)	2 (15.4%)	2 (15.4%)	9 (69.2%)	
		Novel liquid electrolyte	15	0 (0.0%)	2 (13.3%)	5 (33.3%)	8 (53.3%)	
Microscopic summary	Table 1	All microscopic strategies	15	2 (13.3%)	7 (46.7%)	3 (20.0%)	3 (20.0%)	**Overall XFC-validation maturity follows: microscopic > mesoscopic > macroscopic**
Mesoscopic summary	Table 2	All mesoscopic strategies	26	1 (3.8%)	6 (23.1%)	10 (38.5%)	9 (34.6%)	
Macroscopic summary	Table 4	All macroscopic/electrolyte strategies	36	0 (0.0%)	5 (13.9%)	8 (22.2%)	23 (63.9%)	

Author contributions

Jingwen Liu: Conceptualization, Data curation, Formal analysis, Writing - original draft, Writing - review & editing. **Han Jiang**: Data curation, Formal analysis, Writing - review & editing. **Qianyi Chen**: Data curation, Writing - review & editing. **Xiang Guo**: Literature analysis, Writing - review & editing. **Hongxu Li**: Literature analysis, Writing - review & editing. **Viet Q. Bui:** Literature analysis, Writing. **Xinghui Liu**: Conceptualization, Supervision, Project administration, Writing - review & editing.

Data availability

The data that support the findings of this study are available from the corresponding author upon reasonable request.

Conflicts of interest

Xinghui Liu is an editorial board member for Composite Functional Materials and was not involved in the editorial review or the decision to publish this article. Other authors declare that there is no competing interests.

References

[1] Zachary M. Konz, Brendan M. Wirtz, Ankit Verma, TzuYang Huang, Helen K. Bergstrom, Matthew J. Crafton, David E. Brown, Eric J. McShane, Andrew M. Colclasure, Bryan D. McCloskey. High-throughput Li plating quantification for fast-charging battery design. *Nature Energy*, 2023, 8, 450-461. https://doi.org/10.1038/s41560-023-01194-y.

[2] Huigang Zhang, Xindi Yu, Paul V. Braun. Three-dimensional bicontinuous ultrafast-charge and -discharge bulk battery electrodes. *Nature Nanotechnology*, 2011, 6, 277-281. https://doi.org/10.1038/nnano.2011.38.

[3] Ishwar Chandra Yadav, Ram Sharan Bajpai, Sandeep Gupta, Anand Shukla. Hybrid fuzzy-MPC based multi-objective control strategy for fast charging of electric vehicles with advanced battery thermal management and renewable grid support. *Scientific Reports*, 2025, 15, 42342. https://doi.org/10.1038/s41598-025-26279-4.

[4] Peter M. Attia, Aditya Grover, Norman Jin, Kristen A. Severson, Todor M. Markov, Yanghung Liao, Michael H. Chen, Bryan Cheong, Nicholas Perkins, Zi Yang, Patrick K. Herring, Muratahan Aykol, Stephen J. Harris, Richard D. Braatz, Stefano Ermon, William C. Chueh. Closed-loop optimization of fast-charging protocols for batteries with machine learning. *Nature*, 2020, 578, 397-402. https://doi.org/10.1038/s41586-020-1994-5.

[5] Stephen Dongmin Kang, William C. Chueh. Probing the depths of battery heterogeneity. *Nature Nanotechnology*, 2023, 18, 1130-1130. https://doi.org/10.1038/s41565-023-01440-0.

[6] Eric J. Dufek, Daniel P. Abraham, Ira Bloom, Borrong Chen, Parameswara R. Chinnam, Andrew M. Colclasure, Kevin L. Gering, Matthew Keyser, Sangwook Kim, Weijie Mai, David C. Robertson, Marco-Tulio F. Rodrigues, Kandler Smith, Tanvir R. Tanim, Francois L.E. Usseglio-Viretta, Peter J. Weddle. Developing extreme fast charge battery protocols - A review spanning materials to systems. *Journal of Power Sources*, 2022, 526, 231129. https://doi.org/10.1016/j.jpowsour.2022.231129.

[7] Yuhang Dai, Ruihu Lu, Chengyi Zhang, Jiantao Li, Yifei Yuan, Yu Mao, Chumei Ye, Zhijun Cai, Jiexin Zhu, Jinghao Li, Ruohan Yu, Lianmeng Cui, Siyu Zhao, Qinyou An, Guanjie He, Geoffrey I. N. Waterhouse, Paul R. Shearing, Yang Ren, Jun Lu, Khalil Amine, Ziyun Wang, Liqiang Mai. Zn2+-mediated catalysis for fast-charging aqueous Zn-ion batteries. *Nature Catalysis*, 2024, 7, 776-784. https://doi.org/10.1038/s41929-024-01169-6.

[8] Mingzhuang Liu, Xinghua Li, Mengxia Cui, Feiyu Chen, Jiaxing Li, Weijian Shi, Yu Liu, Xiaowei Li, Yan Wang, Wei Zhang, Changlu Shao, Yichun Liu. Amorphous organic-hybrid vanadium oxide for near-barrier-free ultrafast-charging aqueous zinc-ion battery. *Nature Communications*, 2024, 15, 10769. https://doi.org/10.1038/s41467-024-55000-8.

[9] Suting Weng, Gaojing Yang, Simeng Zhang, Xiaozhi Liu, Xiao Zhang, Zepeng Liu, Mengyan Cao, Mehmet Nurullah Ateş, Yejing Li, Liquan Chen, Zhaoxiang Wang, Xuefeng Wang. Kinetic limits of graphite anode for fast-charging lithium-ion batteries. *Nano-Micro Letters*, 2023, 15, 215. https://doi.org/10.1007/s40820-023-01183-6.

[10] Shuibin Tu, Bao Zhang, Yan Zhang, Zihe Chen, Xiancheng Wang, Renming Zhan, Yangtao Ou, Wenyu Wang, Xuerui Liu, Xiangrui Duan, Li Wang, Yongming Sun. Fast-charging capability of graphite-based lithium-ion batteries enabled by Li3P-based crystalline solid-electrolyte interphase. *Nature Energy*, 2023, 8, 1365-1374. https://doi.org/10.1038/s41560-023-01387-5.

[11] Yangyang Liu, Haodong Shi, Zhongshuai Wu. Recent status, key strategies and challenging perspectives of fast-charging graphite anodes for lithium-ion batteries. *Energy & Environmental Science*, 2023, 16, 4834-4871. https://doi.org/10.1039/d3ee02213g.

[12] Borong Li, Yu Chao, Mengchao Li, Yuanbin Xiao, Rui Li, Kang Yang, Xiancai Cui, Gui Xu, Lingyun Li, Chengkai Yang, Yan Yu, David P. Wilkinson, Jiujun Zhang. A review of solid electrolyte interphase (SEI) and dendrite formation in lithium batteries. *Electrochemical Energy Reviews*, 2023, 6, 7. https://doi.org/10.1007/s41918-022-00147-5.

[13] Shouyi Yuan, Kai Ding, Xiaoyuan Zeng, Duan Bin, Yingjie Zhang, Peng Dong, Yonggang Wang. Advanced nonflammable organic electrolyte promises safer Li-metal batteries: From solvation structure perspectives. *Advanced Materials*, 2023, 35, 2206228. https://doi.org/10.1002/adma.202206228.

[14] Ziyang Ning, Guanchen Li, Dominic L. R. Melvin, Yang Chen, Junfu Bu, Dominic Spencer-Jolly, Junliang Liu, Bingkun Hu, Xiangwen Gao, Johann Perera, Chen Gong, Shengda D. Pu, Shengming Zhang, Boyang Liu, Gareth O. Hartley, Andrew J. Bodey, Richard I. Todd, Patrick S. Grant, David E. J. Armstrong, T. James Marrow, Charles W. Monroe, Peter G. Bruce. Dendrite initiation and propagation in lithium metal solid-state batteries. *Nature*, 2023, 618, 287-293. https://doi.org/10.1038/s41586-023-05970-4.

[15] Chris Greig, David Keto, Scott Hobart, Benjamin Finch, Ryan Winkler. Speeding up risk capital allocation to deliver net-zero ambitions. *Joule*, 2023, 7, 239-243. https://doi.org/10.1016/j.joule.2023.01.003.

[16] Yunhong Che, Xiaosong Hu, Remus Teodorescu. Opportunities for battery aging mode diagnosis of renewable energy storage. *Joule*, 2023, 7, 1405-1407. https://doi.org/10.1016/j.joule.2023.06.014.

[17] Xiulei Ji, Linda F. Nazar. Best practices for zinc metal batteries. *Nature Sustainability*, 2024, 7, 98-99. https://doi.org/10.1038/s41893-023-01257-8.

[18] Lauren E. Blanc, Dipan Kundu, Linda F. Nazar. Scientific challenges for the implementation of Zn-ion batteries. *Joule*, 2020, 4, 771-799. https://doi.org/10.1016/j.joule.2020.03.002.

[19] Fei Wang, Oleg Borodin, Tao Gao, Xiulin Fan, Wei Sun, Fudong Han, Antonio Faraone, Joseph A. Dura, Kang Xu, Chunsheng Wang. Highly reversible zinc metal anode for aqueous batteries. *Nature Materials*, 2018, 17, 543-549. https://doi.org/10.1038/s41563-018-0063-z.

[20] Linhui Chang, Hongwei Cheng, Jiamin Li, Lei Zhang, Bomian Zhang, Liheng Zheng, Qiangchao Sun, Jiantao Li, Xionggang Lu, Kangning Zhao. High-entropy solvation chemistry towards affordable and practical Ah-level zinc metal battery. *Nature Communications*, 2025, 16, 6134. https://doi.org/10.1038/s41467-025-61456-z.

[21] Giorgia Zampardi, Fabio La Mantia. Open challenges and good experimental practices in the research field of aqueous Zn-ion batteries. *Nature Communications*, 2022, 13, 687. https://doi.org/10.1038/s41467-022-28381-x.

[22] Boya Tang, Lutong Shan, Shuquan Liang, Jiang Zhou. Issues and opportunities facing aqueous zinc-ion batteries. *Energy & Environmental Science*, 2019, 12, 3288-3304. https://doi.org/10.1039/c9ee02526j.

[23] Chaowei Li, Yinhao Xiao, Xiaoge Li, Haili Hou, Fengjun Hou, Jingchao Zhang, Daojun Zhang, Weimin Du. Towards high-energy-density aqueous Zn-ion batteries: from fundamental challenges to integrated design strategies. *Journal of Materials Chemistry A*, 2026, 14, 25800-25828. https://doi.org/10.1039/d6ta03875a.

[24] Long Jiang, Dongmin Li, Xian Xie, Dongdong Ji, Liwei Li, Le Li, Zhangxing He, Bingan Lu, Shuquan Liang, Jiang Zhou. Electric double layer design for Zn-based batteries. *Energy Storage Materials*, 2023, 62, 102932. https://doi.org/10.1016/j.ensm.2023.102932.

[25] Chun Chen, Zuxin Long, Xiaoyang Du, Liansheng Li, Qinghua Liang, Dongliang Chao, Dan Li. Interfacial ionic effects in aqueous zinc metal batteries. *Energy Storage Materials*, 2024, 71, 103571. https://doi.org/10.1016/j.ensm.2024.103571.

[26] Wenhao Ma, Sunyufei Wang, Xianwen Wu, Wenwen Liu, Fan Yang, Shude Liu, Seong Chan Jun, Lei Dai, Zhangxing He, Qiaobao Zhang. Tailoring desolvation strategies for aqueous zinc-ion batteries. *Energy & Environmental Science*, 2024, 17, 4819-4846. https://doi.org/10.1039/d4ee00313f.

[27] Wenyong Chen, Yanyan Wang, Fengmei Wang, Zihao Zhang, Wei Li, Guozhao Fang, Fei Wang. Zinc chemistries of hybrid electrolytes in zinc metal batteries: from solvent structure to interfaces. *Advanced Materials*, 2024, 36, 2411802. https://doi.org/10.1002/adma.202411802.

[28] Wenjing Deng, Ge Li, Xiaolei Wang. Zinc-ion battery chemistries enabled by regulating electrolyte solvation structure. *Advanced Functional Materials*, 2024, 34, 2405012. https://doi.org/10.1002/adfm.202405012.

[29] Yuhang Dai, Chengyi Zhang, Xinyu Zhang, Peie Jiang, Jie Chen, Wei Zong, Sicheng Zheng, Xuan Gao, Thomas J. Macdonald, Guanjie He. Interfacial energy storage in aqueous zinc-ion batteries. *Energy & Environmental Science*, 2025, 18, 9018-9030. https://doi.org/10.1039/d5ee03741g.

[30] Yan Ran, Huaping Zhao, Yong Lei. A review on strategies toward high-mass-loading aqueous zinc-ion batteries. *Journal of Materials Chemistry A*, 2026, 14, 8452-8482. https://doi.org/10.1039/d5ta08145a.

[31] Joseph F. Parker, Jesse S. Ko, Debra R. Rolison, Jeffrey W. Long. Translating materials-level performance into device-relevant metrics for Zinc-based batteries. *Joule*, 2018, 2, 2519-2527. https://doi.org/10.1016/j.joule.2018.11.007.

[32] Zequan Zhao, Qingquan Ye, Yangyang Liu, Bingan Lu, Shuquan Liang, Jiang Zhou. Advanced Ah-level zinc metal batteries. *Chemical Society Reviews*, 2026, 55, 1271-1292. https://doi.org/10.1039/d5cs00371g.

[33] Wei Lv, Junlin Liu, Zilei Shen, Xudong Li, Chao Xu. Novel approaches to aqueous zinc-ion batteries: Challenges, strategies, and prospects. *eScience*, 2025, 5, 100410. https://doi.org/10.1016/j.esci.2025.100410.

[34] Zhen Ji, Yingliang Zhao, Xianfu Zhang, Songlin Wang, Xinyuan Jia, Zhi Fang, Long Zhang, Yanglong Hou. Multiscale computational insights for hydrogel electrolytes in aqueous Zinc metal batteries. *Advanced Energy Materials*, 2026, 16, e71071. https://doi.org/10.1002/aenm.71071.

[35] Jenitha Moses, Ajay Rakkesh Rajendran. From atoms to algorithms: a review of machine learning approaches to cathode material innovation in zinc-ion batteries. *Journal of Materials Chemistry A*, 2025, 13, 34033-34054. https://doi.org/10.1039/d5ta04723d.

[36] Huiying Zhang, Fanghua Ning, Yiming Guo, Sidra Subhan, Xiaoyu Liu, Siqi Shi, Shigang Lu, Yongyao Xia, Jin Yi. Unraveling the mechanisms of aqueous Zinc ion batteries via First-Principles Calculations. *ACS Energy Letters*, 2024, 9, 4761-4784. https://doi.org/10.1021/acsenergylett.4c02014.

[37] Yida Hu, Peiyuan Wang, Mingzhu Li, Zhexuan Liu, Shuquan Liang, Guozhao Fang. Challenges and industrial considerations towards stable and high-energy-density aqueous zinc-ion batteries. *Energy & Environmental Science*, 2024, 17, 8078-8093. https://doi.org/10.1039/d4ee03628j.

[38] Junyi Yin, Zhiqi Wu, Shun Zhang, Xiaorui Liu, Yunpeng Liu, Huajun Tian. A review of the water dilemma and hydrogen-bond chemistry for aqueous zinc-ion batteries. *Energy & Environmental Science*, 2025, 18, 10263-10285. https://doi.org/10.1039/d5ee05775b.

[39] Yuting Xia, Ye Xiao, Jingxi Zhang, Yanhao Dong, Changan Wang. Designing microemulsion electrolytes with widened electrochemical stability window for highly reversible aqueous Zinc ion batteries. *Advanced Functional Materials*, 2025, 35, 2500889. https://doi.org/10.1002/adfm.202500889.

[40] Qing Ai, Boyu Zhang, Xing Liu, Bongki Shin, Wenhua Guo, Guanhui Gao, Lihong Zhao, Xintong Weng, Qiyi Fang, Tianshu Zhai, Doug Steinbach, Yifan Zhu, Yifeng Liu, Fan Wang, Xiaoyin Tian, Hua Guo, Youtian Zhang, Xuan Zhao, Yimo Han, Ming Tang, Yan Yao, Ting Zhu, Huajian Gao, Jun Lou. Strong and brittle lithium dendrites. *Science*, 2026, 391,

1125-1129. https://doi.org/10.1126/science.adu9988.

[41] Dechao Meng, Zhichen Xue, Guokang Chen, Dengke Zhou, Yushi He, Zifeng Ma, Yijin Liu, Linsen Li. Multiscale correlative imaging reveals sequential and heterogeneous degradations in fast-charging batteries. *Energy & Environmental Science*, 2024, 17, 4658-4669. https://doi.org/10.1039/D4EE01497A.

[42] Longsheng Cao, Dan Li, Enyuan Hu, Jijian Xu, Tao Deng, Lin Ma, Yi Wang, Xiaoqing Yang, Chunsheng Wang. Solvation structure design for aqueous Zn metal batteries. *Journal of the American Chemical Society*, 2020, 142, 21404-21409. https://doi.org/10.1021/jacs.0c09794.

[43] Shiqiang Wei, Quan Zhou, Shuangming Chen, Yixiu Wang, Pengjun Zhang, Wei Jiang, Changda Wang, Jiewu Cui, Xiaojun Wu, Li Song. Anion-mediated solvation structures and intercalation chemistry of aqueous zinc-ion electrolytes. *Proceedings of the National Academy of Sciences*, 2026, 123, e2524561123. https://doi.org/10.1073/pnas.2524561123.

[44] Xiaomin Li, Xinyu Wang, Longtao Ma, Wei Huang. Solvation structures in aqueous metal-ion batteries. *Advanced Energy Materials*, 2022, 12, 2202068. https://doi.org/10.1002/aenm.202202068.

[45] Zhihong Piao, Runhua Gao, Yingqi Liu, Guangmin Zhou, Huiming Cheng. A review on regulating Li^+ solvation structures in carbonate electrolytes for lithium metal batteries. *Advanced Materials*, 2023, 35, 2206009. https://doi.org/10.1002/adma.202206009.

[46] Chunchuan Kao, Chao Ye, Junnan Hao, Jieqiong Shan, Huan Li, Shizhang Qiao. Suppressing hydrogen evolution *via* anticatalytic interfaces toward highly efficient aqueous Zn-ion batteries. *ACS Nano*, 2023, 17, 3948-3957. https://doi.org/10.1021/acsnano.2c12587.

[47] Xiaoyu Yu, Ming Chen, Zhengang Li, Xi Tan, Haitang Zhang, Junhao Wang, Yonglin Tang, Juping Xu, Wen Yin, Yang Yang, Dongliang Chao, Fei Wang, Yeguo Zou, Guang Feng, Yu Qiao, Haoshen Zhou, Shigang Sun. Unlocking dynamic solvation chemistry and hydrogen evolution mechanism in aqueous zinc batteries. *Journal of the American Chemical Society*, 2024, 146, 17103-17113. https://doi.org/10.1021/jacs.4c02558.

[48] Zhengyu Ju, Tianrui Zheng, Bowen Zhang, Guihua Yu. Interfacial chemistry in multivalent aqueous batteries: fundamentals, challenges, and advances. *Chemical Society Reviews*, 2024, 53, 8980-9028. https://doi.org/10.1039/d4cs00474d.

[49] Xiuli Guo, Qiaoling Peng, Rui Yang, Gengyou Cao, Jianfeng Wen, Kyungsoo Shin, Ye Zheng, Sarayut Tunmee, Caineng Zou, Yongping Zheng, Xiaolong Zhou, Yongbing Tang. Non-coordinating charge transfer enables ultrafast desolvation of hydrated zinc ions in the outer Helmholtz layer for stable aqueous Zn metal batteries. *National Science Review*, 2025, 12, nwaf070. https://doi.org/10.1093/nsr/nwaf070.

[50] Lijing Yan, Qiangxiang Zhai, Shaojian Zhang, Zeheng Li, Qiaoling Kang, Xuehui Gao, Chengbin Jin, Tiefeng Liu, Tingli Ma, Zhan Lin. The burgeoning zinc powder anode for aqueous zinc metal batteries: from electrode preparation to performance enhancement. *Advanced Energy Materials*, 2024, 14, 2401328. https://doi.org/10.1002/aenm.202401328.

[51] Qingli Zou, Zhuojian Liang, Wanwan Wang, Dejian Dong, Yichun Lu. A nuclei-rich strategy for highly reversible dendrite-free zinc metal anodes. *Energy & Environmental Science*, 2023, 16, 6026-6034. https://doi.org/10.1039/d3ee03246a.

[52] Zhixiao Xu, Yue Li, Ge Li, Hao Zhang, Xiaolei Wang. Reversible zinc powder anode via crystal facet engineering. *Matter*, 2023, 6, 3075-3086. https://doi.org/10.1016/j.matt.2023.06.045.

[53] Hongli Chen, Wanyu Zhang, Shan Yi, Zhe Su, Zhiqiang Zhao, Yayun Zhang, Bo Niu, Donghui Long. Zinc iso-plating/stripping: toward a practical Zn powder anode with ultra-long life over 5600 h. *Energy & Environmental Science*, 2024, 17, 3146-3156. https://doi.org/10.1039/d3ee04333a.

[54] Qing Li, Nan Li, Chunyi Zhi. Zinc powder anodes for rechargeable aqueous zinc-based batteries. *Nano Letters*, 2024, 24, 4055-4063. https://doi.org/10.1021/acs.nanolett.4c00101.

[55] Biao Fu, Guanqun Liu, Yajue Zhang, Zhexuan Liu, Xuefang Xie, Guozhao Fang, Shuquan Liang. Zn powder-based anodes for aqueous Zn metal batteries: strategies, structures, and perspectives. *ACS Energy Letters*, 2024, 9, 3292-3307. https://doi.org/10.1021/acsenergylett.4c00628.

[56] Yanxin Li, Hongfeng Jia, Usman Ali, Haozhi Wang, Bingqiu Liu, Lu Li, Lingyu Zhang, Chungang Wang. Successive gradient internal electric field strategy toward dendrite-free zinc metal anode. *Advanced Energy Materials*, 2023, 13, 2301643. https://doi.org/10.1002/aenm.202301643.

[57] Xiaomeng Tian, Ying Sun, Hui Li, Xiaoguang Duan, Qin Zhao, Tianyi Ma. Crystallographic texturing of electrodeposits for sustainable Zn anodes. *Advanced Energy Materials*, 2025, 15, 2403995. https://doi.org/10.1002/aenm.202403995.

[58] Zhicheng Xiang, Yubing Qiu, Xingpeng Guo, Kai Qi, Zhenglong Xu, Bao Yu Xia. Inherited construction of porous zinc hydroxide sulfate layer for stable dendrite-free Zn anode. *Energy & Environmental Science*, 2024, 17, 3409-3418. https://doi.org/10.1039/d4ee00721b.

[59] Youngju Lee, Bingyuan Ma, Peng Bai. Concentration polarization and metal dendrite initiation in isolated electrolyte microchannels. *Energy & Environmental Science*, 2020, 13, 3504-3513. https://doi.org/10.1039/d0ee01874k.

[60] Dawei Xi, Abdulrahman M. Alfaraidi, Jinxu Gao, Thomas Cochard, Luana C. I. Faria, Zheng Yang, Thomas Y. George, Taobo Wang, Roy G. Gordon, Richard Y. Liu, Michael J. Aziz. Mild pH-decoupling aqueous flow battery with practical pH recovery. *Nature Energy*, 2024, 9, 479-490. https://doi.org/10.1038/s41560-024-01474-1.

[61] Mingcong Tang, Qun Liu, Xiaohong Zou, Biao Zhang, Liang An. High-energy-density aqueous Zinc-ion batteries: recent progress, design strategies, challenges, and perspectives. *Advanced Materials*, 2025, 37, 2501361. https://doi.org/10.1002/adma.202501361.

[62] Rongyu Deng, Zhenjiang He, Fulu Chu, Jie Lei, Yi Cheng, You Zhou, Feixiang Wu. An aqueous electrolyte densified by perovskite SrTiO3 enabling high-voltage zinc-ion batteries. *Nature Communications*, 2023, 14, 4981. https://doi.org/10.1038/s41467-023-40462-z.

[63] Guoxing Li. Regulating mass transport behavior for high-performance lithium metal batteries and fast-charging lithium-ion batteries. *Advanced energy Materials*, 2021, 11, 2002891. https://doi.org/10.1002/aenm.202002891.

[64] Lukas Stolz, Gerrit Homann, Martin Winter, Johannes Kasnatscheew. The sand equation and its enormous practical relevance for solid-state lithium metal batteries. *Materials Today*, 2021, 44, 9-14. https://doi.org/10.1016/j.mattod.2020.11.025.

[65] Chengjun Xu, Baohua Li, Hongda Du, Feiyu Kang. Energetic Zinc ion chemistry: the rechargeable zinc ion batteriesy. *Angewandte Chemie International Edition*, 2012, 51, 933-935. https://doi.org/10.1002/anie.201106307.

[66] Qi Yang, Guojin Liang, Ying Guo, Zhuoxin Liu, Boxun Yan, Donghong Wang, Zhaodong Huang, Xinliang Li, Jun Fan, Chunyi Zhi. Do zinc dendrites exist in neutral zinc batteries: A developed electrohealing strategy to *in situ* rescue in-service batteries. *Advanced Materials*, 2019, 31, 1903778. https://doi.org/10.1002/adma.201903778.

[67] Penghui Cao, Xiangyang Zhou, Anran Wei, Qi Meng, Han Ye, Weiping Liu, Jingjing Tang, Juan Yang. Fast-charging and ultrahigh-capacity zinc metal anode for high-performance aqueous zinc-ion batteries. *Advanced Functional Materials*, 2021, 31, 2100398. https://doi.org/10.1002/adfm.202100398.

[68] Zhen Hou, Yao Gao, Rui Zhou, Biao Zhang. Unraveling the rate-dependent stability of metal anodes and its implication in designing cycling protocol. *Advanced Functional Materials*, 2022, 32, 2107584. https://doi.org/10.1002/adfm.202107584.

[69] Zhimeng Hao, Yufeng Zhang, Zhenkun Hao, Geng Li, Yong Lu, Song Jin, Gaojing Yang, Sihan Zhang, Zhenhua Yan, Qing Zhao, Jun Chen. Metal anodes with ultrahigh reversibility enabled by the closest packing crystallography for sustainable batteries. *Advanced Materials*, 2023, 35, 2209985. https://doi.org/10.1002/adma.202209985.

[70] Zhuoxi Wu, Yu Wang, Chunyi Zhi. Zinc-anode reversibility and capacity inflection as an evaluation criterion. *Joule*, 2024, 8, 2442-2448. https://doi.org/10.1016/j.joule.2024.07.023.

[71] He Gan, Huan Li, Minwei Xu, Cuiping Han, Huiming Cheng. Failure mechanisms and remedy of an ultrathin Zn metal anode in pouch cells. *Joule*, 2024, 8, 3054-3071. https://doi.org/10.1016/j.joule.2024.07.013.

[72] Mingyan Chuai, Hao Tong, Zimin Yang, Siting Deng, Mingqiang Wu, Jidan Xing, Guoliang Chai. Design of a P-O-M (M = Mn, Zn) d-pπ backbonding electrolyte additive for 40 Ah electrolytic Zn-MnO_2 batteries. *Journal of the American Chemical Society*, 2025, 147, 31591-31602. https://doi.org/10.1021/jacs.5c06922.

[73] Haoyu Li, Sijie Li, Ruilin Hou, Yuan Rao, Shaohua Guo, Zhi Chang, Haoshen Zhou. Recent advances in zinc-ion dehydration strategies for optimized Zn-metal batteries. *Chemical Society Reviews*, 2024, 53, 7742-7783. https://doi.org/10.1039/d4cs00343h.

[74] Dongdong Wang, Hongxia Liu, Dan Lv, Cheng Wang, Jian Yang, Yitai Qian. Rational screening of artificial solid electrolyte Interphases on Zn for ultrahigh-rate and long-life aqueous batteries. *Advanced Materials*, 2023, 35, 2207908. https://doi.org/10.1002/adma.202207908.

[75] Mengqi Zhu, Xuran Li, Jinyan Zhong, Meiling Zhong, Linlan Huang, Jindan Zhang. Zincophilic hydrogen-bonded organic frameworks with vertical channels enabling fast ion-transport kinetics and interface stability toward ultrastable Zn anodes. *Nano Letters*, 2025, 25, 13258-13266. https://doi.org/10.1021/acs.nanolett.5c03302.

[76] Yating Li, Zuhao Yu, Jianhang Huang, Yonggang Wang, Yongyao Xia. Constructing solid electrolyte interphase for aqueous Zinc batteries. *Angewandte Chemie International Edition*, 2023, 62, e202309957. https://doi.org/10.1002/anie.202309957.

[77] Xinpeng Han, Jinpeng Han, Kang Ma, Jiaqi Wen, Lianpeng Li, Daliang Han, Jie Sun. A fluoride gradient, Zn-salt-rich hydrophobic interphase formed by a zincophilic, hydrophobic, anion-philic polymer “skin” for an anode-free solid Zn battery. *energy & Environmental Science*, 2024, 17, 9244-9254. https://doi.org/10.1039/d4ee01978d.

[78] Wanting Zhou, Zetao Chen, Shunshun Zhao, Shimou Chen. Superhydrophobic and highly flexible artificial solid electrolyte Interphase inspired by Lotus effect toward highly stable Zn anode. *Advanced Functional Materials*, 2024, 34, 2409520. https://doi.org/10.1002/adfm.202409520.

[79] Yanyan Wang, Zhijie Wang, Wei Kong Pang, Wilford Lie, Jodie A. Yuwono, Gemeng Liang, Sailin Liu, Anita M. D’ Angelo, Jiaojiao Deng, Yameng Fan, Kenneth Davey, Baohua Li, Zaiping Guo. Solvent control of water O-H bonds for highly reversible zinc ion batteries. *Nature Communications*, 2023, 14, 2720. https://doi.org/10.1038/s41467-023-38384-x.

[80] Dawei Sheng, Xiaoxu Liu, Zhuo Yang, Man Zhang, Yang Li, Peipei Ren, Xueru Yan, Ze Xiang Shen, Dongliang Chao. Hydrogen bond network regulation in electrolyte structure for Zn-based aqueous batteries. *Advanced Functional Materials*, 2024, 34, 2402014. https://doi.org/10.1002/adfm.202402014.

[81] Ming Li, Xuanpeng Wang, Jiashen Meng, Chunli Zuo, Buke Wu, Cong Li, Wei Sun, Liqiang Mai. Comprehensive understanding of hydrogen bond chemistry in aqueous batteries. *Advanced Materials*, 2024, 36, 2308628. https://doi.org/10.1002/adma.202308628.

[82] Ruiyu Qi, Wenhao Tang, Yiliang Shi, Kewei Teng, Yirui

Deng, Lei Zhang, Junqing Zhang, Ruiping Liu. Gel Polymer electrolyte toward large-scale application of aqueous zinc batteries. *Advanced Functional Materials*, 2023, 33, 2306052. https://doi.org/10.1002/adfm.202306052.

[83] Long Qian, Haojie Zhu, Tingting Qin, Rui Yao, Jianwei Zhao, Feiyu Kang, Cheng Yang. Ultralow-salt-concentration electrolyte for high-voltage aqueous Zn metal batteries. *Advanced Functional Materials*, 2023, 33, 2301118. https://doi.org/10.1002/adfm.202301118.

[84] Junpeng Xie, Dewu Lin, Hang Lei, Shuilin Wu, Jinliang Li, Wenjie Mai, Pengfei Wang, Guo Hong, Wenjun Zhang. Electrolyte and interphase engineering of aqueous batteries beyond "water-in-salt" strategy. *Advanced Materials*, 2024, 36, 2306508. https://doi.org/10.1002/adma.202306508.

[85] Jingying Li, Kui Xu, Jia Yao, Yiyuan Yang, Ziang Wu, Jieqiong Zhang, Xu Chen, Junjie Zheng, Yin Yang, Xingtai Liu, Xiaofang Wang, Yi Gan, Wei Hu, Lin Lv, Guokun Ma, Li Tao, Hanbin Wang, Jun Zhang, Hao Wang, Houzhao Wan. Nanofluid channels mitigated Zn2+ concentration polarization prolonged over 30 times lifespan for reversible zinc anodes. *energy Storage Materials*, 2024, 73, 103844. https://doi.org/10.1016/j.ensm.2024.103844.

[86] Chao Yi, Long Jiao, Jizhen Wang, Yuchao Ma, Hongyuan Bai, Qiaoyun Liu, Shaoyu Wang, Wei Xin, Yechen Lei, Tian Zhang, Leixin Yang, Dengkun Shu, Shuo Yang, Kaihua Li, Chenyang Li, Huan Li, Wenjun Zhang, Bowen Cheng. Multi-scale functionally designed $ZnWO_4$ artificial interphase for ultra-stable aqueous Zn metal anodes under high current rates. *Advanced Functional Materials*, 2024, 34, 2404579. https://doi.org/10.1002/adfm.202404579.

[87] Na Gao, Manying Cui, Kai Xi, Teng Deng, Dandan Yin, Jingjie He, Xiaofeng Cui, Limin Liu, Weiping Li, Shujiang Ding, Guoxin Gao, Hongyang Zhao. Elimination of concentration polarization under ultra-high current density zinc deposition by nanofluid self-driven ion enrichment. *Advanced Materials*, 2025, 37, 2419034. https://doi.org/10.1002/adma.202419034.

[88] Jinqiu Zhou, Lifang Zhang, Mingji Peng, Xi Zhou, Yufeng Cao, Jie Liu, Xiaowei Shen, Chenglin Yan, Tao Qian. Diminishing interfacial turbulence by colloid-polymer electrolyte to stabilize zinc ion flux for deep-cycling Zn metal batteries. *Advanced Materials*, 2022, 34, 2200131. https://doi.org/10.1002/adma.202200131.

[89] Yan Dao, Mengyuan Li, Miaomiao Zhang, Ke Fan, Qi Qi, Lin Zhang, Xinyao Yu. Axial Coordination induced electron delocalization and p-p orbital hybridization in single-atom catalysts boosts Zn^{2+} desolvation for highly stable Zn anode. *Advanced Science*, 2026, 13, e18148. https://doi.org/10.1002/advs.202518148.

[90] Guoxin Yang, Xiangrong Zhang, Hanqi Zhang, Chengwei Wu, Ning Zhao, Yiming Fan, Feng Jin, Jiaqi Wang, Xiuxia Zhao, Shujiang Ding, Hongyang Zhao, Xiaofei Hu. Hydrogen bond-anchored interfacial engineering for stable and high-performance aqueous zinc-ion batteries. *eScience energy*, 2026, 2, 100027. https://doi.org/10.1016/j.esen.2026.100027.

[91] Kai Liu, Yanchen Sun, Yingjie Zhang, Qian Ying, Peng Chen, Tauseef Shahid, Yefeng Yang. Constructing a dual interfacial layer of zinc phytate and halloysite nanotubes with enhanced ion sieving and desolvation for an ultrastable zinc metal anode. *energy & Fuels*, 2025, 39, 22680-22690. https://doi.org/10.1021/acs.energyfuels.5c04574.

[92] Geun Yoo, Yong-Ryun Jo, Geon-Hyoung An. Multifunctional zinc vanadium oxide layer on metal anodes via ultrathin surface coating for enhanced stability in aqueous zinc-ion batteries. *ACS energy Letters*, 2024, 9, 5955-5965. https://doi.org/10.1021/acsenergylett.4c02573.

[93] Feiyu Tao, Yingke Ren, Li'e Mo, Yifan Wang, Yang Huang, Hong Zhang, Chengwu Shi, Zhaoqian Li, Jiaqin Liu, Lei Chen, Linhua Hu, Yucheng Wu. Exposing Zn(002) texture with sucralose additive for stable and dendrite-free aqueous zinc-ion batteries. *Nano-Micro Letters*, 2026, 18, 107. https://doi.org/10.1007/s40820-025-01954-3.

[94] Mengke Su, Haozhen Dou, Jinliang Yan, Sitong Liu, Mi Xu, Chuangwei Liu, Xin Wang, Zhongwei Chen. Multisite cooperative regulation of solvation and interface *via* dynamic additive engineering for highly reversible zinc batteries. *Angewandte Chemie International Edition*, 2025, 64, e202511685. https://doi.org/10.1002/anie.202511685.

[95] Jingxuan Ren, Dongdong Wang, Qingying Li, Yizhou Liu, Xinli Guo, Qianyi Ma, Yihang Nie, Haozhen Dou, Dongxin Wang, Dan Luo, Zhongwei Chen. Achieving bichelating solvation structure toward fast charging and long lifespan aqueous Zn-ion batteries. *Advanced Materials*, 2026, 38, e05049. https://doi.org/10.1002/adma.202505049.

[96] Kexuan Zang, Wenqi Song, YanPing Sun, Puang Lu, Sufeng Zhang, Zongchen Miao, Liwei Qian, Valentin Nica, Mohaned Hammad. Solvation-interface coupling strategy enables dendrite-free zinc anodes via amino acid-derived poly(ionic liquid) films. *Chemical Engineering Journal*, 2025, 520, 165800. https://doi.org/10.1016/j.cej.2025.165800.

[97] Mingzhe Fang, Yanqun Lv, Ming Zhao, Chenyue Huang, Qianwen Dong, Mingjun Ma, Linze Xu, Yunkai Xu, Jun Lu. Solvent engineering-driven anion chemistry enables stable Zn interfaces for wide-temperature aqueous zinc batteries. *Advanced Functional Materials*, 2026, 36, e23560. https://doi.org/10.1002/adfm.202523560.

[98] Haozhen Dou, Xinru Wu, Mi Xu, Renwu Feng, Qianyi Ma, Dan Luo, Kai Zong, Xin Wang, Zhongwei Chen. Steric-hindrance effect tuned ion solvation enabling high-performance aqueous zinc ion batteries. *Angewandte Chemie*, 2024, 136, e202401974. https://doi.org/10.1002/ange.202401974.

[99] Zhenyue Xing, Pei Ye, Xiaodong Shi, Lutong Shan, Shan Guo, Mingyang Chen, Yuxuan Xia, Yating Gao, Hamdy Khamees Thabet, Taghreed F. Altamimi, Zeinhom M. El-Bahy, Xinlong Tian, Jiang Zhou. Design of cryogenic

electrolyte with organic-free solvation structure for wide-temperature zinc metal batteries. *Angewandte Chemie International Edition*, 2025, 64, e202516974. https://doi.org/10.1002/anie.202516974.

[100] Hao Tan, Chao Meng, Yuping Zhang, Jieying Zhao, Hao Chen, Long Chen, Zhao-Hua Yin, Xinglong Wu, Hong Liu, Jianjun Wang. Decoupling of ion-solvent interactions *via* compartmentalized molecular design for ultra-stable aqueous zinc batteries. *Advanced Functional Materials*, 2026, 36, e16270. https://doi.org/10.1002/adfm.202516270.

[101] Junjie Zheng, Bao Zhang, Xin Chen, Wenyu Hao, Jia Yao, Jingying Li, Yi Gan, Xiaofang Wang, Xingtai Liu, Ziang Wu, Youwei Liu, Lin Lv, Li Tao, Pei Liang, Xiao Ji, Hao Wang, Houzhao Wan. Critical solvation structures arrested active molecules for reversible Zn electrochemistry. Nano-Micro Letters, 2024, 16, 145. https://doi.org/10.1007/s40820-024-01361-0.

[102] Xiaoyu Yu, Ming Chen, Junhao Wang, Shiqi Li, Haitang Zhang, Qingao Zhao, Haiyan Luo, Yaping Deng, Hanfeng Liang, Jiang Zhou, Fei Wang, Dongliang Chao, Yeguo Zou, Guang Feng, Yu Qiao, Shigang Sun. Deciphering multi-dimensional interfacial mechanisms via organic cosolvent engineering for sustainable zinc metal batteries. *Nature Communications*, 2025, 16, 3820. https://doi.org/10.1038/s41467-025-59069-7.

[103] Xinhua Zheng, Bibo Han, Chaofan Liu, Ruilin Li, Chengchao Li, Shikai Liu, Faxing Wang, Yuping Wu. Taming zinc electrodeposition from the root to break zinc utilization/capacity barriers in practical zinc batteries. *energy & Environmental Science*, 2026, 19, 1028-1041. https://doi.org/10.1039/d5ee05711f.

[104] Xin Liu, Jiawei Qian, Jingwei Chen, Yunkai Xu, Weiyi Wang, Weixu Dong, Wei Hu, Guorui Cai, Jun Lu, Shuhong Yu, Lifeng Chen. A sustainable and scalable approach for *in situ* induction of gradient nucleation sites in biomass-derived interface layers for ultra-stable aqueous zinc metal batteries. *Angewandte Chemie*, 2025, 137, e202504613. https://doi.org/10.1002/ange.202504613.

[105] Ruizheng Zhao, Xusheng Dong, Pei Liang, Hongpeng Li, Tengsheng Zhang, Wanhai Zhou, Boya Wang, Zhoudong Yang, Xia Wang, Lipeng Wang, Zhihao Sun, Fanxing Bu, Zaiwang Zhao, Wei Li, Dongyuan Zhao, Dongliang Chao. Prioritizing hetero-metallic interfaces *via* thermodynamics inertia and kinetics zincophilia metrics for tough Zn-based aqueous batteries. *Advanced Materials*, 2023, 35, 2209288. https://doi.org/10.1002/adma.202209288.

[106] Pengfei Zhang, Chao Geng, Canhuang Li, Jin-Ming Wu, Minhua Cao, Tulai Sun, Wei Wen. Micro-terraced surface induced directional two-dimensional diffusion enables dendrite-free zinc anodes. *Advanced Materials*, 2026, 38, e72560. https://doi.org/10.1002/adma.72560.

[107] Zhe Bie, Qi Yang, Xinxin Cai, Ze Chen, Zhaoyang Jiao, Junbo Zhu, Zhongfeng Li, Jinzhang Liu, Weixing Song, Chunyi Zhi. One-step construction of a polyporous and zincophilic interface for stable zinc metal anodes. *Advanced energy Materials*, 2022, 12, 2202683. https://doi.org/10.1002/aenm.202202683.

[108] Feng Yang, Le Zhou, Tianyu Zhang, Hongfei Wang, Chuqiao Xia, Zhongqing Ma, Yong Hu. A zincophilic and negatively-charged self-reconstructed stratified interface for regulating Zn^{2+} conduction and nucleation toward conformal dendrite-free deposition. *Angewandte Chemie International Edition*, 2026, 65, e23653. https://doi.org/10.1002/anie.202523653.

[109] Xin Zhao, Yong Gao, Qinghe Cao, Fan Bu, Jie Pu, Yuxuan Wang, Cao Guan. A high-capacity gradient Zn powder anode for flexible Zn-ion batteries. *Advanced energy Materials*, 2023, 13, 2301741. https://doi.org/10.1002/aenm.202301741.

[110] Penghui Cao, Mengdi Wu, Huali Zhu, Juan Yang, Shenao Pan, Shuang Zhou, Yuejiao Chen, Chuanchang Li. A high-stability zinc powder anode built on the similarity compatibility principle. *Advanced Functional Materials*, 2026, 36, e15225. https://doi.org/10.1002/adfm.202515225.

[111] Jiahao Tang, Jiale Cao, Yunxuan Jiang, Siying Gou, Ruiqi Yao, Yingqi Li, Botian Liu. Spraying amorphous carbon coated zinc to prepare powder-based anodes for long-life zinc-ion batteries. *Green Chemistry*, 2024, 26, 7990-7996. https://doi.org/10.1039/d4gc01812e.

[112] Xinliang Li, Qing Li, Yue Hou, Qi Yang, Ze Chen, Zhaodong Huang, Guojin Liang, Yuwei Zhao, Longtao Ma, Mian Li, Qing Huang, Chunyi Zhi. Toward a practical Zn powder anode: Ti_3 C_2 T x MXene as a lattice-match electrons/ions redistributor. *ACS Nano*, 2021, 15, 14631-14642. https://doi.org/10.1021/acsnano.1c04354.

[113] Wenying Tang, Lanhe Zhang, Yang Liu, Sen Wang, Jian Zhang. A dual-functional DMDAAC electrode enhancer with hydrophobic effect for highly stable Zn powder composite anode. *energy Storage Materials*, 2025, 76, 104127. https://doi.org/10.1016/j.ensm.2025.104127.

[114] Qi Li, Chun Fang, Chunze Yan. Interfacial alloying-induced 0ptimization of Zn^{2+} diffusion and atomic migration for stable aqueous Zn batteries. *Advanced Functional Materials*, 2025, 35, 2509192. https://doi.org/10.1002/adfm.202509192.

[115] Hyunseo Kang, Seung-Hyeok Kim, David B. Ahn, Xiao Wang, Zhongshuai Wu, Sang-Young Lee. Liquid metal-skinned Zn powder anodes enabled by capillary suspension. *ACS energy Letters*, 2024, 9, 2816-2825. https://doi.org/10.1021/acsenergylett.4c01009.

[116] Qi Li, Sihan Tang, Ruiying Luo, Peng Wei, Peng Chen, Jianlong Cong, Guizhou Liu, Zhufeng Liu, Yizhong Gou, Hongzhi Wu, Shixiong Sun, Jiantao Han, Yusheng Shi, Chun Fang, Chunze Yan. Regulating the local chemical environment of Zn powder surface by multi-site anchoring effect to achieve highly-stable Zn anode. *energy Storage Materials*, 2024, 66, 103229. https://doi.org/10.1016/j.ensm.2024.103229.

[117] Yiming Sun, Yanting Jin, Jiaxing Huang. Passivated Zn powders as metal anode. *Advanced Materials Interfaces*, 2025, 12, 2400643. https://doi.org/10.1002/admi.202400643.

[118] Jiayi Ning, Yuan Li, Penghui Cao, Shanshan Li, Yuejiao Chen, Shuang Zhou, Huali Zhu, Juan Yang, Chuanchang Li, Xiongjun Liu, Zhaoping Lu. Dragon-scale-inspired phosphate interface for enhanced stability of Zn powder anodes. *Chemical Engineering Journal*, 2025, 517, 164402. https://doi.org/10.1016/j.cej.2025.164402.

[119] Yishan Jin, Kai Jin, Wenjing Ji, Zhanfeng Zhang, Linsong Gan, Peng Han, Xinhai Yuan, Lijun Fu, Yuping Wu. Fabrication of a robust zinc powder anode *via* facile integration of copper nanopowder as a functional conductive medium. *Advanced Functional Materials*, 2025, 35, 2418503. https://doi.org/10.1002/adfm.202418503.

[120] Yanbo Wang, Xintao Ma, Xinru Yang, Rong Zhang, Hu Hong, Shixun Wang, Qing Li, Ze Chen, Zhaodong Huang, Haiming Lv, Chunyi Zhi. A multifunctional binder for current-collector-free Zn powder anodes. *Advanced Materials*, 2025, 37, 2419702. https://doi.org/10.1002/adma.202419702.

[121] Pengyang Lei, Jianli Cheng, Xilin Wang, Ruixin Zheng, Junxiang Zhang, Xiaorui Wang, Mengmeng Yang, Bin Wang. Zincophilic/hydrophobic balanced binder enables highly stable Zn powder anode toward flexible zinc-ion batteries. Nano energy, 2025, 141, 111090. https://doi.org/10.1016/j.nanoen.2025.111090.

[122] Xunwen Zheng, Ziyang Song, Da Zhang, Wenyan Du, Ling Miao, Yaokang Lv, Lihua Gan, Mingxian Liu. Biomimetic quasi-skin-capillary structure engineering of ionic-electronic conducting full-chain networks for stable zinc powder anodes. *Advanced Functional Materials*, 2025, 35, 2413990. https://doi.org/10.1002/adfm.202413990.

[123] Min Zhang, Peifeng Yu, Kairong Xiong, Yongyin Wang, Yingliang Liu, Yeru Liang. Construction of mixed ionic-electronic conducting scaffolds in Zn powder: A scalable route to sendrite-free and flexible Zn anodes. *Advanced Materials*, 2022, 34, 2200860. https://doi.org/10.1002/adma.202200860.

[124] Lin Qin, Kangwei Wen, Dengqiao Xiao, Binbin Liu, Zhenguo Wang, Jun Xu, Haihong Yin. Structurally engineered soft-elastic polymers as stress-adaptive and deposition-regulating layers for ultrastable and high-rate Zn-powder anodes. *Advanced Functional Materials*, 2026, 36, e22521. https://doi.org/10.1002/adfm.202522521.

[125] Qun Liu, Zhenlu Yu, Rui Zhou, Biao Zhang. A semi-liquid electrode toward stable Zn powder anode. *Advanced Functional Materials*, 2023, 33, 2210290. https://doi.org/10.1002/adfm.202210290.

[126] Jingxian Wang, Hong Zhang, Lizhuang Yang, Shiyu Zhang, Xiaopeng Han, Wenbin Hu. *In situ* implanting 3D carbon network reinforced zinc composite by powder metallurgy for highly reversible Zn-based batteriesy anodes. *Angewandte Chemie International Edition*, 2024, 63, e202318149. https://doi.org/10.1002/anie.202318149.

[127] Wencheng Du, Song Huang, Yufei Zhang, Minghui Ye, Chengchao Li. Enable commercial zinc powders for dendrite-free zinc anode with improved utilization rate by pristine graphene hybridization. *energy Storage Materials*, 2022, 45, 465-473. https://doi.org/10.1016/j.ensm.2021.12.007.

[128] Zhiqiang Xiao, Zhexuan Liu, Xinru Wu, Xiao Xiao, Yinna Liu, Jiachang Liu, Zhiyang Zheng, Wenxuan Yao, Jincheng Li, Guangmin Zhou. Artificial protrusion architectures enabling horizontal-diffusion nucleation for stable zinc-based batteries. *Journal of the American Chemical Society*, 2025, 147, 32216-32224. https://doi.org/10.1021/jacs.5c11951.

[129] Jiayu Yang, Xi Xu, Yong Gao, Yuxuan Wang, Qinghe Cao, Jie Pu, Fan Bu, Ting Meng, Cao Guan. Ultra-stable 3D-printed Zn powder-based anode coated with a conformal ion-conductive layer. *Advanced energy Materials*, 2023, 13, 2301997. https://doi.org/10.1002/aenm.202301997.

[130] Leiqing Cao, Fan Bu, Yuxuan Wang, Yong Gao, Wenbo Zhao, Jiayu Yang, Jipeng Chen, Xi Xu, Cao Guan. Multifunctional anchoring effect enables ultra-stable 3D-printed zinc powder-based anode. *Science China Materials*, 2025, 68, 897-905. https://doi.org/10.1007/s40843-024-3174-9.

[131] Guobing Sun, Ziyang Cui, Danyang Zhao, Zhixuan Jiao, Ling Li, Zezhan Zhang, Wenming Zhang, Qiancheng Zhu. Enhancing zinc-ion-transport kinetics in solid-state zinc batteries *via* an internal/surface dual acceleration strategy. *Nano Letters*, 2025, 25, 10742-10750. https://doi.org/10.1021/acs.nanolett.5c01076.

[132] Yue Hou, Qiong Liu, Zeru Wang, Xinru Yang, Dedi Li, Yiqiao Wang, Zhiquan Wei, Zhaodong Huang, Qing Li, Ke Wang, Chunyi Zhi. Leveraging piezoelectric and ferroelectric effects to control zinc deposition for high-performance solid-state zinc batteries. *Journal of the American Chemical Society*, 2026, 148, 16872-16881. https://doi.org/10.1021/jacs.5c23299.

[133] Chuancong Zhou, Zeyou Wang, Qing Nan, Huan Wen, Zhenming Xu, Jie Zhang, Zejun Zhao, Jing Li, Zhenyue Xing, Peng Rao, Zhenye Kang, Xiaodong Shi, Xinlong Tian. Simultaneous inhibition of vanadium dissolution and zinc dendrites by mineral-derived solid-state electrolyte for high-performance zinc metal batteries. *Angewandte Chemie*, 2024, 136, e202412006. https://doi.org/10.1002/ange.202412006.

[134] Sanlue Hu, Caiyun Chang, Yangpeng Lin, Jie Li, Dun Wang, Xuexia Lu, Kezhao Du, Hui-Ming Cheng, Cuiping Han. zinc-based metal halide electrolytes for all-solid-state zinc-metal batteries. *Nature Communications*, 2026, 17, 1691. https://doi.org/10.1038/s41467-026-68394-4.

[135] Jiaxin Li, Huanfeng Wang, Dehui Guan, Xiaoxue Wang, Chenglin Miao, Jijing Xu. Crystal transformation strategy in hydrogen-bonded organic framework solid-state electrolyte for stable zinc-ion batteries. *Advanced Materials*, 2025, 37,

2500721. https://doi.org/10.1002/adma.202500721.

[136] Xiaoyun Xu, Songmei Li, Rongrong Guo, Chuangchuang Zhang, Jia Zhou, Mei Yu, Juan Du, Jinyan Zhong, Shubin Yang, Bin Li. Achieving ultrafast monovalent $ZnCl^+$ ion transport in MOF-based Zn ion solid-state electrolyte through polyanion strategy. *Advanced Materials*, 2025, 37, e08925. https://doi.org/10.1002/adma.202508925.

[137] Hu Hong, Zhiquan Wei, Yiqiao Wang, Xinru Yang, Xun Guo, Qingshun Nian, Xinliang Li, Qing Li, Shixun Wang, Shimei Li, Dechao Zhang, Qi Xiong, Zhaodong Huang, Chunyi Zhi. A solid-state battery capable of 180 C superfast charging and 100% energy retention at -30 ℃. *Proceedings of the National Academy of Sciences*, 2025, 122, e2511121122. https://doi.org/10.1073/pnas.2511121122.

[138] Zhiming Zhao, Binbin Nian, Yongjiu Lei, Yizhou Wang, Lin Shi, Jian Yin, Omar F. Mohammed, Husam N. Alshareef. A novel plastic-crystal electrolyte with fast ion-transport channels for solid zinc-ion batteries. *Advanced energy Materials*, 2023, 13, 2300063. https://doi.org/10.1002/aenm.202300063.

[139] Wei Ling, Funian Mo, Xiongwei Wu, Xianxiang Zeng, Jian Xiong, Yan Huang. Solid-state eutectic electrolyte via solvation regulation for voltage-elevated and deep-reversible Zn batteries. *Nature Communications*, 2025, 16, 4868. https://doi.org/10.1038/s41467-025-60125-5.

[140] Ran Han, Yuefeng Meng, Xin Zhao, Yao Wang, Mingkun Tang, Yichen Ding, Baohua Li, Dong Zhou, Feiyu Kang. Polyphosphonitrile derivative-based gel electrolytes for all-climate zinc metal batteries operating from -70 ℃ to +80 ℃. *energy & Environmental Science*, 2025, 18, 5482-5491. https://doi.org/10.1039/d5ee01478f.

[141] Cheng Wang, Zhe Gong, Jodie A. Yuwono, Qiangqiang Meng, Yanqiu Lyu, Shilin Zhang, Shuixin Xia, Xin Zeng, Patrick J. Cullen, Jianfeng Mao, Zaiping Guo, Zengxia Pei. Ligand-channel-induced ion liberation in crowded zwitterionic hydrogel electrolyte for efficient zinc metal batteries. *Nature Communications*, 2025, 16, 11069. https://doi.org/10.1038/s41467-025-66041-y.

[142] Song Yang, Qing Wu, Yue Li, Fusheng Luo, Jinlong Zhang, Kui Chen, Yang You, Jun Huang, Haibo Xie, Yiwang Chen. A bio-inspired multifunctional hydrogel network with toughly interfacial chemistry for dendrite-free flexible zinc ion batteriesy. *Angewandte Chemie International Edition*, 2024, 63, e202409160. https://doi.org/10.1002/anie.202409160.

[143] Lingmei Wang, Huicai Wang, Junlun Cao, Jicheng Yan, Changwei Dai, Wuzhu Sun, Qingyang Du, Zhiqiang Huang, Dan Liu, Chao Li, Jingyu Sun. Restructuring hydrogen bond networks in polyacrylamide hydrogels via trehalose additives for wide-temperature-range Zn-ion batteries. *ACS Nano*, 2025, 19, 28397-28409. https://doi.org/10.1021/acsnano.5c06805.

[144] Qianqin Zhou, Fan Zhang, Ziqing Tan, Tony Wang, Dongchen Qi, Juan Bai, Ting Liao, Ziqi Sun. Gradient hydrogel electrolyte enables high ionic conductivity and robust mechanical properties for dendrite-free aqueous zinc-ion batteriesy. *Advanced Materials*, 2026, 38, e12775. https://doi.org/10.1002/adma.202512775.

[145] Guanjie Li, Zihan Zhao, Shilin Zhang, Liang Sun, Mingnan Li, Jodie A. Yuwono, Jianfeng Mao, Junnan Hao, Jitraporn Vongsvivut, Lidan Xing, Chunxia Zhao, Zaiping Guo. A biocompatible electrolyte enables highly reversible Zn anode for zinc ion battery. *Nature Communications*, 2023, 14, 6526. https://doi.org/10.1038/s41467-023-42333-z.

[146] Zihao Wang, Tianyu Zhu, Chengsheng Gui, Xushen Tan, Lu Sun, Chicheng Huang, Xiaozhe Zhang, Fuxiang Chu, Jingya Nan, Riqing Chen, Chunpeng Wang. Hierarchical-heterogeneous biogel electrolytes regulate zinc anode interfacial compatibility towards green and high-performance solid-state hybrid capacitors. *Advanced Materials*, 2026, 38, e22394. https://doi.org/10.1002/adma.202522394.

[147] Jing Huang, Sijun Wang, Le Yu, Erlantz Lizundia, Xuanyu Zeng, Lu Chen, Ziyang Lu, Luhe Qi, Yu Lin, Hongbing Deng, Chaoji Chen. Practical, sustainable, wide-temperature-adaptable zinc-metal batteries enabled by electrogelated recyclable biomacromolecular hydrogel electrolytes. *National Science Review*, 2025, 12, nwaf308. https://doi.org/10.1093/nsr/nwaf308.

[148] Feifei Wang, Jipeng Zhang, Haotian Lu, Hanbing Zhu, Zihui Chen, Lu Wang, Jinyang Yu, Conghui You, Wenhao Li, Jianwei Song, Zhe Weng, Chunpeng Yang, Quan-Hong Yang. Production of gas-releasing electrolyte-replenishing Ah-scale zinc metal pouch cells with aqueous gel electrolyte. *Nature Communications*, 2023, 14, 4211. https://doi.org/10.1038/s41467-023-39877-5.

[149] Dewu Lin, Jiapei Li, Mingzhan Wang, Muqiang Jian, Ruihong Pan, Yu Liu, Anquan Zhu, Tian Zhang, Kai Liu, Dongyu Feng, Kunlun Liu, Yin Zhou, Chengkai Yang, Guo Hong, Jin Zhang, Wenjun Zhang. Nanofluidic-engineered carbon nanotube ion highways in hydrogels enable high-power aqueous zinc-ion batteries. Science Advances, 2025, 11, eadx9812. https://doi.org/10.1126/sciadv.adx9812.

[150] Jiaying Peng, Weihao Song, Wei Zhang, Xinyu Li, Qing Ma, Bing Wu, Masatsugu Fujishige, Kenji Takeuchi, Morinobu Endo, Chendong Ji, Yilin Sun, Jin Niu, Feng Wang. Bone-inspired sustainable hydrogel electrolytes for Zn metal batteries. *Angewandte Chemie International Edition*, 2025, 64, e202506449. https://doi.org/10.1002/anie.202506449.

[151] Ziming Liu, Xuke Zhang, Heng Zhang, Qiankun Hun, Jiaxing Lu, Chao Yan. Construction of homogeneously porous composite hydrogel electrolyte for dendrite-free aqueous zinc-ion batteries: An Alkali-Etched Graphitized-Carbon Nitride Induced polymerization strategy. *Advanced Functional Materials*, 2026, 36, e75312. https://doi.org/10.1002/adfm.75312.

[152] Xueying Zheng, Qianqian Wang, Chuan Li, Tao Liu, Panqi Song, Haitao Li, Huilin Cui, Yuanhe Sun, Qi Xiong, Hu

Hong, Shixun Wang, Daming Zhu, Jun Fan, Chunyi Zhi. Amphiphile confined water electrolyte enables facilitated cation transport through nanometric water channels. *Journal of the American Chemical Society*, 2026, 148, 8772-8783. https://doi.org/10.1021/jacs.5c21201.

[153] Shihe Wang, Ganxiong Liu, Wang Wan, Xueyang Li, Ju Li, Chao Wang. Acetamide-caprolactam deep eutectic solvent-based electrolyte for stable Zn-metal batteries. *Advanced Materials*, 2024, 36, 2306546. https://doi.org/10.1002/adma.202306546.

[154] Jianhui Li, Siqi Qin, Mi Xu, Wei Wang, Jiabin Zou, Yongguang Zhang, Haozhen Dou, Zhongwei Chen. Multifunctional dual-metal-salt derived ternary eutectic electrolyte for highly reversible zinc ion batteriesy. *Advanced Functional Materials*, 2024, 34, 2402186. https://doi.org/10.1002/adma.202306546.

[155] Caixing Wang, Xuemei Wang, Huaizhu Wang, Chenxi Zheng, Shengwen Tan, Yanrong Wang, Guowang Diao, Zhong Jin. An organometallic chelated electrolyte based on 5-sulfosalicylic group coordination for elevated performance in aqueous zinc-ion batteries. *Advanced Functional Materials*, 2025, 35, 2424024. https://doi.org/10.1002/adfm.202424024.

[156] Heng Jiang, Longteng Tang, Yanke Fu, Shitong Wang, Sean K. Sandstrom, Alexis M. Scida, Guoxing Li, David Hoang, Jessica J. Hong, Nanchieh Chiu, Kyriakos C. Stylianou, William F. Stickle, Donghai Wang, Ju Li, P. Alex Greaney, Chong Fang, Xiulei Ji. Chloride electrolyte enabled practical zinc metal battery with a near-unity Coulombic efficiency. *Nature Sustainability*, 2023, 6, 806-815. https://doi.org/10.1038/s41893-023-01092-x.

[157] Yu Liu, Jiaxin Meng, Mohan Yue, Changmei Jiao, Zhiyuan Zhao, Yuzhen Sun, Yingna Chang, Huayu Wu, Xiaoli Yan, Kefan Song, Jindi Wang, Weizhai Bao, Guozhen Zhang, Rong Xing, Jingfa Li, Feng Yu, Faxing Wang, Yuping Wu. Thermodynamically stable colloid dispersion electrolytes with the Tyndall effect for practical zinc-ion pouch cells. *energy & Environmental Science*, 2026, 19, 589-604. https://doi.org/10.1039/d5ee05434f.

[158] Pinji Wang, Tianchen Li, Yanfen Liu, Congjian Lin, Yangfeng Cui, Haobin Song, Bingan Lu, Shuquan Liang, Huiying Yang, Jiang Zhou. Targeted docking of localized hydrogen bond for efficient and reversible zinc-ion batteries. *Angewandte Chemie International Edition*, 2025, 64, e202422547. https://doi.org/10.1002/anie.202422547.

[159] Kai Yang, Yun Liu, Chengjie Yuan, Yingxue Wang, Yuanyuan Hu, Junwei Zhao, Licheng Miao. Trace diluent-like polyoxometalate modulated localized high-concentration electrolyte enables highly reversible zinc metal chemistry. *Advanced Functional Materials*, 2026, 36, e15837. https://doi.org/10.1002/adfm.202515837.

[160] Shengyang Huang, Zuyang Hu, Xinwang Mo, Yeonju Park, Junsu Kim, Gun Jang, Donghyun Min, Hao Fu, Peixun Xiong, Zhipeng Wen, Young Mee Jung, Jaeyun Kim, Hyunjoo Lee, Chihyun Hwang, Youngkwon Kim, Chengchao Li, Qingyun Dou, Ho Seok Park. Self-assembled ordered nanostructure of zwitterionic co-solutes induces localized high-concentration electrolytes for ultrastable and efficient zinc metal anodes. *Nano-Micro Letters*, 2026, 18, 194. https://doi.org/10.1007/s40820-025-02040-4.

[161] Sinian Yang, Shunshun Zhao, Haojie Xu, Xinwei Wang, Xuanrui Huang, Qi Yang, Yong Chen, Guoxiu Wang, Shimou Chen. Gradient chaotropic regulation of Zn2+ solvation chemistry for low-temperature zinc metal batteries. *Nature Communications*, 2026, 17, 736. https://doi.org/10.1038/s41467-025-67426-9.

[162] Xin Zhao, Jiaping Fu, Ming Chen, Yao Wang, Cong Huang, Kun Qian, Guang Feng, Baohua Li, Dong Zhou, Feiyu Kang. A self-phase separated electrolyte toward durable and rollover-stable zinc metal batteries. *Journal of the American Chemical Society*, 2025, 147, 2714-2725. https://doi.org/10.1021/jacs.4c15132.

[163] Changxin Zhao, Zheng Li, Bin Chen, Fu Chen, Chunsheng Wang. Self-adaptive electrolytes for fast-charging batteries. *Nature energy*, 2025, 10, 904-913. https://doi.org/10.1038/s41560-025-01801-0.

[164] Huimin Wang, Mingzi Sun, Yongqiang Yang, Junhua Zhou, Lingtao Fang, Qiyao Huang, Bolong Huang, Zijian Zheng. Designing multi-tentacle electrolytes to enable fast and deep cycling of aqueous Zn batteries at low temperatures. *energy & Environmental Science*, 2025, 18, 5492-5502. https://doi.org/10.1039/d5ee01316j.

[165] Jianxin Wang, Han Zhang, Mingyu Yin, Huaizheng Ren, Jiaxuan Liu, Nan Zhang, Lei Wang, Chengfan Jiang, Tiancheng Chen, Bowen Cong, Dianlong Wang, Chao Wu, Huakun Liu, Shixue Dou, Dongliang Chao, Bo Wang. Biomimetic anchor-capture effect of multidentate electrolyte additive for ultrastable aqueous zinc ion batteries. *Angewandte Chemie International Edition*, 2026, 65, e26100. https://doi.org/10.1002/anie.202526100.

[166] Hebang Li, Lulu Deng, Yanhui Zhang, Kui Chen, Yuanlong Guo, Qinqin Xu, Mingwei Xu, Haibo Xie, Lei Wang. Synergistic biomass electrolyte *via* mechanochemistry enables ultralong-life dendrite-free zinc anodes. *energy Storage Materials*, 2025, 82, 104639. https://doi.org/10.1016/j.ensm.2025.104639.

[167] Xinghui Liu, Jiahui Lyu, Huizhen Jin, Jia Sun, Songtao Zhu, Miao Liu, Han Jiang. Design strategies for acidic oxygen evolution reaction catalysts. *Matter*, 2025, 8, 102358. https://doi.org/10.1016/j.matt.2025.102358.

[168] Yanbo Wang, Bochun Liang, Dedi Li, Yiqiao Wang, Chuan Li, Huilin Cui, Rong Zhang, Shuo Yang, Ze Chen, Qing Li, Funian Mo, Jun Fan, Chunyi Zhi. Hydrogel electrolyte design for long-lifespan aqueous zinc batteries to realize a 99% Coulombic efficiency at 90 ℃. *Joule*, 2025, 9, 101944. https://doi.org/10.1016/j.joule.2025.101944.

[169] Jingxuan Ren, Jie Zhang, Yufeng Chen, Renming Liu,

Chuangwei Liu, Xinli Guo, Dan Luo, Dongdong Wang, Zhongwei Chen. Multiphase aqueous soggy sand electrolyte for zinc metal batteries applications at elevated temperatures. *Nature Communications*, 2025, 17, 309. https://doi.org/10.1038/s41467-025-67020-z.

[170] Lei Zhang, Yu Han, Yaheng Geng, Hui Zhang, Hongguang Liu, Yan He, Zichao Yan, Zhiqiang Zhu. Aqueous zinc-ion batteries with boosted stability and kinetics under a wide temperature range. *Angewandte Chemie International Edition*, 2025, 64, e202500434. https://doi.org/10.1002/anie.202500434.

[171] Guanjie Li, Qinqin Cai, Shilin Zhang, Jodie A. Yuwono, Lei Mao, Huanyu Jin, Zaiping Guo. Decoupled dual-salt electrolyte for practical aqueous zinc batteries. *Nature Sustainability*, 2025, 8, 1349-1359. https://doi.org/10.1038/s41893-025-01646-1.